



University of Dhaka

Spectral Relaxation numerical simulation of boundary layer flow with nanoparticles on a moving surface influenced by induced magnetic field

A dissertation submitted for the degree of
Doctor of Philosophy

By

Shahina Akter

Registration No: 72/2015-16 & 26/2020-21(Re-Reg)

Department of Applied Mathematics

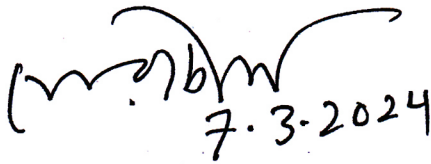
University of Dhaka

Dhaka, Bangladesh

February, 2024

Certificate

This is to certify that the thesis entitled “Spectral Relaxation numerical simulation of boundary layer flow with nanoparticles on a moving surface influenced by induced magnetic field” submitted by **Shahina Akter** as partial fulfillment of the criteria for the degree of **Doctor of Philosophy** in Applied Mathematics. The entire thesis or a portion of it has not been submitted for the award of any other Degree, Diploma, Associateship, or Fellowship of any other University or Institution.



7.3.2024

Professor Dr. Mohammad Ferdows

Supervisor

Department of Applied Mathematics

University of Dhaka

Dhaka-1000, Bangladesh

Abstract

The concept of boundary-layer flow is of utmost importance in the science of fluid dynamics, playing a significant role in a wide variety of engineering applications and natural phenomena. The proliferation of research on heat and mass transfer in boundary layers over perpetually moving surfaces can be attributed to the diverse range of manufacturing processes in which they are used, including paper production, metal extrusion, material-handling conveyors, and glass fibre production. Additionally, the expansion of nanotechnology has spurred researchers to explore the flow behaviour at the boundary layer in nanofluids. A nanofluid is a fluid that contains nanoparticles, which results in a significant enhancement of its heat transfer properties due to the increased thermal conductivity. The ability to boost heat and mass transfer with a low concentration of nano-sized particles, and to regulate the transport processes, have led to a large variety of applications for nanofluids. Furthermore, the interaction of a magnetic field with a nanofluid has numerous potential uses that rely on the potential variation in the fluid perpendicular to both its motion and the magnetic field.

This thesis presents numerical studies of boundary-layer flow and heat transfer from a moving flat plate subject to different boundary conditions under the influence of an applied induced magnetic field. The focus is on flows of two-dimensional, stable, viscous, incompressible, laminar, and electrically conducting water-based nanofluids incorporated with different metallic and magnetic nanoparticles.

At the beginning of this thesis, a theoretical model is studied for steady magnetohydrodynamic (MHD) viscous flow resulting from the motion of a semi-infinite flat plate in an electrically conducting nanofluid. Thermal radiation magnetic induction effects and thermal convective boundary conditions are included. Buongiorno's two-component nanoscale model is deployed, which features Brownian motion and thermophoresis effects. The second study examines the continuous laminar boundary-layer flow of *Ag*-water and *Cu*-water nanofluids with convective heat transport from an inclined stationary or moving flat plate, with a convective surface boundary condition, when there is an induced magnetic field. Then, we perform a computational analysis of

the combined impacts of temperature- and space-dependent internal heat generation/absorption across a moving flat surface in the presence of an induced magnetic field with a momentum slip condition on the boundary-layer flow of a nanofluid. Later, we investigate the effects of viscous dissipation on a convective aligned MHD flow of a nanofluid over a semi-infinite moving flat surface, where the vectors of the magnetic field and the flow velocity are parallel far from the plate. Lastly, the influence of an induced magnetic field on the MHD heat transfer flow of water-based ferrofluids, under the influence of slip, over a moving plate subject to uniform heat flux, is analysed. A transverse magnetic field is applied to the plate.

The aforementioned mathematical problems are solved by applying appropriate similarity transformations to convert the governing boundary-layer equations and related boundary conditions into a system of nonlinear coupled ordinary differential equations. The fluid is assumed to be a water-based nanofluid containing metallic and magnetic nanoparticles with Prandtl number $Pr = 6.2$, without a slip condition. The transformed system of differential equations is solved numerically, employing the spectral relaxation method (SRM) via the MATLAB R2018a software. The SRM is a simple iteration scheme for solving a nonlinear system of equations that does not require any evaluation of derivatives, perturbation, or linearization.

Throughout this thesis, the profiles of velocity, induced magnetic field, temperature, and nanoparticle concentration are derived numerically and displayed for a range of physical parameter values. The significance of multiple embedded physical parameters, including the sheet velocity parameter, magnetic field parameter, Prandtl number, magnetic Prandtl number, thermal radiation parameter, Lewis number, Brownian motion parameter, thermophoresis parameter, Grashof number, Biot number, angle of inclination, nanoparticle volume function, Eckert number, and slip parameter, on the fluid flow is examined, and the findings are presented graphically. The numerical values of the skin friction coefficient, heat transfer rate, mass transfer rate, and other missing slope characteristics are tabulated. The impacts of different metallic and magnetic nanoparticles on the boundary-layer flow, friction drag, and heat flow rate are also investigated. To determine the validity of the computational results, they are compared with those of earlier studies. Thus, this study yields a conclusion that supports the accuracy and reliability of the SRM outcomes.

The significance of the electrical conductivity of nanofluids is that the flow and heat transfer may be controlled by an external magnetic field, which could lead to important applications in areas

such as electronic packing, mechanical engineering, thermal engineering, aerospace, and bioengineering. Increasing the magnetic body force parameter strongly reduces the flow velocity and suppresses magnetic induction, but increases the temperature due to the extra work expended as heat in dragging the magnetic nanofluid. Temperatures also increase with the nanoscale thermophoresis parameter and radiative parameter, whereas they are reduced by a higher wall velocity, Brownian motion parameter, or Prandtl number. Both the hydrodynamic and magnetic boundary-layer thicknesses are reduced by greater reciprocal values of the magnetic Prandtl number. The nanoparticle (concentration) boundary-layer thickness increases with the thermophoresis parameter and Prandtl number, whereas it decreases with increasing wall velocity, nanoscale Brownian motion parameter, radiative parameter, and Lewis number. The simulations are relevant to electroconductive nanomaterial processing. The nanofluid with *Ag* nanoparticles is found to have remarkably high thermal conductivity, whereas the lowest cooling rate is observed in the *TiO₂*–water nanofluid. Moreover, higher flow resistance and a faster rate of heat transfer are detected in magnetite nanofluids. The magnetic field's principal effects are to lower the dimensionless velocity and raise the dimensionless surface temperature compared with the hydrodynamic situation, which in turn increases the ferrofluid skin friction and heat transfer rate.

In recent times, there has been a growing trend of companies recognizing the potential of nanofluid technology and directing their attention to its specific industrial applications. The utilization of boundary-layer flow over a flat surface coupled with nanofluid has found extensive application for addressing thermal management issues. The interaction of magnetic fields and fluid dynamics is crucial in various applications such as liquid metal cooling, magnetic drug targeting, and MHD power generation. In essence, the investigation of boundary-layer flow involving nanoparticles on an evolving surface subjected to an induced magnetic field is of great importance due to its capacity to enhance heat transfer, diminish friction, and propel advancements in fields such as energy production and medicine.

List of Publications

Journal Papers

1. Akter, S., Ferdows, M., Shamshuddin, M. D., Siri, Z. (2022). Similarity solution for induced magnetic field boundary layer flow of metallic nanofluids via convectively inclined stationary/moving flat plate: Spectral Relaxation computation. *ZAMM- Journal of Applied Mathematics and Mechanics*, 102(1), 1-24. [Impact Factor 1.759].
2. Akter, S., Ferdows, M., Tasveer Bég , A., Anwar Bég, O., Kadir, A., Sun, S. (2021). Spectral relaxation computation of electroconductive nanofluid convection flows from a moving surface with radiative flux and magnetic induction. *Journal of Computational Design and Engineering*, 8(4), 1158-1171. [Impact Factor 6.167]

Conference Presentations

1. Akter, S., & Ferdows, M., Spectral Relaxation computation of Slip Effects and Heat Transfer of MHD Ferrofluid Flow over a moving flat plate. *The 1st International Conference on Frontier in Sciences (ICFS-2022)*, BUET, Dhaka, Bangladesh, (2022, November 11-12).
2. Akter, S., & Ferdows, M., Spectral Relaxation computation of heat transfer in aligned-field MHD Flow of nanofluid over a moving flat plate. *Proceedings of UK Fluids Conference*, University of Southampton, (2021, September 08-10).
3. Akter, S., & Ferdows, M., Impulsion of space and temperature dependent internal heat generation/absorption effects on Nanofluid over a moving plate in the presence of induced magnetic field. *Proceedings of ICHMT International Symposium on Advances in Computational Heat Transfer*, Rio de Janeiro, Brazil, (2021, August 15-21).

Table of Contents

Abstract	i
List of Publications	iv
Table of Contents	v
List of Figures	viii
List of Tables	xiv
Symbols	xvi
Chapter 1	Introduction
1.1	Overview of the Literature 1
1.2	Identification of Problems 8
1.3	Goals of the Thesis 9
1.4	Research Significance 10
1.5	Structure of the Thesis 11
Chapter 2	Spectral Relaxation Method
	Illustration of the solution methodology 14
Chapter 3	Spectral Relaxation Simulation of Electroconductive Radiative Nanofluid Flow with Magnetic Induction over a Moving Surface
3.1	Governing Equations for Magnetic Induction Nanofluid Flow 20
3.2	Computational Solution with the Spectral Relaxation Method 25
3.3	Validation of the Spectral Relaxation Method 28
3.4	Results and Discussion 29
3.5	Summary 41

Chapter 4	Spectral Relaxation Method for Convective Metallic Nanofluids Flow with an Induced Magnetic Field past an Inclined Stationary or Moving Flat Plate	
4.1	Mathematical Modelling	42
4.2	Thermophysical Properties of Nanofluids	44
4.3	Numerical Results and Discussion	49
4.4	Summary	68
Chapter 5	MHD Boundary-Layer Slip Flow with an Induced Magnetic Field Simulated by Space- and Temperature-Dependent Internal Heat Generation/Absorption over a Moving Plate	
5.1	Problem Formulation	69
5.2	Spectral Relaxation Method Simulation	74
5.3	Findings and Discussion	76
5.4	Summary	87
Chapter 6	Numerical Simulation for the Influence of Aligned-Field MHD Nanofluids on Heat Transfer over a Moving Flat Plate	
6.1	Mathematical Model with Flow Configuration	88
6.2	Solution Procedure with the Spectral Relaxation Method Scheme	92
6.3	Computational Results and Physical Interpretation	94
6.4	Summary	105
Chapter 7	Slip Effects and Heat Transfer of MHD Ferrofluid Flow across a Moving Flat Plate by Spectral Relaxation Simulation	
7.1	Mathematical Formulation	106
7.2	Numerical Solution with the Spectral Relaxation Method	110
7.3	Observations and Discussion	112
7.4	Summary	124

Chapter 8	Conclusions	
8.1	Summary of the Outcomes	125
8.2	Future Prospects	128
	References	129

List of Figures

Fig. 3.1	Magnetic induction nanofluid radiative convection physical model	21
Fig. 3.2 (a)	The influence of λ on velocity profile	33
Fig. 3.2 (b)	The influence of λ on induced magnetic field profile	33
Fig. 3.2 (c)	The influence of λ on temperature profile	33
Fig. 3.2 (d)	The influence of λ on concentration profile	33
Fig. 3.3 (a)	The influence of magnetic force parameter, β on velocity profile	34
Fig. 3.3 (b)	The influence of magnetic force parameter, β on induced magnetic field	34
Fig. 3.4 (a)	The influence of Nb on temperature profile	35
Fig. 3.4 (b)	The influence of Nb on concentration profile	35
Fig. 3.5 (a)	The influence of Nt on temperature profile	36
Fig. 3.5 (b)	The influence of Nt on concentration profile	36
Fig. 3.6 (a)	The influence of Pr on temperature profile	36
Fig. 3.6 (b)	The influence of Pr on concentration profile	36
Fig. 3.7 (a)	The influence of Prm on velocity profile	37
Fig. 3.7 (b)	The influence of Prm on induced magnetic field profile	37
Fig. 3.8 (a)	The influence of Rd on temperature profile	38
Fig. 3.8 (b)	The influence of Rd on concentration profile	38
Fig. 3.9	The influence of Le on concentration profile	38
Fig. 3.10	Influence of β and λ on the skin friction co-efficient C_f	40
Fig. 3.11	Influence of Pr and λ on reduced Nusselt Number Nu	40

Fig. 3.12	Influence of Le and λ on reduced Sherwood number Sh	41
Fig. 4.1	Physical model of the problem	43
Fig. 4.2 (a)	Effect of nanoparticle value fraction ϕ on velocity for $\lambda = 1$	53
Fig. 4.2 (b)	Effect of nanoparticle value fraction ϕ on velocity for $\lambda = 0$	53
Fig. 4.3 (a)	Effect of nanoparticle value fraction ϕ on induced magnetic field for $\lambda = 1$	54
Fig. 4.3 (b)	Effect of nanoparticle value fraction ϕ on induced magnetic field for $\lambda = 0$	54
Fig. 4.4 (a)	Effect of nanoparticle value fraction ϕ on temperature for $\lambda = 1$	55
Fig. 4.4 (b)	Effect of nanoparticle value fraction ϕ on temperature for $\lambda = 0$	55
Fig. 4.5 (a)	Effect of Grashof number Gr for $\lambda = 1$ on velocity	56
Fig. 4.5 (b)	Effect of Grashof number Gr for $\lambda = 1$ on induced magnetic field	56
Fig. 4.5 (c)	Effect of Grashof number Gr for $\lambda = 1$ on temperature	56
Fig. 4.6	Effect of magnetic Prandtl number Prm on induced magnetic field for $\lambda = 1$	57
Fig. 4.7 (a)	Effect of inclined angle α for $\lambda = 1$ on velocity	58
Fig. 4.7 (b)	Effect of inclined angle α for $\lambda = 1$ on induced magnetic field	58
Fig. 4.7 (c)	Effect of inclined angle α for $\lambda = 1$ on temperature	58
Fig. 4.8 (a)	Effect of Biot number Bi on velocity for $\lambda = 1$	59
Fig. 4.8 (b)	Effect of Biot number Bi on velocity for $\lambda = 0$	59
Fig. 4.9 (a)	Effect of Biot number Bi on induced magnetic field for $\lambda = 1$	60
Fig. 4.9 (b)	Effect of Biot number Bi on induced magnetic field for $\lambda = 0$	60
Fig. 4.10 (a)	Effect of Biot number Bi on temperature for $\lambda = 1$	61
Fig. 4.10 (b)	Effect of Biot number Bi on temperature for $\lambda = 0$	61
Fig. 4.11 (a)	Effect of magnetic interaction parameter M for $\lambda = 1$ on velocity	62

Fig. 4.11 (b)	Effect of magnetic interaction parameter M for $\lambda = 1$ on induced magnetic field	62
Fig. 4.11 (c)	Effect of magnetic interaction parameter M for $\lambda = 1$ on temperature	62
Fig. 4.12 (a)	Effect of nanoparticle value fraction ϕ for both $\lambda = 0$ and $\lambda = 1$ on velocity	64
Fig. 4.12 (b)	Effect of nanoparticle value fraction ϕ for $\lambda = 0$ and $\lambda = 1$ on induced magnetic field	64
Fig. 4.12 (c)	Effect of nanoparticle value fraction ϕ for $\lambda = 0$ and $\lambda = 1$ on temperature	64
Fig. 4.13 (a)	Effect of magnetic interaction parameter M for $\lambda = 0$ and $\lambda = 1$ on velocity	65
Fig. 4.13 (b)	Effect of magnetic interaction parameter M for $\lambda = 0$ and $\lambda = 1$ on induced magnetic field	65
Fig. 4.13 (c)	Effect of magnetic interaction parameter M for $\lambda = 0$ and $\lambda = 1$ on temperature	65
Fig. 4.14	Influence of ϕ and M on skin friction coefficient C_f for $\lambda = 0$ when $Gr = 0.5$, $Pr = 6.2$, $\alpha = 45^\circ$, $Bi = 1$, and $Prm = 0.1$	66
Fig. 4.15	Influence of ϕ and M on reduced Nusselt number Nu for $\lambda = 0$ when $Gr = 0.5$, $Pr = 6.2$, $\alpha = 45^\circ$, $Bi = 1$, and $Prm = 0.1$	66
Fig. 4.16	Influence of ϕ and M on skin friction coefficient C_f for $\lambda = 1$ when $Gr = 0.5$, $Pr = 6.2$, $\alpha = 45^\circ$, $Bi = 1$, and $Prm = 0.1$	67
Fig. 4.17	Influence of ϕ and M on reduced Nusselt number Nu for $\lambda = 1$ when $Gr = 0.5$, $Pr = 6.2$, $\alpha = 45^\circ$, $Bi = 1$, $Prm = 0.1$	67
Fig. 5.1	Coordinates and the physical model	70
Fig. 5.2 (a)	Impact of slip parameter α for Cu -water on velocity	77
Fig. 5.2 (b)	Impact of slip parameter α for Cu -water on induced magnetic field	77
Fig. 5.2 (c)	Impact of slip parameter α for Cu -water on temperature	77
Fig. 5.3 (a)	Impact of magnetic Prandtl number Prm for Cu -water on velocity	78
Fig. 5.3 (b)	Impact of magnetic Prandtl number Prm for Cu -water induced magnetic field	78

Fig. 5.4	Induced magnetic field for Cu -water nanofluid for different values of χ	80
Fig. 5.5	Temperature distribution for Cu -water nanofluid for different values of A^*	80
Fig. 5.6	Temperature distribution for Cu -water nanofluid for different values of B^*	81
Fig. 5.7	Effect of ϕ on temperature profile with A^* and B^* for Cu -water nanofluid	81
Fig. 5.8	Effect of M on temperature profile with A^* and B^* for Cu -water nanofluid	82
Fig. 5.9	Velocity distributions for different nanofluids	83
Fig. 5.10	Induced magnetic field distributions for different nanofluids	84
Fig. 5.11	Temperature distributions for different nanofluids	84
Fig. 5.12	Effects of ϕ and M on skin friction coefficient C_f when $\lambda < 1$	85
Fig. 5.13	Effects of ϕ and M on skin friction coefficient C_f when $\lambda > 1$	85
Fig. 5.14	Effects of ϕ and M on reduced Nusselt number Nu when $\lambda < 1$	86
Fig. 5.15	Effects of ϕ and M on reduced Nusselt number Nu when $\lambda > 1$	86
Fig. 6.1	Geometry of flat moving plate	89
Fig. 6.2 (a)	Impact of velocity ratio parameter ϵ on velocity	96
Fig. 6.2 (b)	Impact of velocity ratio parameter ϵ on induced magnetic field	96
Fig. 6.2 (c)	Impact of velocity ratio parameter ϵ on temperature	96
Fig. 6.3 (a)	Impact of magnetic parameter M on velocity	97
Fig. 6.3 (b)	Impact of magnetic parameter M on induced magnetic field	97
Fig. 6.3 (c)	Impact of magnetic parameter M on temperature	97
Fig. 6.4 (a)	Impact of volume fraction parameter ϕ on velocity	99
Fig. 6.4 (b)	Impact of volume fraction parameter ϕ on induced magnetic field	99
Fig. 6.4 (c)	Impact of volume fraction parameter ϕ on temperature	99

Fig. 6.5 (a)	Impact of magnetic Prandtl number Prm on velocity	100
Fig. 6.5 (b)	Impact of magnetic Prandtl number Prm on induced magnetic field	100
Fig. 6.6	Temperature distributions for different values of Eckert number Ec	100
Fig. 6.7 (a)	Velocity distributions for different nanofluids	101
Fig. 6.7 (b)	Induced magnetic field distributions for different nanofluids	101
Fig. 6.7 (c)	Temperature distributions for different nanofluids	101
Fig. 6.8	Impact of M on skin friction for different nanofluids	102
Fig. 6.9	Impact of M on Nusselt number for different nanofluids	102
Fig. 6.10	Impact of ϕ on skin friction for different nanofluids	103
Fig. 6.11	Impact of ϕ on Nusselt number for different nanofluids	103
Fig. 6.12	Impact of Ec on Nusselt number for different nanofluids	104
Fig. 7.1	Diagram illustrating the ferrofluid boundary layer flow over a flat plate	107
Fig. 7.2 (a)	Impact of slip parameter α on velocity	114
Fig. 7.2 (b)	Impact of slip parameter α on induced magnetic field	114
Fig. 7.2 (c)	Impact of slip parameter α on temperature	114
Fig. 7.3 (a)	Impact of magnetic parameter M on velocity	116
Fig. 7.3 (b)	Impact of magnetic parameter M on induced magnetic field	116
Fig. 7.3 (c)	Impact of magnetic parameter M on temperature	116
Fig. 7.4	Induced magnetic field profiles for various magnetic Prandtl number Prm	117
Fig. 7.5	Temperature distributions for different values of Eckert number Ec	117
Fig. 7.6 (a)	Impact of slip parameter α on velocity for the ferroparticles	119
Fig. 7.6 (b)	Impact of slip parameter α on induced magnetic field for the ferroparticles	119
Fig. 7.6 (c)	Impact of slip parameter α on temperature for the ferroparticles	119

Fig. 7.7 (a)	Impact of magnetic parameter M on velocity for the ferroparticles	120
Fig. 7.7 (b)	Impact of magnetic parameter M on induced magnetic field for the ferroparticles	120
Fig. 7.7 (c)	Impact of magnetic parameter M on temperature for the ferroparticles	120
Fig. 7.8 (a)	Impact of ϕ on velocity for the ferroparticles	121
Fig. 7.8 (b)	Impact of ϕ on induced magnetic field for the ferroparticles	121
Fig. 7.9	Variation of the skin friction coefficient with α for different ferrofluids	122
Fig. 7.10	Variation of the Nusselt number with α for different ferrofluids	122
Fig. 7.11	Variation of the skin friction coefficient with ϕ and M for different ferrofluids	123
Fig. 7.12	Variation of the Nusselt number with ϕ and M for different ferrofluids	123

List of Tables

Table 3.1	Comparison of SRM solutions for $-f''(0)$ when $Pr = 0.7$, $Prm = 0.5$, $\beta = 0.1$, $Nt = 0.1$, $Nb = 0.3$, $Rd = 0.5$, and $Le = 5$	29
Table 3.2	Skin friction co-efficient C_f , the reduced Nusselt number Nu , and the reduced Sherwood number Sh with $Prm = 0.71$, $\beta = 0.1$	30
Table 3.3	Reduced Nusselt number Nu with $Prm = 0.71$, $\beta = 0.1$, $Le = 1$, $Nb = Nt = 0.3$, $Rd = 1$	31
Table 3.4	Reduced Sherwood number Sh with $Pr = 0.71$, $Prm = 0.71$, $\beta = 0.1$, $Nb = Nt = 0.3$, $Rd = 1$	31
Table 3.5	Skin friction co-efficient C_f with $Pr = 0.7$, $Prm = 0.5$, $\lambda = 0.1$, $Nt = 0.1$, $Nb = 0.3$, $Rd = 0.5$, and $Le = 5$	32
Table 4.1	Thermophysical properties of the base fluid and nanoparticles	45
Table 4.2	Mathematical relations of thermophysical properties of nanofluid	45
Table 4.3	Nanoparticle volume fraction parameters	46
Table 4.4	Comparison of the SRM $-\theta'(0)$ results with Aziz (2009) for different values of Biot number when $\alpha = \pi/2$, $\phi = 0$, $Gr = 0$, $M = 0$, $Prm = 0$, and $\lambda = 0$	50
Table 4.5	Comparison of the SRM $-\theta'(0)$ results with Ramesh (2016) for different values of Bi when $\alpha = \pi/6$, $Gr = 0.5$, $\phi = 0$, $M = 0$, and $Prm = 0$, for $\lambda = 0$ and $\lambda = 1$	51

Table 4.6	Numerical data for $f''(0)$ and $-\theta'(0)$ for <i>Cu</i> -water and <i>Ag</i> -water nanofluids with $\phi = 0.2$, $Gr = 0.5$, $Pr = 6.2$, $Bi = 1$, and $\lambda = 1$	52
Table 5.1	Thermophysical properties of the base fluid and nanoparticles	72
Table 6.1	Thermophysical characteristic of fluid and nanoparticles	92
Table 6.2	Comparison of $-\theta'(0)$ values for various values of Ec when $\epsilon = 0.1$, $Pr = 6.2$, $Prm = 0.1$, $M = 0.5$, and $\phi = 0$	94
Table. 7.1	Thermophysical properties of the base fluid and magnetic nanoparticles	113
Table. 7.2	Comparison of $f''(0)$ values for various values of α and β when $Pr = 6.2$, $Prm = 1$, and $\phi = M = \lambda = Ec = 0$	113

Symbols

α	Thermal diffusivity of the nanofluid
α_1	Magnetic diffusivity of nanofluid
B	Magnetic body force number
β	Thermal expansion coefficient
Bi	Biot number
c	Constant
C_f	Skin friction coefficient
C_w	Nanoparticle concentration at the moving wall
C_∞	Nanoparticle concentration in the free stream
D	Differentiation matrix in spectral algorithm
D_T	Buongiorno nanoscale thermophoresis diffusion coefficient
D_B	Buongiorno nanoscale Brownian diffusion coefficient
f	Dimensionless stream function
f	Vector function at the collocation points
f'	Dimensionless velocity
g	Dimensionless magnetic induction stream function
g'	Dimensionless induced magnetic field stream function gradient
$F_{r+1}(\eta)$	Current iteration level of dimensionless velocity
Gr	Grashof number
$G_{r+1}(\eta)$	Current iteration level of dimensionless magnetic stream function

h_f	Heat transfer coefficient
H_1, H_x	Dimensional magnetic stream function components along the x-axis
H_2, H_y	Dimensional magnetic stream function components along the y-axis
K	Thermal conductivity of magnetic nanofluid
K_S	Radiative mean absorption coefficient
λ	Wall velocity parameter
Le	Lewis number
M	Magnetic body force number
N	Collocation points deployed in the spectral method
Nu_x	Local Nusselt number
O	Size of the matrix in the spectral algorithm
Pr	Prandtl number
Prm	Magnetic Prandtl number
q_m	Nanoparticle mass transfer rate at the wall
q_r	Fourier heat flux
q_w	Heat transfer rate at the wall
Rd	Radiation parameter (Rosseland number)
Re_x	Local Reynolds number
Sh_x	Local Sherwood number
T	Magnetic nanofluid temperature
T_f	Hot fluid temperature
T_w	Temperature at the moving wall

T_∞	Temperature in the free stream
U	Velocity of the free stream (at the boundary layer edge)
U_w	Velocity of moving wall (sheet)
η	Dimensionless similarity variable (transverse coordinate)
η_∞	Infinity value (to edge of boundary layer domain)
ρ	Nanofluid density
(ρC_p)	Heat capacity
$\rho\beta$	Thermal diffusivity
σ	Electrical conductivity
σ^*	Stefan-Boltzmann constant
θ	Dimensionless temperature function
ϕ	Dimensionless nanoparticle concentration function
μ	Magnetic nanofluid dynamic viscosity
ν	Magnetic nanofluid kinematic viscosity
μ_0	Magnetic nanofluid permeability
τ	Heat capacity of the magnetic nanoparticles
τ_j	Gauss-Lobatto collocation points
τ_w	Shear stress on the wall
ψ	Dimensional stream function
Φ	Dimensional magnetic stream function
u, v	Dimensional velocity components along the x-axis and y-axis, respectively
x, y	Cartesian coordinates (x - axis is aligned along the horizontal surface, and y - axis is normal to it)

Subscripts

f	base fluid
s	nanoparticle
nf	nanofluid

Chapter 1

Introduction

This introductory chapter provides a comprehensive overview of the steady laminar two-dimensional convection boundary-layer flow of nanofluids made up of water and various types of nanoparticles. The research concentrates on analysing the dynamic interaction between a nanofluid and a moving flat plane. The study considers the remarkable influence of a magnetic field on the convective behaviour exhibited by the nanofluid. Incorporating different types of nanoparticles adds an extra layer of complexity, requiring a thorough analysis of their effects on the boundary-layer flow. This exploration enhances our understanding of the interplay between fluid dynamics, nanotechnology, and external magnetic influences, advancing our theoretical knowledge and providing valuable insights for practical applications.

To lay a strong groundwork for the ensuing discussions, a thorough literature review is presented, focusing on key themes that will be explored further in the upcoming chapters. The process of problem identification is then discussed, followed by the research goals and phenomena to be investigated. This sets the stage for the subsequent chapters, ensuring a comprehensive exploration of boundary-layer flow induced by magnetic fields in nanofluids. The study promises to provide valuable insights at the intersection of fluid dynamics and nanotechnology.

1.1 Overview of the Literature

The study of fluid dynamics has received a great deal of attention due to its widespread applications in engineering, science, and technology. Boundary-layer flow is among the most widely researched topics. Blasius (1908) was the first to investigate and present a theoretical result for boundary-layer flow over a flat plate in a uniform stream. Using both exact and approximate methods, Sakiadis (1961) was the first to investigate the action of boundary-layer flow caused by the motion of a flat surface through an otherwise quiescent fluid. Later, Tsou *et al.* (1967) conducted experiments to support Sakiadis' research hypotheses for Newtonian fluids and found a perfect match between the analytical predictions and measurements of the laminar velocity field.

Additional studies examining the boundary-layer flow over a moving plate include those of Kumari *et al.* (1996), Ali *et al.* (1998), Chen (1999), Elbashbeshy *et al.* (2000), and Weidman *et al.* (2006), which added impulsive velocity, temperature-dependent viscosity, transpiration, radiation impact, forced convection, and suction or injection influences, respectively.

The heat transfer problem induced by a continuous moving plane or an axisymmetric surface was studied numerically by Lee *et al.* (1972). Other researchers have periodically expanded the concept (Char *et al.*, 1990; Chiam, 1993; Al-Sanea, 2004). Bataller (2008) used the fourth-order Runge–Kutta algorithm in conjunction with the shooting method to investigate the effects of thermal radiation on the laminar boundary layer around a flat plate. Under a convective surface boundary condition, Bataller (2008) investigated the effects of thermal radiation on the laminar boundary layer around a flat plate in a uniform stream of fluid, and around a flowing plate in a quiescent ambient fluid. Aziz (2009) studied heat transfer in boundary-layer flow with a convective boundary condition. The boundary-layer flow of nanofluids over moving surfaces was investigated by Bachok *et al.* (2010). In the context of thermal radiation, Ishak *et al.* (2011) examined steady laminar boundary-layer flow over a moving plate in a fluid with convective surface boundary conditions. In this work, they combined two processes, Blasius flow and Sakiadis flow, using the composite velocity ($U = U_w + U_\infty$) introduced by Afzal *et al.* (1993). Ishak *et al.* (2011) investigated the effects of radiation on the conventional Blasius and Sakiadis flows in fluid dynamics. They discovered a reduction in the heat transfer rate in the presence of thermal radiation. Ferdows *et al.* (2012) studied the steady 2D flow of an incompressible viscous and electrically conducting nanofluid generated by stretching a sheet in the vertical direction with viscous dissipation in saturated porous media. Ferdows *et al.* (2021) analysed the effects of the suction and injection on boundary-layer viscous fluid flow and heat transfer via a moving flat plate. They found that, with an increase in suction/injection parameter, both the skin friction coefficient and Nusselt number decrease.

Nanofluids have, in recent years, been proposed as a way of improving the efficiency of heat transfer liquids. Thermal conductivity significantly influences the heat transfer coefficient between the fluid and the surface. Heat transfer fluids are employed in thermal systems to carry out heat transfer procedures. The efficiency and compactness of many engineering systems are hampered by the low thermal conductivity of convectional heat transfer fluids like water, methanol, ethylene

glycol, and engine oils (Oztop *et al.*, 2016). It is well established that the suspension of solid particles, such as millimetre or micrometre-sized particles, can improve the thermal conductivity of traditional heat transfer fluids. Adding even a small quantity (fewer than one percent by volume) of nanoparticles to conventional heat transfer liquids may increase the fluid's thermal conductivity by as much as twice that of the base fluid. Researchers and technologists have found a new class of fluid known as a nanofluid. Nanofluids are fluids in which solid nanometre-sized particles are suspended. The term "nanofluid" was first proposed by Choi (1995) to explain how solid nanoparticles are suspended in a base fluid. These dispersed nanoparticles can modify the base fluid's thermal and transport properties (Lotfi *et al.*, 2010). Enhanced thermal efficiency is provided by nanofluid once nanoparticles (e.g. *Cu*, *Ag*, *TiO₂*, and *Al₂O₃*) are mixed with a carrier fluid (e.g. water, methanol, ethylene glycol, and engine oils; Tripathi *et al.*, 2014; Darbari *et al.*, 2016; Bhatti *et al.*, 2016; Mahanthesh *et al.*, 2017; Gireesha *et al.*, 2018).

Researchers are becoming more interested in using nanofluids next to flat plates to accelerate the heat transmission rate. There are numerous studies in the literature, including those of Maïga *et al.* (2004), Buongiorno (2006), Trisaksri *et al.* (2007), Wang *et al.* (2007), Kakac *et al.* (2009), and Ahmad *et al.* (2011). Long *et al.* (2011) investigated stagnation-point flow over a shrinking or expanding nanofluid sheet. Haile *et al.* (2015) examined the boundary-layer flow of nanofluids across moving objects, considering viscous dissipation, heat transfer, and chemical reactions. The explicit mathematical solution of two-dimensional laminar flow and heat transfer of nanofluids via a microchannel with nonlinear velocity slip and temperature was studied by Zhu *et al.* (2018). A great deal of research has also been conducted to demonstrate the benefits of nanofluids by considering various effects, physical characteristics, surfaces, and shapes. Prasad *et al.* (2016), Mishra *et al.* (2018), Farooq *et al.* (2019), and He *et al.* (2020) have all published reviews on nanofluid studies.

Magnetohydrodynamics is the study of the motion of electrically conducting fluids with magnetic properties. These include both inviscid and viscous fluids. A current induced in the presence of a magnetic field in an electrically conducting fluid polarizes the liquid, and as a result, the magnetic field also changes. The fluids can be driven electrically in various applications for processing materials in chemical and mechanical engineering, and as such, they will react to an applied magnetic field. Such a system may be used to monitor, for example, the heat transfer rates in

stretched sheets and to fine-tune the final materials to industry requirements. This process takes advantage of the effect of the Lorentzian drag force that abates flows in a direction perpendicular to the magnetic field applied (i.e. transverse; Hughes & Young, 1966). Magnetohydrodynamic (MHD) boundary-layer flows also arise in applications such as MHD power generator designs, liquid metal manipulation, plasma studies, cooling of nuclear reactors, induction heating, and plasma cutting. Jafar *et al.* (2011) examined MHD flow and heat transfer over stretching or shrinking sheets with an external magnetic field. The effects of thermal radiation in MHD flow, free convection flow, and viscoelastic flow were analysed, respectively, by Chamkha (1997), Raptis (1998b), Jumah *et al.* (2001), and Mohammadein and El-Amin (2000). Recently, researchers have paid substantial attention to MHD boundary-layer flow with heat and mass transfer of nanofluids owing to the significant thermal enhancement properties exhibited by these nano-engineered liquids. Furthermore, by combining magnetic and nanofluid material properties, one can obtain magnetic nanofluids with exceptional magnetic responsive features. Magnetic actuation offers specific capabilities as it can be controlled temporally and spatially and applied externally to the device, offering a noninvasive approach to remote control.

Unsteady boundary-layer flows of nanofluids over a stretching sheet with thermal radiation in the presence of a magnetic field were numerically addressed by Ferdows *et al.* (2012). Mabood *et al.* (2015) and Mustafa *et al.* (2015) studied MHD flow and nanofluid heat transfer due to a nonlinear stretching sheet. Srinivasacharya *et al.* (2015) investigated the steady laminar MHD nanofluid flow over a wedge in a variable magnetic field. MHD boundary-layer flow of nanofluid over a continuously stretching surface was studied by Rasheed *et al.* (2017). Yohannes and Shankar (2014) successfully analysed melting heat transfer in the MHD flow of nanofluid over a permeable exponential stretching sheet. The heat and mass transfer of free convective MHD flow of Ag–kerosene oil nanofluid was elucidated by Upreti *et al.* (2020). The results showed that the heat and mass transfer rates grew consistently as the quantity of surface mass flux shifted from injection to the suction domain. Nadeem *et al.* (2019) analysed the characteristics of heat and mass transfer for the three-dimensional unsteady, laminar, and incompressible flow of a micropolar nanofluid. Kumar *et al.* (2022) analysed the impact of magnetohydrodynamics on the flow of an ethylene glycol-based nanofluid containing copper nanoparticles over an exponential stretching sheet with Navier velocity slip conditions and thermal radiation.

The free convection flow of a nanofluid in the presence of a magnetic field over a vertical semi-infinite flat plate was investigated by Hamad *et al.* (2011). The impact of thermophoresis and Brownian motion on heat transfer enhancement in natural convection of nanofluids was examined by Haddad *et al.* (2012). Daniel *et al.* (2018) studied the combined effects of thermal stratification, applied magnetic fields, and thermal radiation on a boundary-layer flow of electrically conducting nanofluid over a nonlinear stretching sheet. The radiative heat transfer is sensitive to the fluid temperature and thermal boundary-layer thickness. Das *et al.* (2016) studied the impact of thermophoresis and thermal radiation on heat and mass transfer for the second-grade fluid flow over a semi-infinite stretching sheet with convective surface heat flux. They found that the fluid velocity and temperature in the boundary-layer region rise significantly to increase the value of the thermal radiation parameter.

Most of the above research has employed the “no-slip boundary condition”, which is one of the fundamental concepts of Navier–Stokes theory. In the flow of a suspension such as foam, a polymer solution, or a nanofluid, the phenomenon of “slip” may appear on the stretching border. There are a few instances in which the no-slip criteria are inappropriate and replaced with the partial slip condition because boundary slip has many implications, like refining inside cavities besides artificial heart valves. The impact of partial slip on laminar boundary-layer flow and heat transfer over a flat surface was analysed by Martin *et al.* (2006). Navier (1827) developed a fundamental boundary condition that allows for fluid slide at a solid barrier to explain the occurrence of slip. He suggested a proportional relationship between the stress and the fluid velocity tangential to the boundary walls. Rashidi *et al.* (2014) used similarity variables to investigate mixed convective flow with MHD, slip, and thermal convective boundary conditions and a moving vertical flat surface. A numerical analysis of nanofluid flow along a straining tube in the presence of velocity slip was provided by Mukhopadhyay (2013), who observed that slip increases the temperature but decreases velocity. Aminreza *et al.* (2012) examined how slip affects boundary-layer flow and heat transfer over a stretching surface developed in the presence of nanoparticle fractions. They discovered that the slip parameter significantly reduces the Nusselt number. Wang *et al.* (2016) analysed the laminar forced convection of Al_2O_3 –water nanofluid flows with slip velocity and jump temperature conditions at a solid–fluid interface. Their numerical results demonstrate that the increase in convection along the solid–fluid interface caused by the slip velocity can significantly enhance heat transfer. Analytical studies have been carried out on

the boundary-layer flow and heat transfer of a nanofluid from a nonlinear stretching flat surface with slip boundary conditions by Adem *et al.* (2018). Mishra *et al.* (2020) examined the effects of slip on MHD boundary-layer flow through a stretching tube, including viscous–Joule heating, and considered uncertainties in the thermal conductivity and dynamic viscosity.

In fluid mechanics, viscous dissipation refers to a velocity profile distortion due to an applied viscous stress. This is presumed to be the process by which kinetic energy is transformed into the internal energy of the relevant fluid. Viscous dissipation significantly impacts natural convection in various systems that experience significant fluctuations in gravitational force or that operate at high speeds. When a magnetic field is introduced into the system, the energy released from the fluid's motion is retarded, causing the surface to heat up or cool down, significantly transferring heat to the liquid in the boundary-layer region. The conversion of mechanical energy into thermal energy is characterized by viscous dissipation. Viscous dissipation is relevant to various applications since it has led to significant temperature increases in polymer manufacturing processes like high-speed extrusion and injection modelling. The dimensionless Eckert number is used widely to describe viscous thermal dissipation of convection, particularly for forced convection (Chazal, 1972; Oosthuizen, 1999). It expresses the relationship between the kinetic energy of a flow and the enthalpy difference at the boundary layer. The energy equation is adjusted by adding a factor corresponding to the viscous dissipation effect. The impact of viscous thermal dissipation on fluid flows and heat transfer has been studied extensively by various authors. It has been observed that in fluid flows with high Eckert numbers, heat generated from viscous thermal dissipation dominates the fluid temperature; therefore, the Eckert number cannot be zero in the study of convection heat transfer. Brinkman (1951) seems to have been the first to perform a theoretical analysis of viscous dissipation.

In the presence of the combined effect of Hall and ion-slip currents for the situation of power-law fluctuation of the wall temperature, Abo-Eldahab *et al.* (2005) investigated the effects of viscous dissipation and Joule heating on MHD-free convection flow across a semi-infinite vertical flat plate. Aydin *et al.* (2006) employed numerical analysis to investigate steady laminar MHD mixed-convection heat transfer around a vertical plate while considering the effects of ohmic heating and viscous dissipation. The steady boundary-layer flow of a viscous and incompressible fluid across a moving vertical flat plate in an externally flowing liquid with viscous dissipation was

investigated theoretically by Bachok *et al.* (2013). Desale *et al.* (2015) studied boundary-layer flow with viscous dissipation and convection along a flat plate. They noticed that the temperature distribution for variable temperature rises as the Eckert number increases. Reddy *et al.* (2017) analysed the impact of viscous dissipation on MHD natural convective flow over an oscillating vertical plate. The influence of viscous dissipation on the boundary-layer flow of an electrically conducting viscoelastic fluid across a nonlinear stretching sheet was investigated numerically in the work of Jafar *et al.* (2019). Ajibade *et al.* (2020) theoretically analysed the influences of boundary plate thickness and viscous dissipation on the steady natural convection flow of an incompressible viscous fluid with variable characteristics.

There has also been a substantial increase in research into analysing the flow of nanofluids in the context of magnetic field interaction. Ferrofluids, or magnetic nanofluids, are suspensions of magnetic nanoparticles with a 5–15 nm diameter in carrier liquids like glycerol, water, ethylene glycol, or oil (Papell, 1965). Research on ferrofluids reveals that the presence of these particles significantly enhances heat transfer in the fluid flow (Neuringer, 1964; Rosensweig, 1987). Ferrofluids are strongly magnetized and display a significant rise in thermal conductivity in a magnetic field since heat is rapidly transferred through percolating ferroparticle paths. Recently, nanofluids containing ferroparticles have become significantly more important in engineering applications, including shock absorbers, magnetorheological fluids, biomedicine, printer inks, and heat transfer (Popplewell, 1984; Pankhurst, 2003; Scherer, 2005). Although performing numerical and analytical investigations of such fluids is challenging, it is crucial for industrial applications. Hard disks, revolving X-ray tubes, shafts, rods, and other components are examples of applications in electrical devices. Magnetic fluids are also used in devices such as sensors, densimeters, accelerometers, and pressure transducers (Maruno, 1983; Raj, 1990).

Tzirtzilakis *et al.* (2010) examined the forced and free convective boundary-layer flow of a magnetic fluid over a flat plate in a specific magnetic field. Finite element simulations of heat transmission to a ferrofluid in the presence of an external magnetic field were performed by Tangthieng *et al.* (1999). They studied a problem based on the flow between vertical parallel plates and in a box. They concluded that a magnetic field gradient considerably increased the heat transfer. Alternating magnetic fluids have been applied to treat cancer and tumours in the medical sciences (Feynman, 1963; Shliomis, 2004). Ferrites, such as magnetite (Fe_3O_4), cobalt ferrite

($CoFe_2O_4$), and Mn–Zn ferrite ($Mn-ZnFe_2O_4$), have a variety of uses in biomedicine, such as therapeutic applications for hyperthermia, cancer treatment, and drug delivery, as well as diagnostic tools, such as nuclear magnetic resonance imaging (Cabuil, 2004; Frey, 2009; Singamaneni, 2011; Akbarzadeh, 2012). Khan *et al.* (2015) investigated the MHD boundary-layer flow and heat transfer of ferrofluids along a flat plate with slip velocity. They concluded that, in comparison with the hydrodynamic situation, the magnetic field increases the dimensionless momentum and reduces the dimensionless surface temperature, raising the ferrofluids' skin friction and heat transfer rate. Ramil *et al.* (2017) analysed how uniform heat flux and slip influence MHD flow and heat transfer of ferrofluids across a moving flat plate. Anuar *et al.* (2019) focused on the MHD boundary-layer flow of ferrofluid via a permeable flat plate, taking into account the impacts of thermal radiation. Bognar *et al.* (2020) investigated water-based ferrofluid flow over a moving surface in a spatially varying magnetic field. They found that the velocity and temperature of a ferrofluid are affected by even a small concentration of ferroparticles. Bognar *et al.* (2020) also examined the ferromagnetic viscoelastic flow past a stretching sheet with the suction and injection effect of a magnetic dipole. Mohamed *et al.* (2021) analysed the convective heat transfer of a blood-based Casson ferrofluid on a flat surface, considering slip effects. Ferdows *et al.* (2023) studied the fluid flow, including magnetic particles, over an unstable stretching/shrinking cylinder, taking blood as the base fluid.

1.2 Identification of Problems

In recent years, much interest has been given to studying nanofluids owing to their greatly enhanced thermal conduction properties (Keblinski *et al.*, 2005). A large number of numerical and experimental studies have been carried out by numerous researchers on thermal conductivity, thermal diffusivity, viscosity, and convective heat transfer characteristics of nanofluids (Choi *et al.*, 2004; Liu *et al.*, 2005; Maiga *et al.*, 2005; Das *et al.*, 2006, 2007; Kang *et al.*, 2006; Tyler *et al.*, 2006; Tiwari & Das, 2007; Abu-Nada, 2008; Oztop & Abu-Nada, 2008; Tzou, 2008; Yu *et al.*, 2008; Choi, 2009). Nanoparticles can help extract energy from the earth's core, improve the efficiency of cooling systems employed in nuclear reactors, and help in targeted drug delivery in pharmaceuticals. Additionally, the presence of a magnetic field in a fluid (e.g. liquid metals,

electrolytes, plasma, or salt water) affects the rate at which heat is transferred in a flow system. The magnetohydrodynamics of electrically conducting fluid has an important effect on various vital processes in fields as diverse as astrophysics, geophysics, and fire engineering.

In recent years, research in the field of magnetohydrodynamics has progressed rapidly (Davidson, 2006). MHD natural convection flow is widely used in chemical engineering, reactor cooling, aeronautics, heat exchangers, and electronics. The induced magnetic field affects fluid flow configuration, and so the rate of flow must be precisely regulated. In many significant phenomena, such as cosmic rays, sunspots, geothermal energy, solar flares, and groundwater flow, the interplanetary magnetic field plays a dynamic role in studying MHD flow. Based on the problems mentioned above, a study was carried out to examine the MHD viscous flow resulting from a semi-infinite flat plate moving through electrically conducting water-based nanofluids with different metallic nanoparticles (*Cu*, *Ag*, *Al₂O₃*, and *TiO₂*) and magnetic nanoparticles (*Fe₃O₄*, *CoFe₂O₄*, and *Mn-ZnFe₂O₄*), and to explore how velocity, induced magnetic field, temperature, and concentration profiles, in addition to the skin friction coefficients and Nusselt and Sherwood numbers, are influenced by the parameters of physical problems, such as the sheet velocity parameter λ , the magnetic field parameter M , the Prandtl number Pr , the magnetic Prandtl number Prm , the thermal radiation parameter Rd , the Lewis number Le , the Brownian motion parameter Nb , the thermophoresis parameter Nt , Grashof number Gr , the Biot number Bi , the slip parameter α , the Eckert number Ec , and the nanoparticle volume percentage ϕ . An efficient MATLAB-based numerical quadrature technique known as the spectral relaxation method (Motsa, 2014) is employed to obtain solutions to boundary-layer equations and achieve a faster convergence rate.

1.3 Goals of the Thesis

The purpose of this thesis is to present theoretical investigations into the heat and mass transfer characteristics within the boundary-layer flow of nanofluids. The theoretical framework aims to provide a comprehensive understanding of the intricate interactions between nanofluid behaviour, the influence of an induced magnetic field, and the dynamics of a moving surface. The research objectives are as follows:

- Explore and analyse the free convection flow characterized by convective heat transport from both a moving flat plate and an inclined stationary or moving flat plate. The goal is to contribute insights into the interaction between free convection, plate motion, and plate inclination, enhancing our understanding of heat transfer in these configurations.
- Examine and assess the influence of various factors on boundary-layer flow, including the effects of an induced magnetic field, momentum slip condition, space- and temperature-dependent internal heat generation and absorption, and uniform heat flux. The objective is to conduct a thorough analysis of how each of these factors individually, as well as their combined effects, influences the behaviour of boundary-layer flow.
- Construct a nanoscale formulation and solve the Tiwari–Das model to investigate the material properties of specific nanoparticles and the base fluid. Use similarity transformations to convert the governing equations of the problem into sets of ordinary differential equations (ODEs) with multiple degrees, incorporating appropriate boundary conditions at the far-stream and convective wall.
- Solve the local transformed equations numerically, employing the spectral relaxation method (SRM).
- Clarify the impact of embedded physical parameters on flow distributions, skin friction, and heat and mass transfer rates within a system involving water-based metallic and magnetic nanofluids. Analyse how variations in these physical parameters, such as nanoparticle concentration and magnetic field strength, influence the overall flow patterns and the rates of skin friction, as well as heat and mass transfer.

1.4 Research Significance

This research intends to investigate the heat transfer within the external boundary layer of a fluid supplemented with various nanoparticles. A comprehensive inquiry has been undertaken to ascertain the effects of multiple nanoparticles, induced magnetic fields, and other parameter-dependent flow characteristics. Nanofluids have received much attention from researchers due to their high electrical conductivity, high melting point, low electrochemical migration behaviour, and low cost. They have various commercial and domestic applications, such as catalysis, imaging,

medical applications, energy-based research, and environmental applications. In addition, this research unequivocally establishes that the induced magnetic field influences both the momentum and thermal boundary layer thicknesses. The momentum boundary-layer thickness of a nanofluid drops when the magnetic field strength is increased, while the thermal boundary-layer thickness increases. The *Ag* nanoparticles demonstrated the highest cooling performance for the problem of a flat moving plate. This is because *Ag* has high thermal conductivity, while Al_2O_3 , *Cu*, and TiO_2 have low thermal conductivities. Moreover, the use of magnetic nanoparticles to enhance both thermal and magnetic capabilities has been investigated. The results show that Fe_3O_4 demonstrates greater fluid flow resistance and a faster heat transfer rate than $CoFe_2O_4$ and *Mn-ZnFe₂O₄*. Another significant factor is implementing the spectral relaxation method (SRM) to solve the nonlinear coupled partial differential equations (PDEs) numerically. Able to resolve large algebraic systems of equations, SRM is an iterative approach similar to the Gauss–Seidel relaxation process. Compared with other numerical and analytical techniques, SRM has been shown to be accurate, simple to apply, convergent, and highly efficient.

1.5 Structure of the Thesis

The research described in this thesis aims to provide a comprehensive overview of the MHD free-forced convective flow of water-based nanofluids containing various metallic and magnetic nanoparticles. The central results presented in the thesis originate from papers that have been published, submitted for publication, or presented at international conferences. The introduction, which comprises a literature review, an overview, and discussions of the primary goals and significance of the thesis, is included in **Chapter 1**.

The solution methodology is thoroughly outlined in **Chapter 2**. A novel method is presented for solving a set of PDEs that model the flow of unstable two-dimensional MHD flow and mass transfer over a moving flat surface. The spectral relaxation method (SRM) is an algorithm that decouples a system of nonlinear PDEs into a system of linear PDEs, which are then solved sequentially, much like the well-known Gauss–Seidel iteration. This approach is accurate, convenient, and computationally efficient.

Chapters 3 to 7 demonstrate the mathematical models created to achieve the identified research goals. **Chapter 3** investigates a theoretical model for steady MHD viscous flow resulting from the motion of a semi-infinite flat plate in an electrically conducting nanofluid. Thermal radiation, magnetic induction effects, and convective boundary conditions are included. Buongiorno's two-component nanoscale model, which features Brownian motion and thermophoresis effects, is deployed. The governing nonlinear boundary-layer equations are converted to nonlinear ODEs using suitable similarity transformations.

Chapter 4 describes a mathematical model for incompressible free convection flow with convective heat transport from an inclined stationary/moving flat plate under the impact of an induced magnetic field. The current flow model is formulated to consider different water-based nanofluids with metallic nanoparticles (copper and silver). A nanoscale formulation with the Tiwari–Das model was effectively deployed to study specific nanoparticle and base fluid material properties.

The purpose of **Chapter 5** is to investigate the combined effects of space- and temperature-dependent internal heat generation or absorption on MHD heat transfer flow. This study aims to observe boundary-layer movement in nanofluids near a flat surface under an induced magnetic field and momentum slip.

Chapter 6 concentrates on the study of the free convective heat transfer phenomena of an electrically conducting flow past a semi-infinite moving flat plate under the influence of an aligned induced magnetic field and viscous dissipation, where the flow velocity and magnetic field vectors far from the plate are parallel. The goal of this research is to determine how the Eckert number influences the heat and mass transmission rates during the simultaneous flow transfer of nanofluids containing various nanoparticles.

Chapter 7 presents a study on the influence of an induced magnetic field on the MHD heat transfer flow of water-based ferrofluids, under the influence of slip, over a moving plate subject to uniform heat flux. A transverse magnetic field is applied to the plate. The novelty of this research is to examine how an induced magnetic field affects gravity-driven flow in electrically conducting ferrofluids.

The key conclusions and observations are finally summed up in **Chapter 8**. Future research proposals are presented after identifying several open questions. A complete list of all references cited in this thesis follows Chapter 8.

Chapter 2

Spectral Relaxation Method

The numerical solution of PDEs leads to some of the most important and challenging problems in numerical analysis. Nonlinear coupled PDEs are a class of systems encompassing various physical phenomena in applied science and engineering. Several sophisticated numerical algorithms have been used to solve these equations. Many researchers have expended considerable effort to develop new numerical methods that can overcome challenges like high computation times and low convergence rates. This thesis adopts the spectral relaxation method (SRM) for the numerical solution. This approach was introduced by Motsa (2014), and has been applied by Motsa and Makukula (2013) to solve the swirling von Kármán disc flow of a Reiner–Rivlin fluid with Joule heating, viscous dissipation, and wall transpiration. It has also been implemented for thermal ignition flows of rheological rocket gel propellants by Awad *et al.* (2014) and in micropolar convective wall plumes in geothermics by Haroun *et al.* (2015).

Illustration of the solution methodology

The SRM is an iterative algorithm intended for nonlinear systems of differential equations in which some of the unknown functions have exponentially decaying profiles. The method has been shown to be efficient and convenient in solving boundary-layer problems in which at least one of the profiles, such as velocity, temperature, or concentration, decays exponentially. The SRM approach is derived by linearizing the Gauss–Seidel concept of decoupling a system of equations by a simple rearrangement of the order in which they are described and sequentially resolved. The resulting SRM iterative scheme is then implemented using the Chebyshev spectral collocation process. The use of Chebyshev polynomials provides good accuracy and fast convergence in the computations.

Consider a system of m nonlinear ODEs with m unknown functions $x_i(\xi)$, $i = 1, 2, \dots, n$ for $\xi \in [a, b]$. The vector X_i represents the derivatives of x_i with respect to ξ , that is,

$$\mathbf{X}_i(\xi) = [x_i^{(0)}, x_i^{(1)}, \dots, x_i^{(p)}, \dots, x_i^{(m_i)}] \quad (2.1)$$

in which $x_i^{(0)} = x_i$, $x_i^{(p)}$ is the p th derivative of x_i with respect to ξ , and $x_i^{(m_i)}$ is the highest derivative. The system is reformulated as a sum of its linear and nonlinear components as follows:

$$\mathcal{L}_i[X_1, X_2, \dots, X_n] + \mathcal{N}_i[X_1, X_2, \dots, X_n] = \mathcal{R}_i(\xi), \quad i = 1, 2, \dots, n \quad (2.2)$$

where \mathcal{R}_i is a known function of ξ . If the nonlinear component in equation (2.2) can be expressed as a combination of nonlinear components, with at least one of them being a multiple of x_i , we can further divide \mathcal{N}_i into a sum of two nonlinear functions:

$$\mathcal{N}_i[X_1, X_2, \dots, X_n] = x_i \mathcal{F}_i[X_1, \dots, \hat{X}_i, \dots, X_n] + \mathcal{S}_i[X_1, X_2, \dots, X_n] \quad (2.3)$$

where $\hat{X}_i = [x_i^{(1)}, \dots, x_i^{(m_i)}]$ and \mathcal{F}_i is a nonlinear function that is a factor of x_i , while \mathcal{S}_i is a nonlinear function of X_1, X_2, \dots, X_n that either has x_i absent or as a nonlinear factor.

The solution to equation (2.2) is contingent upon two-point boundary conditions, denoted as

$$\sum_{k=1}^n \sum_{p=0}^{m_k-1} \alpha_{\nu,k}^{[p]} x_k^{(p)}(a) = \mathcal{K}_{a,\nu}, \quad \nu = 1, 2, \dots, n_a \quad (2.4)$$

$$\sum_{k=1}^n \sum_{p=0}^{m_k-1} \beta_{\sigma,k}^{[p]} x_k^{(p)}(b) = \mathcal{K}_{b,\sigma}, \quad \sigma = 1, 2, \dots, n_b \quad (2.5)$$

Here, $\alpha_{\nu,k}^{[p]}$ and $\beta_{\sigma,k}^{[p]}$ indicate constant coefficients of $x_k^{(p)}$ within the boundary conditions, and n_a and n_b are consecutive boundary conditions at a and b .

To develop the iteration approach, we use the Gauss–Seidel relaxation method to decouple linear algebraic equations and use updated solutions in the solution process. From initial approximations $X_{1,0}, X_{2,0}, \dots, X_{n,0}$, the iterative approach is obtained as follows:

$$\begin{aligned} & \mathcal{L}_1[X_{1,r+1}, X_{2,r}, \dots, X_{n,r}] + x_{1,r+1} \mathcal{F}_1[\hat{X}_{1,r}, X_{2,r}, \dots, X_{n,r}] \\ & \quad = \mathcal{R}_1 - \mathcal{S}_1[X_{1,r}, X_{2,r}, \dots, X_{n,r}] \\ & \mathcal{L}_2[X_{1,r+1}, X_{2,r+1}, X_{3,r}, \dots, X_{n,r}] + x_{2,r+1} \mathcal{F}_2[X_{1,r+1}, \hat{X}_{2,r}, X_{3,r}, \dots, X_{n,r}] \\ & \quad = \mathcal{R}_2 - \mathcal{S}_2[X_{1,r+1}, X_{2,r}, \dots, X_{n,r}] \\ & \mathcal{L}_{n-1}[X_{1,r+1}, \dots, X_{n-1,r+1}, X_{n,r}] + x_{n-1,r+1} \mathcal{F}_{n-1}[X_{1,r+1}, \dots, X_{n-2,r+1}, \hat{X}_{n-1,r}, X_{n,r}] \\ & \quad = \mathcal{R}_{n-1} - \mathcal{S}_{n-1}[X_{1,r+1}, \dots, X_{n-2,r+1}, X_{n-1,r}, X_{n,r}] \end{aligned}$$

$$\begin{aligned} & \mathcal{L}_n[X_{1,r+1}, \dots, X_{n-1,r+1}, X_{n,r+1}] + x_{n-1,r+1} \mathcal{F}_n[X_{1,r+1}, \dots, X_{n-1,r+1}, \hat{X}_{n,r}] \\ & = \mathcal{R}_n - \mathcal{S}_n[X_{1,r+1}, \dots, X_{n-1,r+1}, X_{n,r}] \end{aligned} \quad (2.6)$$

This is a system of n decoupled linear equations. The goal is to solve them iteratively for different values of $r = 1, 2, \dots$ starting from an initial approximation $X_{i,0}$. Here $X_{i,r+1}$ and $X_{i,r}$ are the estimated values of X_i at the current and prior iterations, respectively. The iterative process typically involves updating the values of $X_{i,r+1}$ based on the previous approximations $X_{i,r}$ and the given equations. This process continues until convergence is achieved or until a predefined stopping criterion is met. The specific details of the iterative method, such as the update rule and convergence criteria, would depend on the context and the nature of equation (2.6). The convergence criteria are evaluated by examining the error arising from the decoupling and subsequent solution of the governing equations. This error, denoted as E_d at the $(r + 1)$ th iteration, is determined using the following formula:

$$E_d = \max \left(\|x_{1,r+1} - x_{1,r}\|_{\infty}; \|x_{2,r+1} - x_{2,r}\|_{\infty}; \dots; \|x_{n,r+1} - x_{n,r}\|_{\infty} \right)$$

The strategy stated above for decoupling a linear algebraic system of equations is analogous to the Gauss–Seidel relaxation method. Applying this algorithm leads to a series of linear differential equations with variable coefficients that are solved here using Chebyshev spectral collocation methods (Shateyi *et al.*, 2013; Awad *et al.*, 2014; Haroun *et al.*, 2015). Due to their relatively high precision and efficiency, spectral methods are used here in the discretization and for the subsequent solution of variable-coefficient linear differential equations with smooth solutions over a simple domain. There is currently a substantial quantity of literature on the practical application of spectral collocation methods, notably the works by Mosayebidorcheh *et al.* (2018), Fakhar *et al.* (2020), Arain *et al.* (2021), Rasool *et al.* (2022).

To apply the spectral method, the physical region $[0, \infty]$ is transformed into the domain $[-1, 1]$, employing the domain truncation process in which the problem is solved on the truncated interval $[0, L]$, where L is a finite number selected to be large enough to illustrate the behavior of the flow properties when ξ is large. The mapping of intervals from $[0, L]$ to $[-1, 1]$ is done using the transformation

$$\frac{\xi}{L} = \frac{\tau + 1}{2}, -1 < \tau < 1$$

Applying the spectral collocation method, the unknown functions are determined at $N + 1$ collocation points by demanding that the decoupled equations be satisfied precisely. A suitable set of collocation points is the Gauss–Lobatto points, defined on $[-1, 1]$ by

$$\tau_j = \cos\left(\frac{\pi j}{N}\right), \quad j = 0, 1, 2, \dots, N; \quad -1 < \tau < 1$$

The derivatives of the unknown variables at the collocation points are approximated by applying a differentiation matrix \mathbf{D} of size $(N + 1) \times (N + 1)$ as the matrix–vector product of the form

$$\frac{dx_i}{d\xi} = \sum_{j=0}^N \mathbf{D}_{lj} x_i(\tau_j) = \mathbf{D}\mathbf{X}_i, \quad l = 0, 1, 2, \dots, N$$

where $\mathbf{D} = \frac{2\mathbf{D}}{L}$ and $\mathbf{X} = [x(\tau_0), x(\tau_1), \dots, x(\tau_N)]^T$ is the vector function at the collocation points.

Higher-order derivatives are obtained as powers of \mathbf{D} , that is,

$$x_k^{(p)} = \mathbf{D}^p \mathbf{X}_k$$

where p is the order of the derivative. Depending on the nature of the interpolating polynomials employed in the collocation process, the elements of \mathbf{D} can be evaluated with various methods (Canuto *et al.*, 1988; Don *et al.*, 1995; Trefethen, 2000; Weideman *et al.*, 2000; Boyd, 2001). The method used by Trefethen (2000) in the `cheb.m` Matlab code is applied in this thesis.

To implement the Chebyshev differentiation method for the governing equation (2.1) and the iteration scheme (2.6), we note that (2.1) can be expressed in an analogous form,

$$\sum_{k=1}^n \sum_{p=0}^{m_k} \gamma_{i,k}^{[p]} x_k^{(p)} + \mathcal{N}_i[X_1, X_2, \dots, X_n] = \mathcal{R}_i \quad (2.7)$$

where $\gamma_{i,k}^{[p]}$ are the constant coefficients of $x_k^{(p)}$, the differential of x_k ($k = 1, 2, \dots, n$) emerging in the i th iteration for $i = 1, 2, \dots, n$. Therefore, with respect to the notation employed in (2.7), the iteration scheme delineated in (2.6), for $i = 1, 2, \dots, n$, can be succinctly described as

$$\begin{aligned}
& \sum_{k=1}^i \sum_{p=0}^{m_k} \gamma_{i,k}^{[p]} x_{k,r+1}^{(p)} + x_{i,r+1} \mathcal{F}_i [X_{1,r+1}, \dots, X_{i-1,r+1}, \hat{X}_{i,r}, X_{i+1,r}, \dots, X_{n,r}] \\
& = \mathcal{R}_i - \sum_{k=i+1}^n \sum_{p=0}^{m_k} \gamma_{i,k}^{[p]} x_{k,r}^{(p)} + \mathcal{S}_i [X_{1,r+1}, \dots, X_{i-1,r+1}, X_{i,r}, \dots, X_{n,r}]
\end{aligned} \tag{2.8}$$

By using (2.2) in (2.8) and incorporating the relevant boundary conditions, we derive the spectrum relaxation method (SRM) iteration scheme as

$$\begin{aligned}
& \sum_{k=1}^i \sum_{p=0}^{m_k} \gamma_{i,k}^{[p]} \mathbf{D}^p \mathbf{X}_{k,r+1} + x_{i,r+1} \mathcal{F}_i [\mathbf{X}_{1,r+1}, \dots, \mathbf{X}_{i-1,r+1}, \hat{\mathbf{X}}_{i,r}, \mathbf{X}_{i+1,r}, \dots, \mathbf{X}_{n,r}] \\
& = \mathcal{R}_i - \sum_{k=i+1}^n \sum_{p=0}^{m_k} \gamma_{i,k}^{[p]} \mathbf{D}^p \mathbf{X}_{k,r} + \mathcal{S}_i [\mathbf{X}_{1,r+1}, \dots, \mathbf{X}_{i-1,r+1}, \mathbf{X}_{i,r}, \dots, \mathbf{X}_{n,r}]
\end{aligned} \tag{2.9}$$

subject to

$$\sum_{k=1}^n \sum_{p=0}^{m_k-1} \alpha_{\nu,k}^{[p]} \sum_{j=0}^N \mathbf{D}^p {}_N j x_{k,r+1}(\tau_j) = \mathcal{K}_{a,\nu}, \quad \nu = 1, 2, \dots, n_a \tag{2.10}$$

$$\sum_{k=1}^n \sum_{p=0}^{m_k-1} \beta_{\sigma,k}^{[p]} \sum_{j=0}^N \mathbf{D}^p {}_0 j x_{k,r+1}(\tau_j) = \mathcal{K}_{b,\sigma}, \quad \sigma = 1, 2, \dots, n_b \tag{2.11}$$

Hence, the SRM algorithm for self-similar boundary-layer problems can be stated as follows:

- 1) The governing nonlinear equations are sorted in a specific order, starting with the set of equations with the fewest unknowns. The ordered equations are labelled with $f_i(\eta)$, $i = 1, 2, \dots, m, \eta \in [a, b]$, where each $f_i(\eta)$ is the unknown function associated with the highest-order derivative in the i th equation.
- 2) The iteration scheme is developed by assuming that $f_1(\eta)$ is known from an initial guess, then arranging the converted equations in a specific order, with the equations with the fewest unknowns first.
- 3) An iteration scheme is constructed by assuming that only linear terms in f_1 (1st equation) are to be evaluated at the current iteration level (denoted by $r + 1$), and that all other terms (linear and nonlinear) in f_2, f_3, \dots are assumed to be known from the previous iteration (denoted by r). Nonlinear terms in f_1 are also computed during the preceding iteration.

- 4) Comparably, in creating the iteration scheme for f_2 (2nd equation), only linear terms are used, with all other terms aside from f_1 , which is already known from the first equation's solution evaluated at the prior level.
- 5) The updated solutions for f_{i-1} from the preceding $i - 1$ equations are used to repeat this process in the i th equation ($i = 3, 4, \dots$).
- 6) The iteration schemes for the other governing dependent variables are created similarly, using the updated solutions of the variables obtained in the previous equation.
- 7) The iteration is repeated until convergence is achieved. Errors resulting from decoupling and solving the governing equations can then be used to evaluate the intended convergence. The formula below establishes the error E_d at the $(r + 1)$ th iteration:

$$E_d = \max \left(\|f_{1,r+1} - f_{1,r}\|_{\infty}; \|f_{2,r+1} - f_{2,r}\|_{\infty}; \dots; \|f_{m,r+1} - f_{m,r}\|_{\infty} \right)$$

The SRM approach can quickly solve an extensive range of PDEs and ODEs compared with older techniques. Below are some of its key advantages:

- 1) The outcomes are relatively precise for coupled systems of equations.
- 2) It yields smaller matrices, which leads to greater accuracy.
- 3) CPU times are of the order of several minutes, and the solutions converge quickly.
- 4) It drastically reduces the number of iterative steps needed to achieve a convergent result.

However, the SRM also has some limitations:

- 1) It can be sluggish, prolonging the period needed to obtain reliable results.
- 2) It is inapplicable to power-law equations and boundary conditions with all zero values.

Chapter 3

Spectral Relaxation Simulation of Electroconductive Radiative Nanofluid Flow with Magnetic Induction over a Moving Surface

This chapter presents an MHD induction–convection model of an electrically conducting nanofluid flowing over a moving semi-infinite stretching surface with appreciable thermal radiative heat transfer. The novelty of the present simulations is the use of a spectral relaxation method (SRM) and the combination of electromagnetic induction, moving sheet velocity effects, nonlinear radiative flux (for high-temperature material processing), and heat and mass transfer. The Rosseland diffusion flux model is deployed for optically thick magnetic nanofluids (Khan *et al.*, 2013; Beg *et al.*, 2014). Using suitable similarity transformations, the momentum and energy equations are converted into dimensionless coupled ODEs and solved with the SRM technique (Beg *et al.*, 2014, 2016; Haroun *et al.*, 2015). Validation against the earlier study of Shateyi and Prakash (2014) is included. The effects of embedded parameters, i.e. the moving sheet velocity parameter λ , magnetic field parameter β , Prandtl number Pr , magnetic Prandtl number Prm , thermal radiation parameter Rd , Lewis number Le , Brownian motion parameter Nb , and thermophoresis parameter Nt on velocity, induced magnetic field, temperature, nanoparticle concentration, skin friction, local Nusselt number, and Sherwood number profiles, are visualized. The simulations are relevant to multiphysical magnetic nanoliquid material processing (Ali *et al.*, 2018).

3.1 Governing Equations for Magnetic Induction Nanofluid Flow

Consider the 2D, steady, viscous MHD thermal-convection boundary-layer flow of an electrically conducting nanofluid over a moving semi-infinite surface (sheet). The physical model is shown in Fig. 3.1. A uniform magnetic field of force H_0 is applied to the surface in the

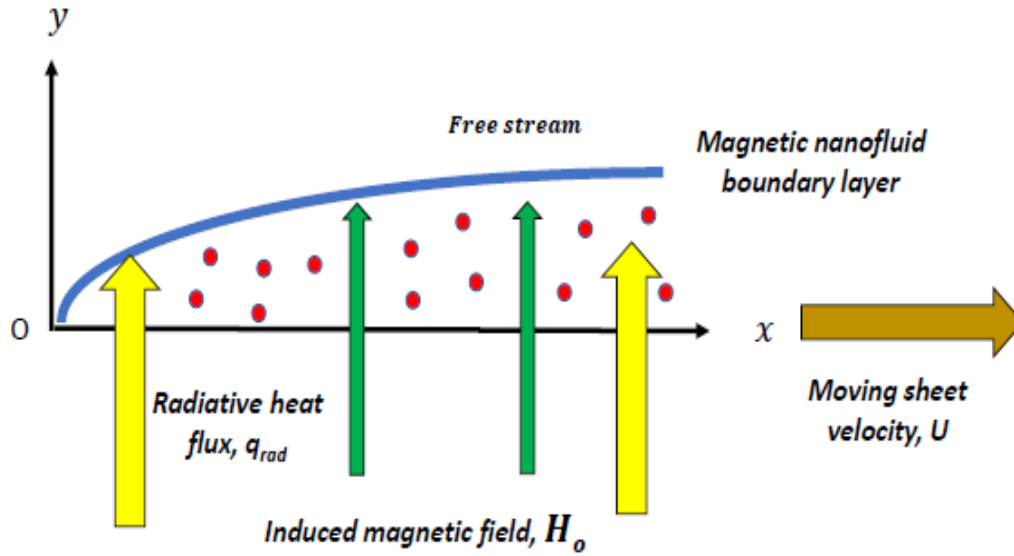


Fig. 3.1 Magnetic induction nanofluid radiative convection physical model

normal direction. In contrast, the normal component of the induced magnetic field H_2 vanishes as it hits the wall, and the parallel component H_1 approaches the value of H_0 . It is also assumed that the velocity of the free stream is U and that of the plate (sheet) is $U_w = \lambda U$. Maxwell displacement current, Hall current, viscous and ohmic dissipation, and chemical reaction effects are neglected. Under the boundary-layer approximations, using the Buongiorno two-component nanoscale model (Buongiorno, 2006), as elaborated in detail by Beg (2018), and the Rosseland diffusion flux model for radiative transfer (Beg *et al.*, 2014; Ferdows *et al.*, 2014; Uddin *et al.*, 2015), the conservation equations can be written as follows:

Mass:

$$\frac{\partial u}{\partial x} + \frac{\partial v}{\partial y} = 0 \quad (3.1)$$

$$\frac{\partial H_1}{\partial x} + \frac{\partial H_2}{\partial y} = 0 \quad (3.2)$$

Momentum: (3.3)

$$u \frac{\partial u}{\partial x} + v \frac{\partial u}{\partial y} = \nu \frac{\partial^2 u}{\partial y^2} + \frac{\mu_0}{\rho} \left(H_1 \frac{\partial H_1}{\partial x} + H_2 \frac{\partial H_1}{\partial y} \right)$$

Induced magnetic field: (3.4)

$$u \frac{\partial H_1}{\partial x} + v \frac{\partial H_1}{\partial y} - H_1 \frac{\partial u}{\partial x} - H_2 \frac{\partial u}{\partial y} = \alpha_1 \frac{\partial^2 H_1}{\partial y^2}$$

Thermal energy: (3.5)

$$u \frac{\partial T}{\partial x} + v \frac{\partial T}{\partial y} = \alpha \frac{\partial^2 T}{\partial y^2} - \frac{\alpha}{K} \frac{\partial q_r}{\partial y} + \tau \left[D_B \frac{\partial C}{\partial y} \frac{\partial T}{\partial y} + \left(\frac{D_T}{T_\infty} \right) \left(\frac{\partial T}{\partial y} \right)^2 \right]$$

Nanoparticles: (3.6)

$$u \frac{\partial C}{\partial x} + v \frac{\partial C}{\partial y} = D_B \frac{\partial^2 C}{\partial y^2} + \frac{D_B}{T_\infty} \frac{\partial^2 T}{\partial y^2}$$

The radiative heat flux q_r is evaluated by using the Rosseland diffusion approximation (Hossain & Takhar, 1996) and, following Raptis (1998a) among other researchers, is found to be

$$q_r = \frac{4\sigma^*}{3K_s} \frac{\partial T^4}{\partial y} \quad (3.7)$$

where σ^* and K_s are the Stefan–Boltzmann constant and the Rosseland mean absorption coefficient, respectively. The temperature differences within the flow are sufficiently small under the assumption that T^4 can be approximated as a linear combination of the temperature, as shown in Chamakha (1997). Expanding T^4 as a Taylor series about T_∞ and neglecting the higher-order terms, we obtain

$$T^4 \cong 4T_\infty^3 T - 3T_\infty^4 \quad (3.8)$$

Using (3.7) and (3.8) in equation (3.5), we obtain

$$\frac{\partial q_r}{\partial y} = -\frac{16\sigma^*T_\infty^3}{3K_s} \frac{\partial^2 T}{\partial y^2} \quad (3.9)$$

The prescribed boundary conditions at the wall (plate) and in the free stream for equations (3.1)–(3.6) are defined as follows:

$$u = \lambda U, \quad v = 0, \quad \frac{\partial H_1}{\partial y} = H_2 = 0, \quad T = T_w, \quad C = C_w \quad \text{at } y = 0 \quad (3.10a)$$

$$u \rightarrow U, \quad H_1 \rightarrow H_0, \quad T \rightarrow T_\infty, \quad C \rightarrow C_\infty \quad \text{at } y \rightarrow \infty \quad (3.10b)$$

We now introduce the following similarity transformations to normalize the boundary-layer equations:

$$\left. \begin{aligned} \psi &= (2Uvx)^{\frac{1}{2}} f(\eta), \quad \Phi = \left(\frac{2vx}{U}\right)^{\frac{1}{2}} H_0 g(\eta), \quad \eta = \left(\frac{U}{2vx}\right)^{\frac{1}{2}} y \\ \theta(\eta) &= \frac{T - T_\infty}{T_w - T_\infty}, \quad \phi(\eta) = \frac{C - C_\infty}{C_w - C_\infty} \end{aligned} \right\} \quad (3.11)$$

Here, ψ is the stream function, which is defined by $u = \frac{\partial \psi}{\partial y}$ and $v = -\frac{\partial \psi}{\partial x}$, and Φ is the magnetic stream function, defined by $H_1 = \frac{\partial \Phi}{\partial y}$ and $H_2 = -\frac{\partial \Phi}{\partial x}$. Mass conservation (3.1) and magnetic field continuity (3.2) are satisfied identically. Substituting the similarity variables into equations (3.3)–(3.6) gives the following nonlinear similarity momentum, magnetic, thermal, and species (nanoparticle) boundary-layer ODEs:

$$f''' + ff'' - \beta gg'' = 0 \quad (3.12)$$

$$\frac{1}{Prm} g''' + fg'' - gf'' = 0 \quad (3.13)$$

$$\left(\frac{3+4Rd}{Pr}\right) \theta'' + f\theta' + Nb\theta'\phi' + Nt\theta'^2 = 0 \quad (3.14)$$

$$\phi'' + Lef\phi' + \frac{Nt}{Nb}\theta'' = 0 \quad (3.15)$$

The dimensionless boundary conditions for the tenth-order problem now become

$$f(0) = 0, f'(0) = \lambda, g(0) = g''(0) = 0, \theta(0) = 1, \phi(0) = 1 \text{ as } \eta = 0 \quad (3.16a)$$

$$f' \rightarrow 1, g' \rightarrow 1, \theta \rightarrow 0, \phi \rightarrow 0 \text{ as } \eta \rightarrow \infty \quad (3.16b)$$

Here, primes denote differentiation with respect to η , $Pr = \frac{\nu}{\alpha}$ is the Prandtl number, $Prm = \frac{\nu}{\alpha_1}$ is the magnetic Prandtl number, $\beta = \frac{\mu_0 H_0^2}{\rho U^2}$ is the magnetic body force number, $Rd = \frac{4\sigma^* T_\infty^3}{K K_s}$ is the radiation parameter, $Nb = \frac{\tau_{DB}}{\nu} (C_w - C_\infty)$ is the Brownian motion parameter, $Nt = \frac{\tau_{DT}}{\nu T_\infty} (T_w - T_\infty)$ is the thermophoresis parameter, and $Le = \frac{\nu}{D_B}$ is the Lewis number. The physical quantities of interest in magnetic materials processing are the skin friction coefficient C_f , the local Nusselt number Nu_x , and the local Sherwood number Sh_x . These parameters characterize the surface drag, wall heat transfer rate, and wall nanoparticle mass transfer rate, respectively. The skin friction coefficient is defined as

$$C_f = \frac{\tau_w}{\rho U^2} \quad (3.17)$$

Here, τ_w is the shear stress at the surface of the wall (sheet), which is given by

$$\tau_w = \mu \left[\frac{\partial u}{\partial y} \right]_{y=0} = \rho U^{\frac{3}{2}} \sqrt{\frac{\nu}{2x}} f''(0) \quad (3.18)$$

Using equation (3.18) in (2.17), we obtain the dimensionless skin friction coefficient (surface drag) as

$$\sqrt{2Re_x} C_f = f''(0) \quad (3.19)$$

The Nusselt number is defined as

$$Nu_x = \frac{xq_w}{K(T_w - T_\infty)} \quad (3.20)$$

where the heat transfer rate at the surface is given by

$$q_w = -K \left[\frac{\partial T}{\partial y} \right]_{y=0} = -K(T_w - T_\infty) \sqrt{\frac{U}{2\nu x}} \theta'(0) \quad (3.21)$$

Using equation (3.21) in (3.20), the dimensionless wall heat transfer rate is obtained as

$$\sqrt{\frac{2}{Re_x}} Nu_x = -\theta'(0) \quad (3.22)$$

The nanoparticle mass transfer rate at the surface is given by

$$q_m = -D_B \left[\frac{\partial C}{\partial y} \right]_{y=0} = -D_B(C_w - C_\infty) \sqrt{\frac{U}{2\nu x}} \phi'(0) \quad (3.23)$$

The Sherwood number is defined as

$$Sh_x = \frac{xq_m}{D_B(C_w - C_\infty)} \quad (3.24)$$

From equations (3.23) and (3.24), the dimensionless nanoparticle mass transfer rate becomes

$$\sqrt{\frac{2}{Re_x}} Sh_x = -\phi'(0) \quad (3.25)$$

Here, $Re_x = \frac{Ux}{\nu}$ is the local Reynolds number. According to Bachok *et al.* (2010), $Re_x^{-1/2} Nu_x$ and $Re_x^{-1/2} Sh_x$ are referred to as the reduced Nusselt number and reduced Sherwood number, which are represented by $-\theta'(0)$ and $-\phi'(0)$, respectively.

3.2 Computational Solution with the Spectral Relaxation Method

The SRM algorithm, when applied to the transformed equations (3.12)–(3.15), can be summarized as follows:

- 1) The order of the velocity and induced magnetic equations is reduced by introducing the transformation $f'(\eta) = F(\eta)$ and $g'(\eta) = G(\eta)$, and the original equations are expressed in terms of $F(\eta)$ and $G(\eta)$.
- 2) The iteration scheme is developed by assuming that only linear terms in $F(\eta)$ and $G(\eta)$ are to be evaluated at the current iteration level (denoted by $F_{r+1}(\eta)$ and $G_{r+1}(\eta)$), and all other terms (linear and nonlinear) in $f(\eta)$ and $g(\eta)$ are assumed to be known from the previous iteration (denoted by $f_r(\eta)$ and $g_r(\eta)$). Nonlinear terms in $F(\eta)$ and $G(\eta)$ are also calculated at the previous iteration.
- 3) The process is repeated for the other governing variables using the updated solutions of the variables determined in the previous equation.

To apply the SRM to the nonlinear ODEs, we define $f'(\eta) = F(\eta)$ and $g'(\eta) = G(\eta)$ and then express the problem as the following set of equations:

$$f' = F$$

$$F'' + fF' - \beta gG' = 0$$

$$g' = G$$

$$\frac{1}{Prm} G'' + fG' - gG' = 0$$

$$\frac{1+Rd}{Pr} \theta'' + f\theta' + Nb\theta'\phi' + Nt\theta'^2 = 0$$

$$\phi'' + Lef\phi' + \frac{Nt}{Nb}\theta'' = 0$$

The associated boundary conditions become

$$f(0) = 0, \quad F(0) = \lambda, \quad g(0) = 0, \quad G'(0) = 0, \quad \theta(0) = 1, \quad \phi(0) = 1$$

$$F(\infty) = 1, \quad G(\infty) = 1, \quad \theta(\infty) = 0, \quad \phi(\infty) = 0$$

In the context of the SRM algorithm, we obtain the following iteration scheme:

$$F''_{r+1} + f_r F'_{r+1} = \beta g_r G'_r \tag{3.26}$$

$$f'_{r+1} = F_{r+1} \quad (3.27)$$

$$\frac{1}{Prm} G''_{r+1} + f_{r+1} G'_{r+1} - g_r G'_{r+1} = 0 \quad (3.28)$$

$$g'_{r+1} = G_{r+1} \quad (3.29)$$

$$\frac{1+Rd}{Pr} \theta''_{r+1} + f_{r+1} \theta'_{r+1} + Nb \theta'_{r+1} \phi'_r = -Nt \theta_r'^2 \quad (3.30)$$

$$\phi''_{r+1} + Le f_{r+1} \phi'_{r+1} = -\frac{Nt}{Nb} \theta_{r+1}'' \quad (3.31)$$

subject to the boundary conditions

$$F_{r+1}(0) = \lambda, F_{r+1}(\infty) = 1 \quad (3.32)$$

$$f_{r+1}(0) = 0 \quad (3.33)$$

$$G'_{r+1}(0) = 0, G'_{r+1}(\infty) = 1 \quad (3.34)$$

$$g_{r+1}(0) = 0 \quad (3.35)$$

$$\theta_{r+1}(0) = 1, \theta_{r+1}(\infty) = 0 \quad (3.36)$$

$$\phi_{r+1}(0) = 1, \phi_{r+1}(\infty) = 0 \quad (3.37)$$

To solve equations (3.26)–(3.37), we discretize them using the Chebyshev spectral method. Applying the Chebyshev pseudo-spectral method to equations (3.32) to (3.37), we obtain

$$A_1 \mathbf{F}_{r+1} = R_1, \quad F_{r+1}(\tau_N) = \lambda, F_{r+1}(\tau_0) = 1 \quad (3.38)$$

$$A_2 \mathbf{f}_{r+1} = R_2, \quad f_{r+1}(\tau_N) = 0 \quad (3.39)$$

$$A_3 \mathbf{G}_{r+1} = R_3, \quad G'_{r+1}(\tau_N) = 0, G_{r+1}(\tau_0) = 1 \quad (3.40)$$

$$A_4 \mathbf{g}_{r+1} = R_4, \quad g_{r+1}(\tau_N) = 0 \quad (3.41)$$

$$A_5 \mathbf{\theta}_{r+1} = R_5, \quad \theta_{r+1}(\tau_N) = 0, \theta_{r+1}(\tau_0) = 1 \quad (3.42)$$

$$A_6 \mathbf{\phi}_{r+1} = R_6, \quad \phi_{r+1}(\tau_N) = 0, \phi_{r+1}(\tau_0) = 1 \quad (3.43)$$

Here,

$$A_1 = \mathbf{D}^2 + \text{diag}[\mathbf{f}_r], \quad R_1 = \beta \mathbf{g}_r \mathbf{G}'_r \quad (3.44)$$

$$A_2 = \mathbf{D}, \quad R_2 = \mathbf{F}_{r+1} \quad (3.45)$$

$$A_3 = \frac{1}{Prm} \mathbf{D}^2 + \text{diag}[\mathbf{f}_{r+1} - \mathbf{g}_r] \mathbf{D}, \quad R_3 = \mathbf{O} \quad (3.46)$$

$$A_4 = \mathbf{D}, \quad R_4 = \mathbf{G}_{r+1} \quad (3.47)$$

$$A_5 = \left(\frac{1+Rd}{Pr} \right) \mathbf{D}^2 + \text{diag}[\mathbf{f}_{r+1} + Nb] \mathbf{D}, \quad R_5 = -Nt \boldsymbol{\theta}'_r{}^2 \quad (3.48)$$

$$A_6 = \mathbf{D}^2 + \text{diag}[Le \mathbf{f}_{r+1}] \mathbf{D}, \quad R_6 = -\frac{Nt}{Nb} \boldsymbol{\theta}''_r \quad (3.49)$$

In equations (3.38) to (3.43), the size of the matrix \mathbf{O} is $(N + 1) \times 1$, $\text{diag} []$ is a diagonal matrix of size $(N + 1) \times (N + 1)$, where N is the number of grid points, and \mathbf{f} , \mathbf{g} , \mathbf{F} , \mathbf{G} , $\boldsymbol{\theta}$, and $\boldsymbol{\phi}$ are the values of f , g , F , G , θ , and ϕ , respectively, evaluated at the grid points. The subscript r denotes the iteration number. Equations (3.38) to (3.43) constitute the SRM scheme and can be solved using the spectral collocation method starting from the following initial conditions, which are chosen to satisfy the boundary conditions:

$$\left. \begin{aligned} f_0(\eta) &= \eta + (\lambda - 1)(1 - e^{-\eta}), & F_0(\eta) &= 1 + (\lambda - 1)e^{-\eta}, \\ G_0(\eta) &= 1, & g_0(\eta) &= \eta, & \theta_0(\eta) &= e^{-\eta}, & \phi_0(\eta) &= e^{-\eta} \end{aligned} \right\} \quad (3.50)$$

3.3 Validation of the Spectral Relaxation Method

The nonlinear boundary value problem is defined by equations (3.12) to (3.15) subject to the boundary conditions (3.16a) to (3.16b), and is solved numerically using the SRM. The SRM results are obtained here using $N = 50$ collocation points, and the infinity value η_∞ is taken as 15. This study adopts the following default parameter values for computations: $Pr = 0.7$, $Prm = 0.5$, $\lambda = 0.1$, $\beta = 0.1$, $Nt = 0.1$, $Nb = 0.3$, $Rd = 0.5$, and $Le = 5$. These data correspond to metallic nanofluids in base fluids, which reduce the Prandtl number, have strong magnetic induction, appreciable radiative flux, and species diffusivity twice the thermal diffusivity ($Le = 0.5$), following Daniel *et al.* (2018; for radiative effect), Das *et al.* (2007), Beg *et al.* (2014), Uddin *et al.* (2015), Aly and Sayed (2017; for nanofluids), and Hughes and Young (1966; for

electromagnetic drag and induction effects). All data are realistic and apply to the case studied, that is, magnetic nanofluid stretching sheet flow for coating. All results, therefore, conform to these values unless explicitly stated otherwise. To verify the accuracy of the SRM, the results are compared with the earlier solutions of Shateyi and Prakash (2014) and shown in Table 3.1 for skin friction $-f''(0)$ with different values of the sheet velocity parameter λ . Close agreement is achieved, verifying the accuracy of the present SRM code.

Table 3.1 Comparison of SRM solutions for $-f''(0)$ when $Pr = 0.7$, $Prm = 0.5$, $\beta = 0.1$, $Nt = 0.1$, $Nb = 0.3$, $Rd = 0.5$, and $Le = 5$

λ	SRM	Shateyi and Prakash (2014)
0.1	0.46251223	0.46251223
0.2	0.44315478	0.44315478
0.4	0.37509516	0.37509516
0.5	0.32874112	0.32874112

3.4 Results and Discussion

Extensive computations have been conducted in MATLAB, and SRM solutions are shown in Tables 3.2–3.4 and Figs. 3.2–3.18. Table 3.2 presents the effects of Prandtl number Pr , radiation parameter Rd , moving surface (sheet velocity) parameter λ , Lewis number Le , Brownian motion parameter Nb , and thermophoresis parameter Nt on the skin friction coefficient C_f , the reduced Nusselt number Nu , and the reduced Sherwood number Sh . It is observed that the rate of heat transfer at the surface increases with the Prandtl number: a lower thermal conductivity of the magnetic nanofluid reduces temperatures in the boundary layer and promotes heat transfer to the wall. In contrast, the rate of mass transfer falls as the Prandtl number increases: the nanoparticle concentration is increased in the boundary-layer regime, which decreases the rate of nanoparticle mass transfer to the wall.

Increasing the Lewis number Le and the radiation parameter Rd increases the reduced Sherwood number at the border. This is because a larger Lewis number implies higher thermal diffusivity

relative to the nanoparticle mass diffusivity, which boosts nanoparticle concentrations in the fluid regime and suppresses transport to the wall. However, this reduces the heat transfer rate at the border, because a higher radiative flux elevates temperatures in the boundary layer, which decreases heat transfer to the wall. It is also evident that increasing the moving surface parameter value λ decreases the skin friction at the wall plate, since this inhibits boundary-layer growth and destroys momentum, leading to deceleration. This also increases the reduced Nusselt and Sherwood numbers, that is, it significantly enhances heat and nanoparticle diffusion to the wall.

Increases in the Brownian motion parameter Nb and thermophoresis parameter Nt have no substantial influence on the skin friction coefficient. However, the rate of heat and mass transfer at the wall increases as the Brownian motion parameter increases, which corresponds to smaller nanoparticles and encourages thermal and species diffusion to the boundary. Both the Nusselt number and the Sherwood number are reduced as the values of the thermophoresis parameter increase since temperatures and nanoparticle concentration magnitudes in the boundary layer are elevated, and this mitigates transfer to the wall, as noted by many other researchers, such as Hamad *et al.* (2011) and Haddad *et al.* (2012). Table 3.3 depicts the heat transfer rate for various values of the Prandtl number Pr with other flow parameters constrained. The reduced Nusselt number increases with negative wall velocity at all Prandtl number values.

Table 3.2 Skin friction coefficient C_f , the reduced Nusselt number Nu , and the reduced Sherwood number Sh with $Prm = 0.71$, $\beta = 0.1$

Pr	Le	Rd	λ	Nb	Nt	$f''(0)$	$-\theta'(0)$	$-\phi'(0)$
1	2	1	0.1	0.1	0.1	0.43850546	0.24324811	0.62176714
2	2	1	0.1	0.1	0.1	0.43850546	0.32268809	0.59315154
1	10	1	0.1	0.1	0.1	0.43850546	0.24543873	1.20585872
1	2	2	0.1	0.1	0.1	0.43850546	0.20192103	0.63398262
1	2	1	0.5	0.1	0.1	0.30817145	0.27678430	0.84214287
1	2	1	0.1	0.5	0.1	0.43850546	0.27990286	0.64700386
1	2	1	0.1	0.1	0.5	0.43850546	0.23536033	0.49264088

Table 3.3 Reduced Nusselt number Nu with $Prm = 0.71$, $\beta = 0.1$, $Le = 1$, $Nb = Nt = 0.3$, $Rd = 1$

λ	$-\theta'(0), Pr = 0.71$	$-\theta'(0), Pr = 5$	$-\theta'(0), Pr = 10$
-0.3	0.17039064	0.27824451	0.30238506
0.1	0.22008309	0.46040570	0.54910057
0.5	0.24559296	0.56481218	0.69755154
1	0.26900089	0.66560004	0.84272786
1.5	0.28787633	0.74959618	0.96437941
2	0.30409146	0.82329138	1.07133585

Table 3.4 lists the mass transfer rate (the reduced Sherwood number) for different Lewis numbers with other parameters constant. The reduced Sherwood number decreases with an increasing Lewis number for negative wall velocity, whereas it rapidly increases with Lewis number for the positive wall velocity case.

Table 3.5 demonstrates the influence of the magnetic force parameter β on the skin friction coefficient C_f for different values of the sheet velocity parameter λ . It can be seen that the skin friction coefficient reduces rapidly as these parameters are increased.

Table 3.4 Reduced Sherwood number Sh with $Pr = 0.71$, $Prm = 0.71$, $\beta = 0.1$, $Nb = Nt = 0.3$, $Rd = 1$

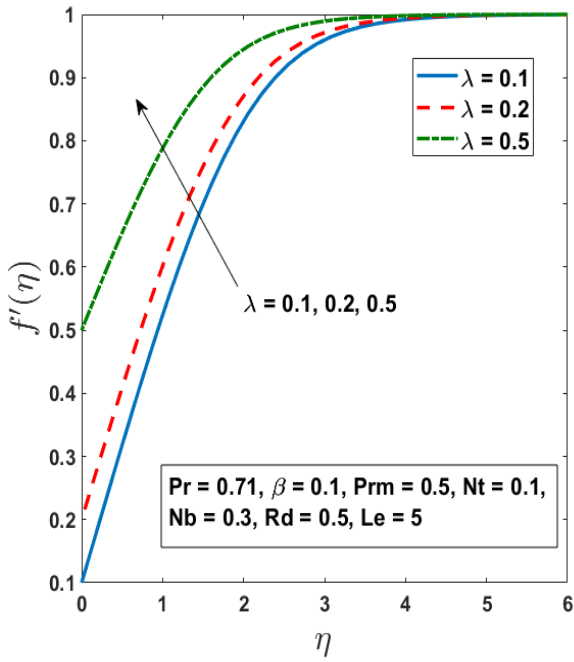
λ	$-\phi'(0), Le = 1$	$-\phi'(0), Le = 5$	$-\phi'(0), Le = 10$
-0.3	0.23757681	0.21076314	0.12930055
0.1	0.46154611	0.90775090	1.20149742
0.5	0.59332949	1.33118606	1.86506212
1	0.72134948	1.73296536	2.47937544
1.5	0.82831705	2.06229602	2.97641263
2	0.92225761	2.34770012	3.40422563

Table 3.5 Skin friction coefficient C_f with $Pr = 0.7$, $Prm = 0.5$, $\lambda = 0.1$, $Nt = 0.1$, $Nb = 0.3$, $Rd = 0.5$, and $Le = 5$

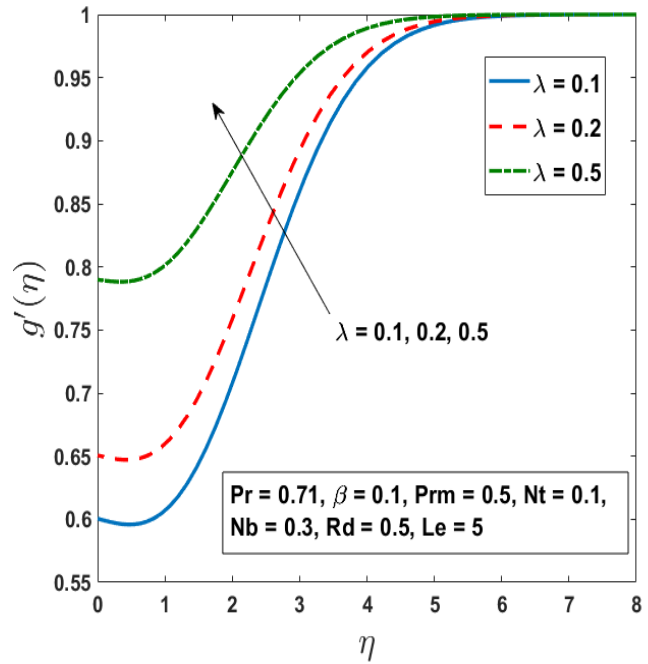
λ	$-f''(0)$ $\beta = 0.1$	$-f''(0)$ $\beta = 0.2$	$-f''(0)$ $\beta = 0.3$
0.1	0.46187385	0.46119457	0.46049300
0.2	0.44273586	0.44229701	0.44184741
0.3	0.41319222	0.41280996	0.41241846
0.4	0.37464177	0.37417205	0.37368768
0.5	0.32805632	0.32734220	0.32659778
0.6	0.27411112	0.27291390	0.00069248
0.7	0.21317965	0.21099046	0.00085186
0.8	0.14491586	0.00168838	0.00099312
0.9	0.00321266	0.00167927	0.00098807

Fig. 3.2 (a–d) displays the effects of the moving wall velocity parameter λ on the velocity, induced magnetic field, temperature, and nanoparticle concentration profiles. It is seen that increasing the velocity parameter λ leads to an increase in speed (Fig. 3.2 (a)), that is, the flow acceleration and induced magnetic field (Fig. 3.2 (b)) magnitudes. The hydrodynamic boundary-layer thickness decreases, whereas magnetic boundary-layer thickness grows. Asymptotically smooth profiles are achieved in the free stream, verifying that an adequately large infinity boundary condition is prescribed in the MATLAB SRM code. The temperature (Fig. 3.2 (c)) and nanoparticle concentration (Fig. 3.2 (d)) both decrease rapidly as the moving wall velocity parameter increases. The thermal boundary-layer and nanoparticle concentration boundary-layer thicknesses are reduced as λ increases.

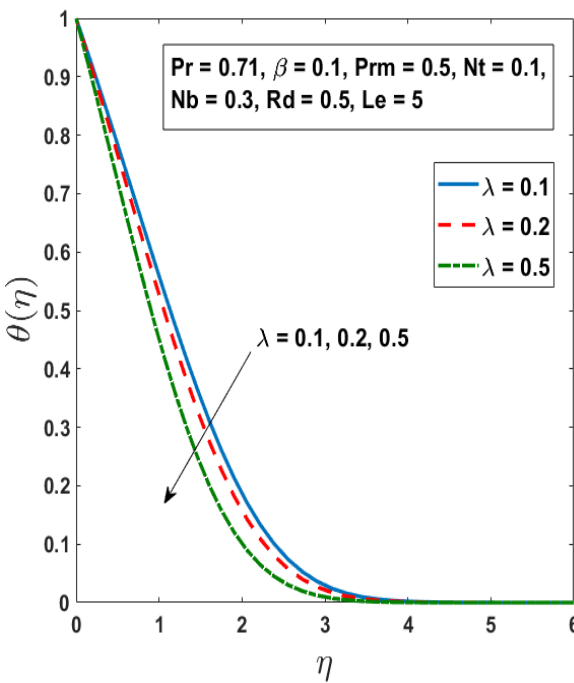
Fig. 3.3 (a–b) visualizes the effects of the magnetic force number β on the velocity and induced magnetic field profiles. This parameter features in the magnetic induction term in the dimensionless momentum boundary-layer equation (3.9), $-\beta g g''$, which also couples the momentum equation (3.9) to the magnetic induction equation (3.10). It is an opposing body force, and high values of β will inhibit momentum and magnetic induction in the regime.



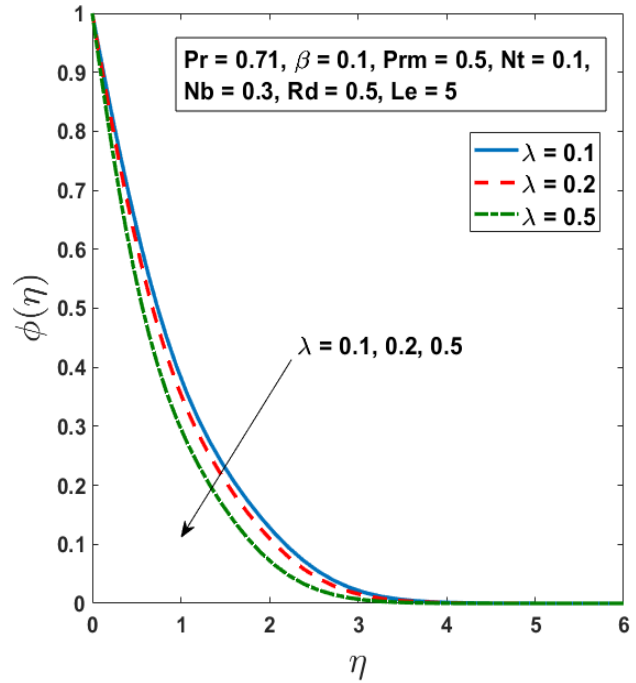
(a)



(b)



(c)



(d)

Fig. 3.2 The influence of λ on a) velocity profile, b) induced magnetic field profile, c) temperature profile, and d) concentration profile

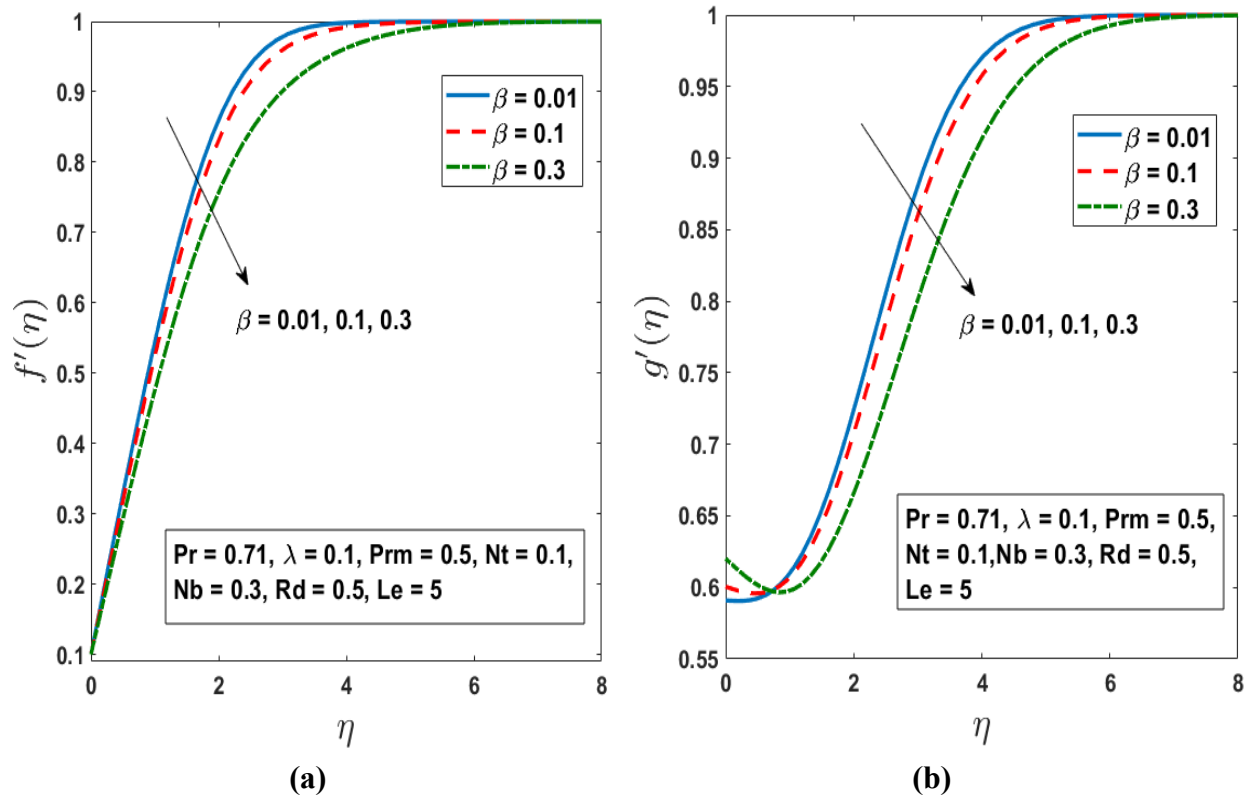


Fig. 3.3 The influence of magnetic force parameter, β on a) velocity profile and b) induced magnetic field profile

This will manifest as a decrease in velocity and induced magnetic field magnitudes and a concomitant increased momentum boundary-layer thickness and reduced magnetic boundary-layer thickness, as noted earlier by Hughes and Young (1966), among other researchers.

Fig. 3.4 (a–b) shows that increasing the Brownian motion parameter Nb noticeably decreases the temperature and nanoparticle concentrations. Conversely, in Fig. 3.5 (a–b), increasing the thermophoresis parameter Nt significantly elevates the temperature and concentration profiles. Thermophoretic body force encourages heat and nanoparticle mass diffusion with a thermal gradient. The thermal and nanoparticle concentration boundary-layer thicknesses, therefore, both grow with the thermophoretic body force. These trends concur with many other investigations, including those of Bachok *et al.* (2010), Ferdows *et al.* (2012), and Mabood *et al.* (2015), although these studies neglected magnetic induction effects. The nanoscale effects, that is, Brownian motion

and thermophoresis, do not significantly influence the nanofluid velocity or induced magnetic field profile. Therefore, these plots are omitted for brevity.

Fig. 3.6 (a–b) illustrates the variation of the temperature and nanoparticle concentration distributions in response to a change in Prandtl number Pr . Increasing Pr induces a substantial decrease in nanofluid temperature and reduces the thermal boundary-layer thickness. The nanoparticle concentration profiles exhibit a monotonic response to the Prandtl number: as Pr increases, nanoparticle diffusion is promoted, and the nanoparticle concentration boundary-layer thickness also increases.

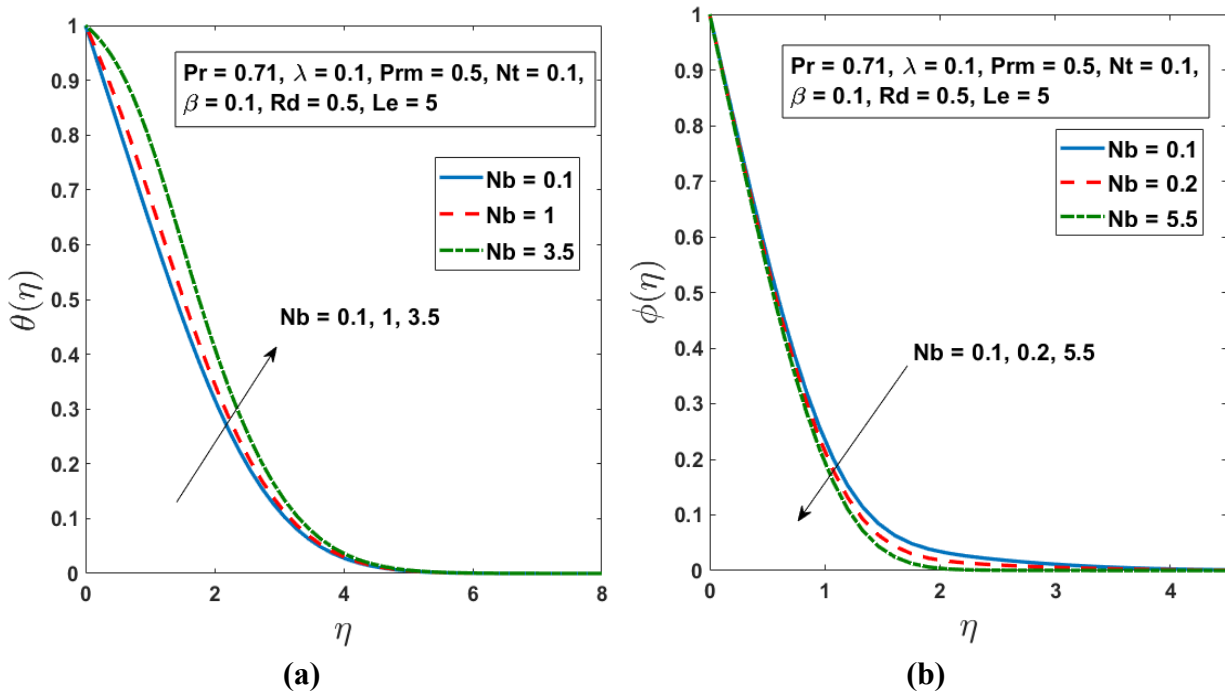


Fig. 3.4 The influence of Nb on a) temperature profile and b) concentration profile

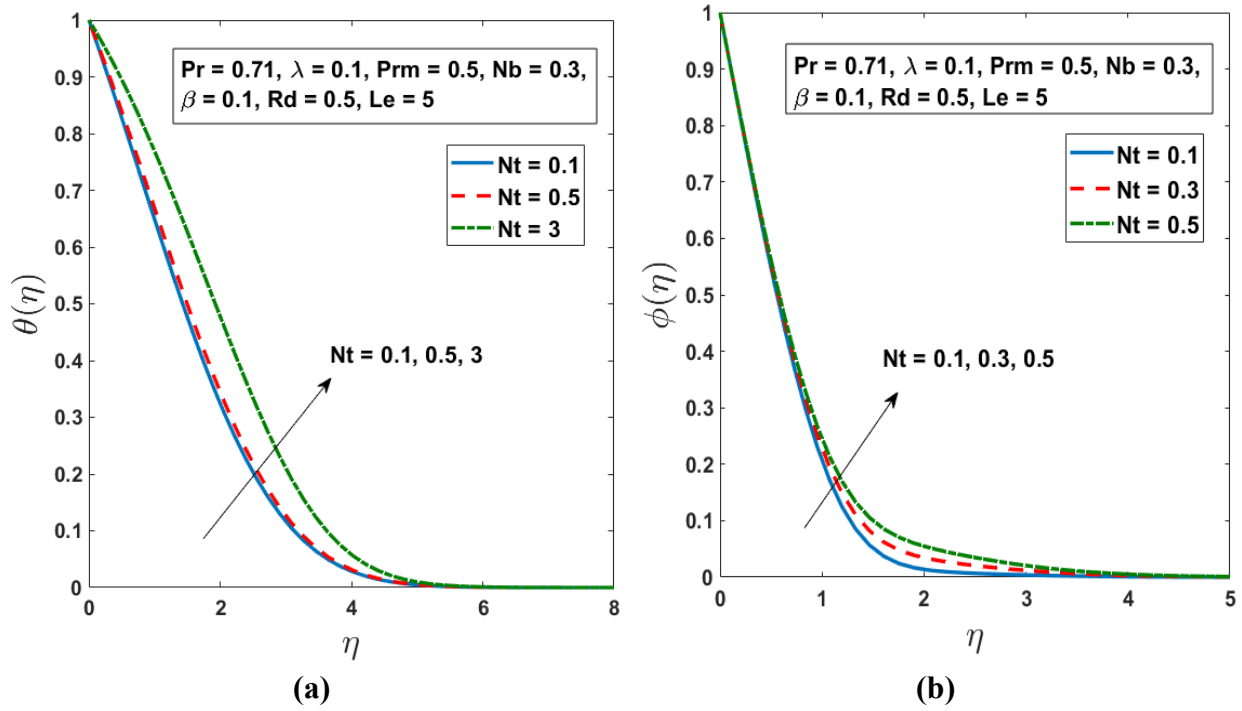


Fig. 3.5 The influence of Nt on a) temperature profile and b) concentration profile

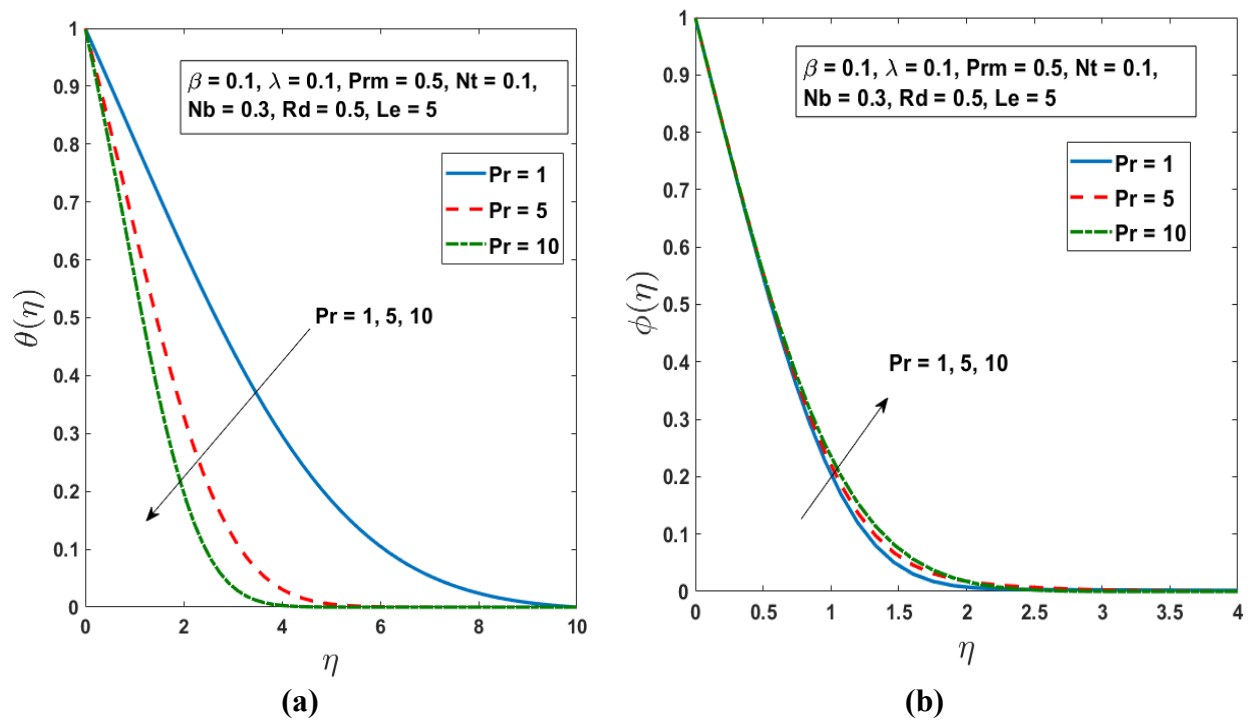


Fig. 3.6 The influence of Pr on a) temperature profile and b) concentration profile

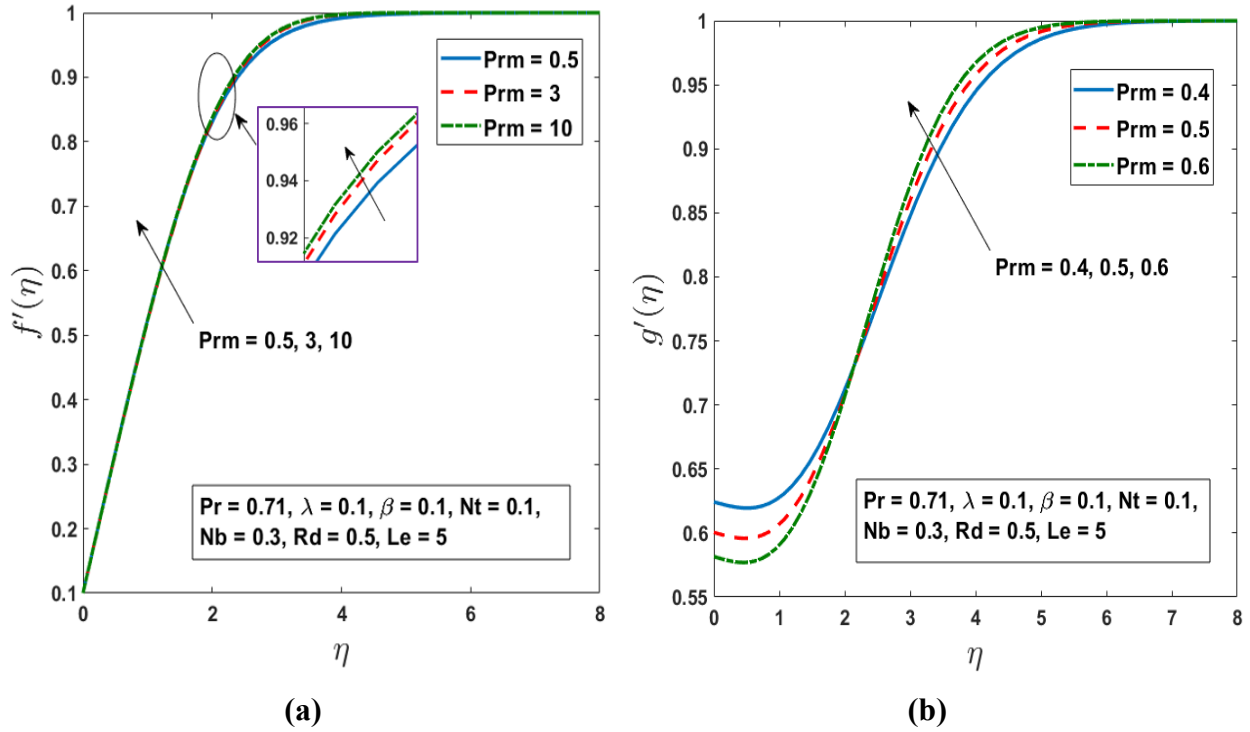


Fig. 3.7 The influence of Prm on a) temperature profile and b) concentration profile

Fig. 3.7 (a–b) visualizes the impact of the magnetic Prandtl number Prm on the velocity and induced magnetic field profiles. Both the velocity and induced magnetic field profiles of the nanofluid increase with Prm . This parameter is equal to ν/α_1 , is invoked because of magnetic induction effects, and determines the ratio of magnetic to viscous diffusivity. It features exclusively in the magnetic induction conservation equation (3.10). Thus, the magnetic Reynolds number is high enough for the flow field to cause magnetic field distortion. The magnetic field is considered to be undistorted by the flow for a case in which this parameter is much less than one. However, the induction effects of a large magnetic Reynolds number are significant and necessitate a separate conservation equation, as considered in the present model. As Prm is elevated, both momentum and magnetic induction are increased in the regime. The velocity and magnetic boundary-layer thicknesses will increase and decrease, respectively. It is also apparent that Prm has a greater effect on the magnetic induction $g'(\eta)$ than on $f'(\eta)$.

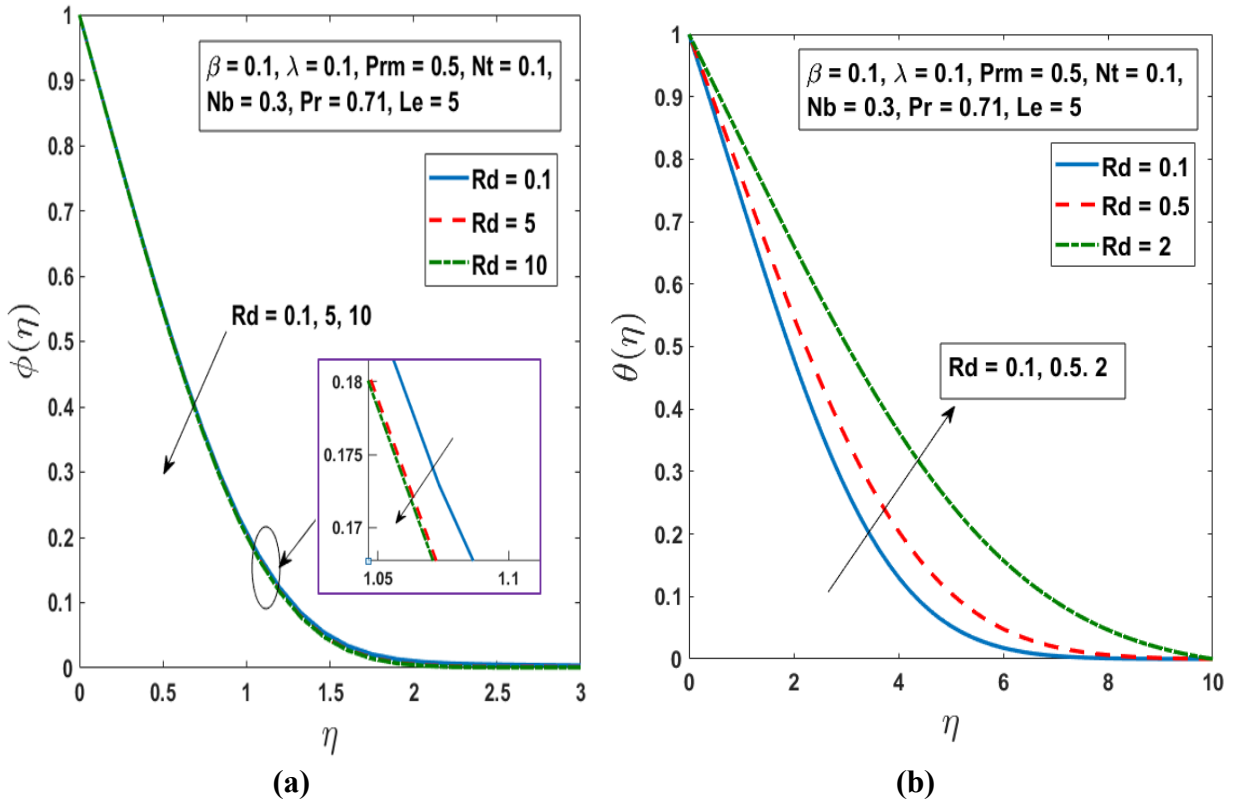


Fig. 3.8 The influence of Rd on a) temperature profile and b) concentration profile

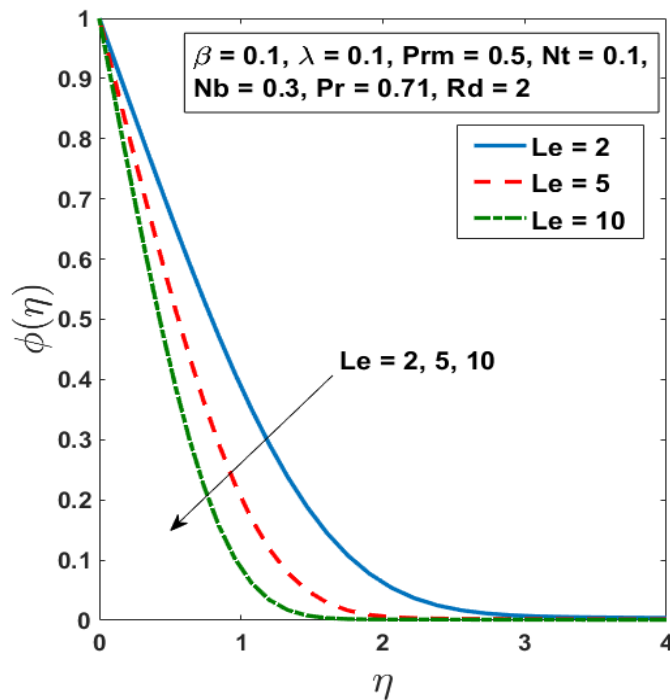


Fig. 3.9 The influence of Le on concentration profile

Fig. 3.8 (a–b) depicts the influence of the radiation parameter Rd on the nanoparticle volume fraction (concentration) and the temperature distribution, occurring in the augmented thermal diffusion term in the energy conservation equation (2.11), viz. $(1 + Rd)\theta''/Pr$. The quantity $R = 16\sigma T_\infty^3/3KK_s$ expresses the relative contribution of thermal radiation and thermal conduction to the heat transfer. When $Rd = 1$, both modes contribute equally. For $Rd < 1$, conduction dominates, and vice versa for $Rd > 1$. An increase in Rd leads to a decrease in the nanoparticle volume fraction (Fig. 3.8 (a)) since greater energization of the nanofluid with radiative flux inhibits nanoparticle diffusion; however, the opposite response is induced on temperature magnitudes (Fig. 3.8 (b)), which are strongly elevated with a greater radiative contribution. The nanoparticle concentration boundary-layer thickness is decreased, whereas the thermal boundary-layer thickness is increased, with greater radiative parameter (this agrees with the decrease in reduced Nusselt number at the wall, discussed earlier). The computations agree with several other investigations, including those of Aly and Sayed (2017) and Uddin *et al.* (2015). Therefore, the inclusion of radiative heat transfer in magnetic nanomaterials fabrication produces more accurate temperature and nanoparticle concentration predictions than neglecting this mode of heat transfer (which leads to underpredicting temperatures and overpredicting nanoparticle volume fractions).

Fig. 3.9 illustrates the variation of the nanoparticle concentration profile with the Lewis number $= \nu/D_B$, which defines the ratio of the momentum diffusion rate to the nanoparticle species diffusion rate. When $Le = 1$, these rates are equal, and the momentum and nanoparticle concentration boundary-layer thicknesses are similar. However, for $Le > 1$ (as considered here), the momentum diffusivity exceeds the species diffusivity, which inhibits nanoparticle diffusion and results in a reduction in nanoparticle concentration boundary-layer thickness. The latter may, therefore, be successfully controlled in nanoliquid material processing via careful selection of nanoparticles based on appropriate diffusivities.

Figs. 3.10–3.12 show plots of the skin friction coefficient C_f , the reduced Nusselt number Nu , and the reduced Sherwood number Sh against the velocity parameter, for different values of the magnetic parameter, Prandtl number, and Lewis number, respectively. The values of the skin friction coefficient C_f decrease as the magnetic force parameter increases, and the reduced Nusselt number Nu grows rapidly with the Prandtl number. The reduced Sherwood number Sh increases with the Lewis number.

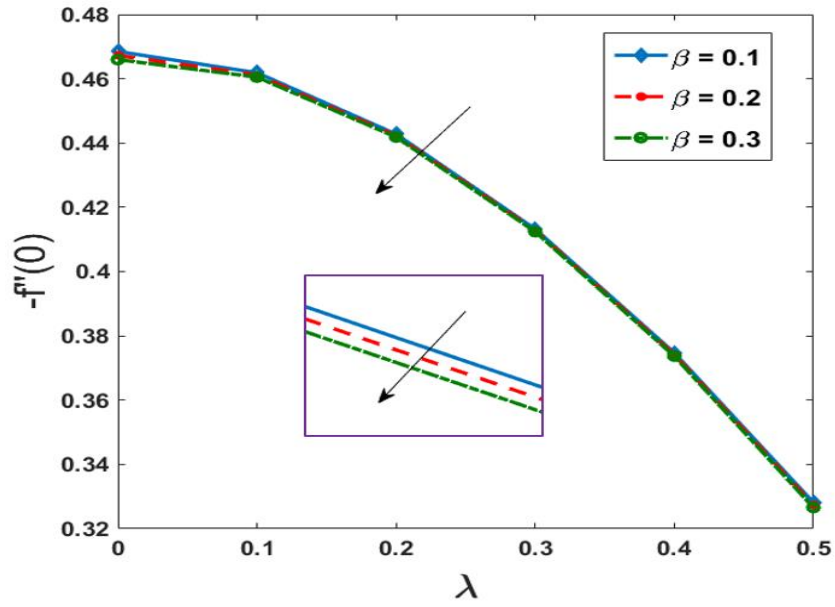


Fig. 3.10 Influence of β and λ on the skin friction coefficient C_f

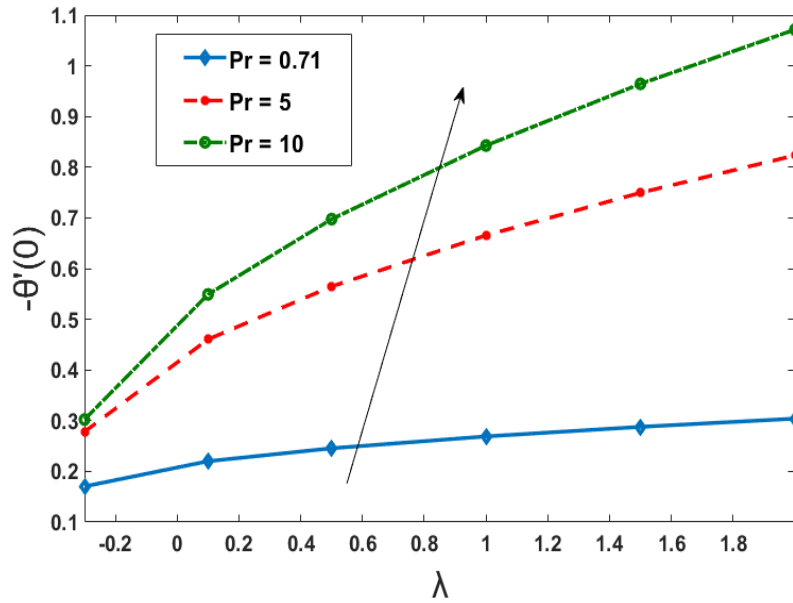


Fig. 3.11 Influence of Pr and λ on reduced Nusselt number Nu

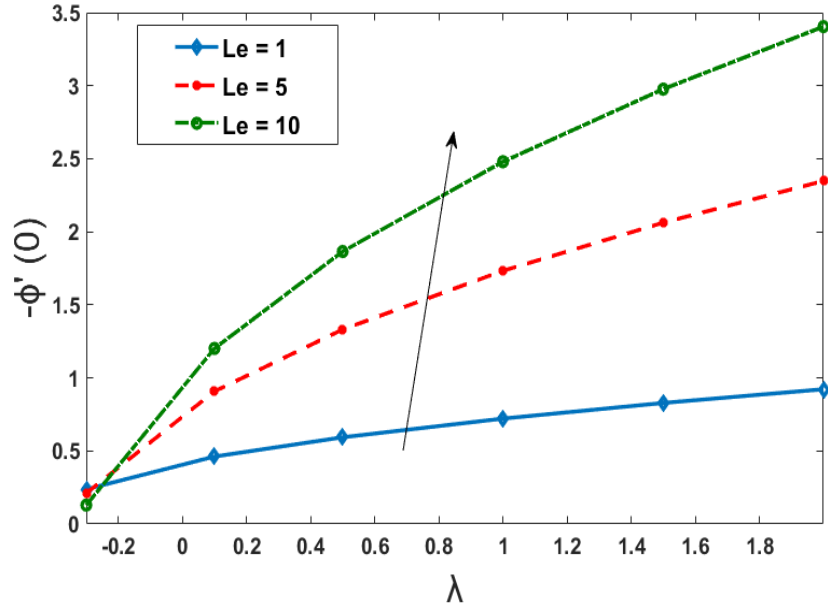


Fig. 3.12 Influence of Le and λ on reduced Sherwood number Sh

3.5 Summary

In this chapter, the steady thermal-convection boundary-layer flow of electroconductive nanofluids over a moving surface with magnetic induction and radiative heat transfer effects has been studied. The Buongiorno model has been deployed, incorporating the results of Brownian diffusion and thermophoresis. The variation of the skin friction coefficient, the heat transfer rate, and the mass transfer rate, as well as the velocity, induced magnetic field, temperature, and nanoparticle volume fraction profiles, has been illustrated in tabular and graphical form for various values of the physical parameters. The MATLAB SRM code has been validated against published results.

Chapter 4

Spectral Relaxation Method for Convective Metallic Nanofluid Flow with an Induced Magnetic Field past an Inclined Stationary or Moving Flat Plate

This chapter describes a mathematical model for incompressible free convection flows with convective heat transport from an inclined stationary/moving flat plate under the impact of an induced magnetic field. The current flow model is formulated considering the heat transport in the nanofluid external boundary layer from an inclined stationary/moving flat plate with a range of metallic nanoparticles in water as the base fluid. A nanoscale formulation with the Tiwari–Das model is effectively deployed to study material properties for specific nanoparticles and base fluid. The nonlinear model is rendered into a system of coupled ODEs with suitable far-stream and convective wall boundary conditions by developing appropriate transformation similarity variables. The effects of embedded parameters, like the Grashof number Gr , Biot number Bi , angle of inclination α , magnetic field parameter M , and magnetic Prandtl number Pr_m , on the velocity, induced magnetic field, temperature, nanoparticle concentration, skin friction, and local Nusselt number profiles, are visualized. The results are verified for limiting cases by comparing them with various studies for the case of stationary and moving flat plates, and are found to be in excellent agreement. Furthermore, computed numerical results for skin friction and Nusselt number, for different emerging parameters in Cu and Ag nanofluids with a moving plate, are tabulated and discussed in detail.

4.1 Mathematical Modelling

The steady two-dimensional boundary-layer flow of a stream of cold, incompressible, viscous, electrically conducting nanofluid of temperature T_∞ , passing through a moving flat plate with constant velocity U_w , in the same or opposite direction to the free stream U_∞ , is considered. The plate is inclined with an acute angle α with the vertical. The x –axis is measured along the plate, and the y –axis is measured in the direction normal to the plate, as shown in Fig. 4.1. An induced magnetic field of strength H_0 is applied orthogonal to the plate; H_1 and H_2 are the parallel and

normal components of the induced magnetic field; in the free stream, H_1 becomes H_0 while H_2 vanishes near the wall. It is also assumed that the lower surface of the plate is heated by convection from a hot fluid of temperature T_f , which provides a heat transfer coefficient of h_f .

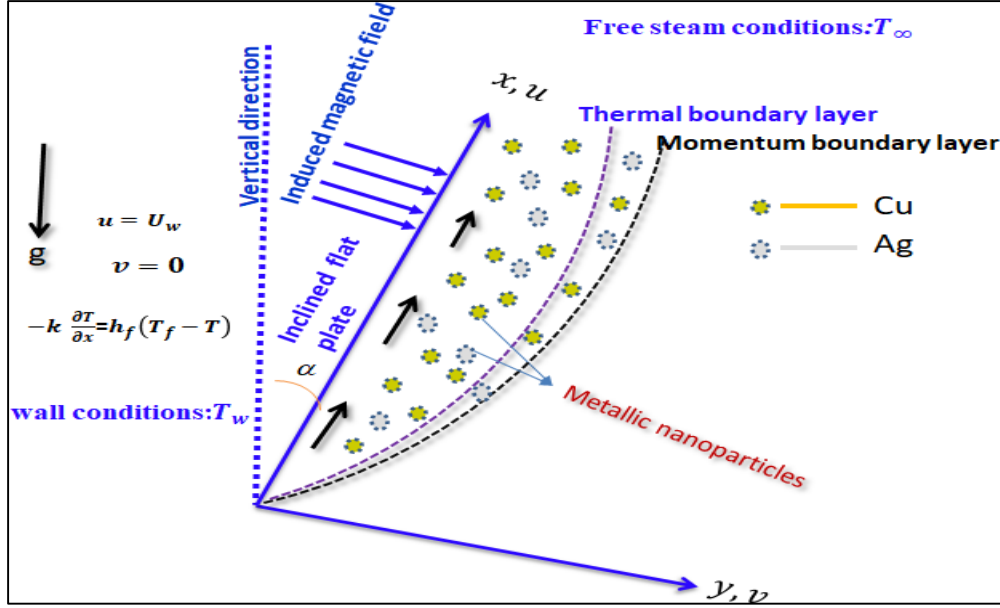


Fig. 4.1 Physical model of the problem

Under these assumptions, following the nanofluid model proposed by Tiwari and Das (2007), the governing mass, momentum, induced magnetic field, and energy equation are described as follows:

Continuity:

$$\frac{\partial u}{\partial x} + \frac{\partial v}{\partial y} = 0 \quad (4.1a)$$

$$\frac{\partial H_1}{\partial x} + \frac{\partial H_2}{\partial y} = 0 \quad (4.1b)$$

Momentum:

(4.2)

$$u \frac{\partial u}{\partial x} + v \frac{\partial u}{\partial y} = \frac{\mu_0}{\rho_{nf}} \left(H_1 \frac{\partial H_1}{\partial x} + H_2 \frac{\partial H_1}{\partial y} \right) + \frac{\mu_{nf}}{\rho_{nf}} \frac{\partial^2 u}{\partial y^2} + \frac{g(\rho\beta)_{nf}}{\rho_{nf}} (T - T_\infty) \cos \alpha$$

Induced magnetic field: (4.3)

$$u \frac{\partial H_1}{\partial x} + v \frac{\partial H_1}{\partial y} - H_1 \frac{\partial u}{\partial x} - H_2 \frac{\partial u}{\partial y} = \alpha_1 \frac{\partial^2 H_1}{\partial y^2}$$

Energy: (4.4)

$$u \frac{\partial T}{\partial x} + v \frac{\partial T}{\partial y} = \frac{k_{nf}}{(\rho C_p)_{nf}} \frac{\partial^2 T}{\partial y^2}$$

where α is the angle of inclination and $\alpha_1 = 1/4\pi\sigma_{nf}$ is the magnetic diffusivity of the nanofluid. The appropriate boundary conditions (Ramesh, 2016) for the current study are described by

$$\left. \begin{aligned} u = U_w, v = 0, \frac{\partial H_1}{\partial y} = H_2 = 0, -k_f \frac{\partial T}{\partial y} = h_f(T_f - T) \quad \text{at } y = 0 \\ u \rightarrow U_\infty, H_1 \rightarrow H_0, T \rightarrow T_\infty \quad \text{at } y \rightarrow \infty \end{aligned} \right\} \quad (4.5)$$

For a similarity solution of momentum and energy equations, let $h_f = c/\sqrt{x}$, where c is a constant.

4.2 Thermophysical Properties of Nanofluids

The fluid is water-based and contains two different types of nanoparticles, namely copper (*Cu*) and silver (*Ag*). It is assumed that both the base fluid and the nanoparticles are in thermal equilibrium without a slip condition between them. Following Sheikholeslami (2015) and Bég (2018), the thermophysical properties of the base fluid and nanoparticles are given in Table 4.1. The mathematical relations for the thermophysical properties of nanofluids are listed in Table 4.2. The nanoparticle volume fraction parameters related to the study of nanofluid are listed in Table 4.3.

Table 4.1 Thermophysical properties of the base fluid and nanoparticles

Physical property	Base fluid (water)	Copper (Cu)	Silver (Ag)
C_p (J/kg · K)	4,179	385	235
ρ (kg/m ³)	997.1	8,933	10,500
k (W/m · K)	0.613	401	429
σ (S/m)	0.05	5.96×10^7	3.6×10^7
$\beta \times 10^{-5}$ (1/K)	21	1.67	1.89

Table 4.2 Mathematical relations of thermophysical properties of nanofluid

Property	Nanofluid
Kinematic viscosity	$\nu_{nf} = \frac{\mu_{nf}}{\rho_{nf}}$
Viscosity	$\mu_{nf} = \frac{\mu_f}{(1 - \phi)^{2.5}}$
Density	$\rho_{nf} = (1 - \phi)\rho_f + \phi\rho_s$
Thermal diffusivity	$(\rho\beta)_{nf} = (1 - \phi)(\rho\beta)_f + \phi(\rho\beta)_s$
Heat capacity	$(\rho C_p)_{nf} = (1 - \phi)(\rho C_p)_f + \phi(\rho C_p)_s$
Electrical conductivity	$\frac{\sigma_{nf}}{\sigma_f} = 1 + \frac{3((\sigma_s/\sigma_f) - 1)\phi}{((\sigma_s/\sigma_f) + 2) - \phi((\sigma_s/\sigma_f) - 1)}$
Thermal conductivity	$\frac{k_{nf}}{k_f} = \frac{1 - \phi + 2\phi \frac{k_s}{k_s - k_f} \ln \frac{k_s + k_f}{2k_f}}{1 - \phi + 2\phi \frac{k_f}{k_s - k_f} \ln \frac{k_s + k_f}{2k_f}}$

Table 4.3 Nanoparticle volume fraction parameters

$$\begin{aligned}\phi_1 &= (1 - \phi)^{2.5} \left(1 - \phi + \phi \frac{\rho_s}{\rho_f}\right) \\ \phi_2 &= 1 - \phi + \phi \frac{\rho_s}{\rho_f} \\ \phi_3 &= 1 - \phi + \phi \frac{(\rho\beta)_s}{(\rho\beta)_f} \\ \phi_4 &= \frac{\sigma_{nf}}{\sigma_f} = 1 + \frac{3((\sigma_s/\sigma_f) - 1)\phi}{((\sigma_s/\sigma_f) + 2) - \phi((\sigma_s/\sigma_f) - 1)} \\ \phi_5 &= \frac{k_{nf}}{k_f} = \frac{1 - \phi + 2\phi \frac{k_s}{k_s - k_f} \ln \frac{k_s + k_f}{2k_f}}{1 - \phi + 2\phi \frac{k_f}{k_s - k_f} \ln \frac{k_s + k_f}{2k_f}} \\ \phi_6 &= 1 - \phi + \phi \frac{(\rho C_p)_s}{(\rho C_p)_f}\end{aligned}$$

Let us introduce the following non-dimensional variables to simplify the mathematical analysis:

$$\psi = (2Uvx)^{\frac{1}{2}} f(\eta), \quad \Phi = \left(\frac{2vx}{U}\right)^{\frac{1}{2}} H_0 g(\eta), \quad \theta(\eta) = \frac{T - T_\infty}{T_w - T_\infty}, \quad \eta = \left(\frac{U}{2vx}\right)^{\frac{1}{2}} y \quad (4.6)$$

Here, $\psi(x, y)$ and $\Phi(x, y)$ are the stream functions defined by

$$\left. \begin{aligned} u &= \frac{\partial \psi}{\partial y}, \quad v = -\frac{\partial \psi}{\partial x} \\ H_1 &= \frac{\partial \Phi}{\partial y}, \quad H_2 = -\frac{\partial \Phi}{\partial x} \end{aligned} \right\} \quad (4.7)$$

The continuity equations (4.1a) and (4.1b) are identically satisfied with the above transformations. Modifying the governing equations (4.2)–(4.4) by using (4.6) and (4.7), along with the boundary conditions (4.5), reduces them to the following non-dimensional form:

$$\frac{2}{\phi_1} f''' + ff'' - \frac{M}{\phi_2} gg'' + 2Gr \cos \alpha \frac{\phi_3}{\phi_2} \theta = 0 \quad (4.8)$$

$$2g''' + Pr_m \phi_4 f g'' - Pr_m \phi_4 g f'' = 0 \quad (4.9)$$

$$\frac{2\phi_5}{Pr\phi_6}\theta'' + f\theta' = 0 \quad (4.10)$$

The corresponding dimensionless parameters appearing in equations (4.8)–(4.10) are the magnetic interaction parameter, the local Grashof number (Kierkus, 2008), the magnetic Prandtl number, and the Prandtl number, which are defined as follows:

$$M = \frac{\mu_0 H_0^2}{\rho_f U^2}, \quad Gr = \frac{g \beta_f (T_f - T_\infty) x}{U^2}, \quad Prm = \frac{\alpha_1}{\nu_f}, \quad Pr = \frac{\nu_f (\rho C_p)_f}{k_f} \quad (4.11)$$

It is observed from equation (4.8) that when $\alpha = 0^\circ$, the problem reduces to the vertical flat plate, whereas $\alpha = 90^\circ$ reduces it to the horizontal flat plate. In the above, $\phi_1, \phi_2, \phi_3, \phi_4, \phi_5$, and ϕ_6 are the nanofluid volume fraction parameters listed in Table 4.3.

The boundary conditions given in (4.5) can be described as:

$$\left. \begin{aligned} f(0) = 0, \quad f'(0) = \lambda, \quad g(0) = g''(0) = 0, \quad \theta'(0) = -Bi(1 - \theta) \text{ as } \eta = 0 \\ f' \rightarrow 1 - \lambda, \quad g' \rightarrow 1, \quad \theta \rightarrow 0 \text{ as } \eta \rightarrow \infty \end{aligned} \right\} \quad (4.12)$$

where $\lambda = U_w/U$ is the velocity ratio parameter, and $Bi = (c/k_f)\sqrt{\nu_f/U}$ is the Biot number. The problem reduces to the Blasius flow (stationary flat plate) for $\lambda = 0$ and Sakiadis flow (moving flat plate) for $\lambda = 1$.

In the present study, the most important quantities of physical interest are the skin friction coefficient C_f and the heat transfer coefficient Nu_x , which are defined as

$$C_f = \frac{2\tau_w}{\rho_f U^2} \quad \text{and} \quad Nu_x = \frac{xq_w}{k_f(T_w - T_\infty)} \quad (4.13)$$

where τ_w and q_w are the wall shear stress and wall heat flux, respectively, defined as

$$\tau_w = \mu_{nf} \left(\frac{\partial u}{\partial y} \right)_{y=0} \quad \text{and} \quad q_w = -k_{nf} \left(\frac{\partial T}{\partial y} \right)_{y=0} \quad (4.14)$$

Using equation (4.14) in (4.13), we obtain

$$\frac{1}{2} \sqrt{Re_x} C_f = \frac{1}{(1 - \phi)^{2.5}} f''(0) \quad (4.15)$$

$$(Re_x)^{-1/2}Nu_x = -\phi_5\theta'(0) \quad (4.16)$$

where $Re_x = Ux/v_f$ is the local Reynolds number.

The spectral relaxation method (SRM) is employed here to solve the ODEs (4.9)–(4.11) together with the boundary conditions (4.12). We derive the following iteration scheme within the framework of the SRM algorithm,

$$\frac{2}{\phi_1}F''_{r+1} + f_r F'_{r+1} - \frac{M}{\phi_2}g_r G'_r + 2Gr \cos \alpha \frac{\phi_3}{\phi_2} \theta_r = 0 \quad (4.17)$$

$$2G''_{r+1} + Prm\phi_4 f_{r+1} G'_{r+1} - Prm\phi_4 g_r F'_{r+1} = 0 \quad (4.18)$$

$$\frac{2\phi_5}{Pr\phi_6} \theta''_{r+1} + f_{r+1} \theta'_{r+1} = 0 \quad (4.19)$$

subject to the following boundary conditions:

$$F_{r+1}(0) = \lambda, \quad F_{r+1}(\infty) = 1 - \lambda \quad (4.20)$$

$$f_{r+1}(0) = 0 \quad (4.21)$$

$$G'_{r+1}(0) = 0, \quad G'_{r+1}(\infty) = 1 \quad (4.22)$$

$$g_{r+1}(0) = 0 \quad (4.23)$$

$$\theta'_{r+1}(0) = -Bi(1 - \theta_{r+1}(0)), \quad \theta_{r+1}(\infty) = 0 \quad (4.24)$$

The above equations form a system of linear decoupled equations that can be solved iteratively for $r = 1, 2, \dots$ starting from initial approximations $F_0(\eta)$, $G_0(\eta)$, and $\theta_0(\eta)$.

By using the Chebyshev pseudo-spectral approach on equations (4.17) to (4.24), the following results are obtained:

$$A_1 \mathbf{F}_{r+1} = R_1, \quad F_{r+1}(\tau_N) = 1 - \lambda, F_{r+1}(\tau_0) = \lambda \quad (4.25)$$

$$A_2 \mathbf{f}_{r+1} = R_2, \quad f_{r+1}(\tau_N) = 0 \quad (4.26)$$

$$A_3 \mathbf{G}_{r+1} = R_3, \quad G'_{r+1}(\tau_N) = 0, G_{r+1}(\tau_0) = 1 \quad (4.27)$$

$$A_4 \mathbf{g}_{r+1} = R_4, \quad g_{r+1}(\tau_N) = 0 \quad (4.28)$$

$$A_5 \boldsymbol{\theta}_{r+1} = R_5, \quad \theta_{r+1}(\tau_N) = 0, \theta'_{r+1}(\tau_0) = -Bi(1 - \theta_{r+1}(\tau_0)) \quad (4.29)$$

where

$$A_1 = \text{diag}\left(\frac{2}{\phi_1}\right) D^2 + \text{diag}(f_r) D, \quad R_1 = \frac{M}{\phi_2} g_r G'_r + 2Gr \cos \alpha \frac{\phi_3}{\phi_2} \theta_r \quad (4.30)$$

$$A_2 = D, \quad R_2 = F_{r+1} \quad (4.31)$$

$$A_3 = 2D^2 + \text{diag}(Prm\phi_4 f_{r+1}) D, \quad R_3 = Prm\phi_4 g_r F'_{r+1} \quad (4.32)$$

$$A_4 = D, \quad R_4 = G_{r+1} \quad (4.33)$$

$$A_5 = \text{diag}\left(\frac{2\phi_5}{Pr\phi_6}\right) D^2 + \text{diag}(f_{r+1}) D, \quad R_5 = 0 \quad (4.34)$$

The spectral collocation method can be used to solve equations (4.25) to (4.34), which make up the SRM scheme. The initial conditions listed below are selected to meet the boundary conditions:

$$f_0(\eta) = \eta + e^{-\eta} - e^{-\lambda\eta}, \quad g_o(\eta) = \eta - (2 + \eta)e^{-\eta} + 2, \quad \theta_0(\eta) = \frac{1}{2}e^{-Bi\eta} \quad (2.35)$$

4.3 Numerical Results and Discussion

A broad range of spectral relaxation method (SRM) computations have been performed to investigate the effects of nanoscale, thermophysical, and hydrodynamic parameters on the non-dimensional velocity, induced magnetic field, temperature, skin friction, and Nusselt number. The results are visualized in Figs. 4.2–4.17. The infinity value η_∞ is chosen to be 15, and the SRM findings are achieved with $N = 60$ collocation points. To justify the numerical results obtained, a comparison has been made with the values of $-\theta'(0)$ at $\lambda = 0$ with the published results of Aziz (2009) in Table 4.4 for $Pr = 0.72$ and $Pr = 10$, and in Table 4.5 with those of Ramesh (2016) for both a flat plate ($\lambda = 0$) and a moving plate ($\lambda = 1$) at different values of Biot number. Excellent agreement has been found. Extensive calculations have been performed to obtain the velocity, induced magnetic field, temperature profiles, skin friction coefficient, and local Nusselt number for various values of physical parameters such as ϕ , α , Gr , Prm , and Bi .

Table 4.4 Comparison of the SRM $-\theta'(0)$ results with Aziz (2009) for different values of Biot number when $\alpha = \pi/2$, $\phi = 0$, $Gr = 0$, $M = 0$, $Prm = 0$, and $\lambda = 0$

Bi	Present SRM		Aziz (2009)	
	$Pr = 0.72$	$Pr = 0.72$	$Pr = 10$	$Pr = 10$
0.05	0.04301040	0.04684338	0.0468	0.0468
0.10	0.07514188	0.08800435	0.0879	0.0879
0.20	0.11993571	0.15699452	0.1569	0.1569
0.40	0.17091211	0.25833066	0.2582	0.2582
0.60	0.19912003	0.32914211	0.3289	0.3289
0.80	0.21704351	0.38137649	0.3812	0.3812
1	0.22940863	0.42159040	0.4213	0.4213
5	0.28062282	0.63591888	0.6356	0.6356
10	0.28870770	0.67904684	0.6787	0.6787
20	0.29289876	0.70294207	0.7026	0.7026

The numerical values of the skin friction coefficient C_f and the reduced Nusselt number Nu for various values of the volume fraction ϕ , magnetic field M , angle of inclination α , and magnetic Prandtl number Prm , with fixed values of the Grashof number Gr and Biot number Bi , are shown in Table 4.6 for Cu -water and Ag -water nanofluids and a moving plate ($\lambda = 1$). The impact of increasing ϕ and α is to increase the skin friction coefficient C_f while decreasing the reduced Nusselt number Nu for both the Cu -water and Ag -water nanofluids. Growing magnetic field M and Biot number Bi values reduce the skin friction coefficient, but enhance the non-dimensional rate of heat transfer for both the Cu -water and Ag -water nanofluids when the direction of the free stream is fixed ($\lambda = 1$). It is also observed that the Cu -water nanofluid has a lower skin friction coefficient and a higher reduced Nusselt number than the Ag -water nanofluid.

Table 4.5 Comparison of the SRM $-\theta'(0)$ results with Ramesh (2016) for different values of Bi when $\alpha = \pi/6$, $Gr = 0.5$, $\phi = 0$, $M = 0$, and $Prm = 0$, for $\lambda = 0$ and $\lambda = 1$

Bi	Present SRM		Ramesh (2016)	
	$\lambda = 0$	$\lambda = 1$	$\lambda = 0$	$\lambda = 1$
0.1	0.07599846	0.0759	0.0759	0.07599846
0.5	0.20217874	0.2021	0.2021	0.20217874
2.0	0.29983621	0.2997	0.2997	0.29983621
5.0	0.33295986	0.3328	0.3328	0.33295986
10	0.34578606	0.3456	0.3456	0.34578606
50	0.35678464	0.3567	0.3567	0.35678464
100	0.35819841	0.3581	0.3581	0.35819841
500	0.35933003	0.3593	0.3593	0.35933003
1000	0.35941088	0.3594	0.3594	0.35941088
5000	0.35953216	0.3595	0.3595	0.35953216
10000	0.35957663	0.3595	0.3595	0.35957663
100000	0.35958067	0.3595	0.3595	0.35958067
1000000	0.35958472	0.3595	0.3595	0.35958472
5000000	0.35958876	0.3595	0.3595	0.35958876

Table 4.6 Numerical data for $f''(0)$ and $-\theta'(0)$ for Cu -water and Ag -water nanofluids with $\phi = 0.2$, $Gr = 0.5$, $Pr = 6.2$, $Bi = 1$, and $\lambda = 1$

ϕ	M	α	Prm	Cu -water ($\lambda = 1$)		Ag -water ($\lambda = 1$)	
				$f''(0)$	$-\theta'(0)$	$f''(0)$	$-\theta'(0)$
0.05	0.01	45°	0.1	-0.41545475	1.07155641	-0.42858764	1.05392909
0.1				-0.52568297	0.95286723	-0.54954923	0.92345929
0.2				-0.77040321	0.84552535	-0.81299751	0.79909409
0.2	0.01	45°	0.1	-0.77040321	0.84552535	-0.81299751	0.79909409
	0.02			-0.76977043	0.84575730	-0.81238217	0.79932789
	0.1			-0.76477838	0.84757755	-0.80752212	0.80116472
0.2	0.01	30°	0.1	-0.73280627	0.84716475	-0.77295072	0.80129091
		45°		-0.77058266	0.84462326	-0.81318129	0.79827185
		60°		-0.82210282	0.83156288	-0.86807820	0.78537822
0.2	0.01	45°	0.05	-0.77074870	0.84539911	-0.81299751	0.79991601
			0.1	-0.77040321	0.84552535	-0.81080856	0.79909409
			0.5	-0.76549070	0.84725537	-0.76359696	0.81629551

Fig. 4.2 (a–b) presents the evolution of the linear velocity, induced magnetic field, and temperature profiles with various nanoparticle volume fractions (ϕ) for Cu -water and Ag -water nanofluids for both a stationary flat plate ($\lambda = 0$) and a moving flat plate ($\lambda = 1$). Fig. 4.2 (a–b) shows the response of the transverse velocity to a modification in nanoparticle volume fraction, for Cu and Ag nanoparticles and for a moving flat plate and a stationary plate. It is evident in the case of a moving flat plate that the flow is reduced substantially with a higher fractional volume of nanoparticles, and the thickness of the hydrodynamic boundary layer reduces; it is evident for the

case of a stationary plate that a strong increase in the flow is induced by a higher fractional volume of nanoparticles. The *Cu* nanofluid produces the maximum velocity while *Ag* achieves the least. It is apparent from Fig. 4.3 (a–b) that a strong increase in the case of a moving plate and a strong decrease in the case of a stationary plate is obtained with a higher nanoparticle volume fraction. In Fig. 4.4 (a–b) an increase in nanoparticle volume fraction is observed to substantially elevate temperatures throughout the boundary-layer regime, irrespective of whether the plate is moving and stationary and the nanoparticle considered.

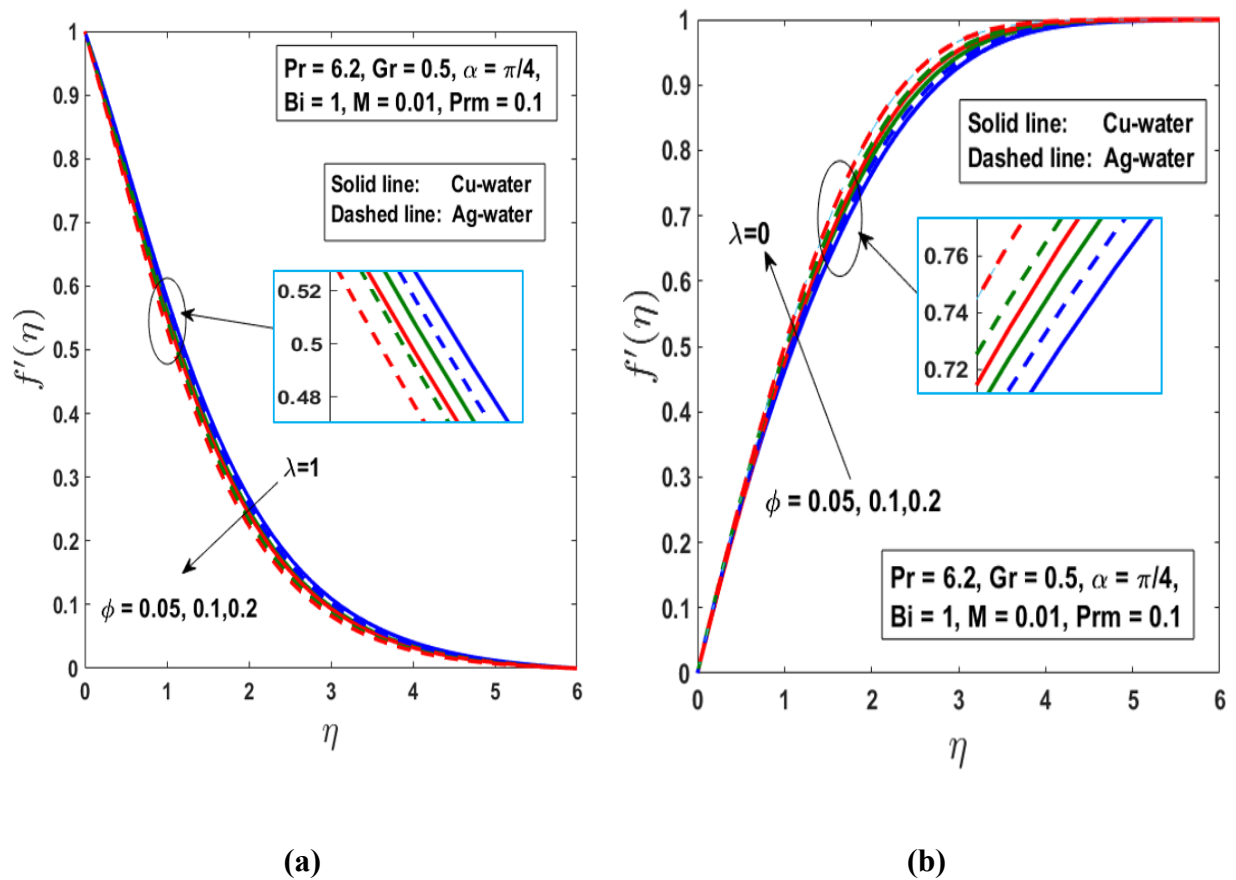


Fig. 4.2 Effect of nanoparticle value fraction ϕ on velocity for (a) $\lambda = 1$ and (b) $\lambda = 0$

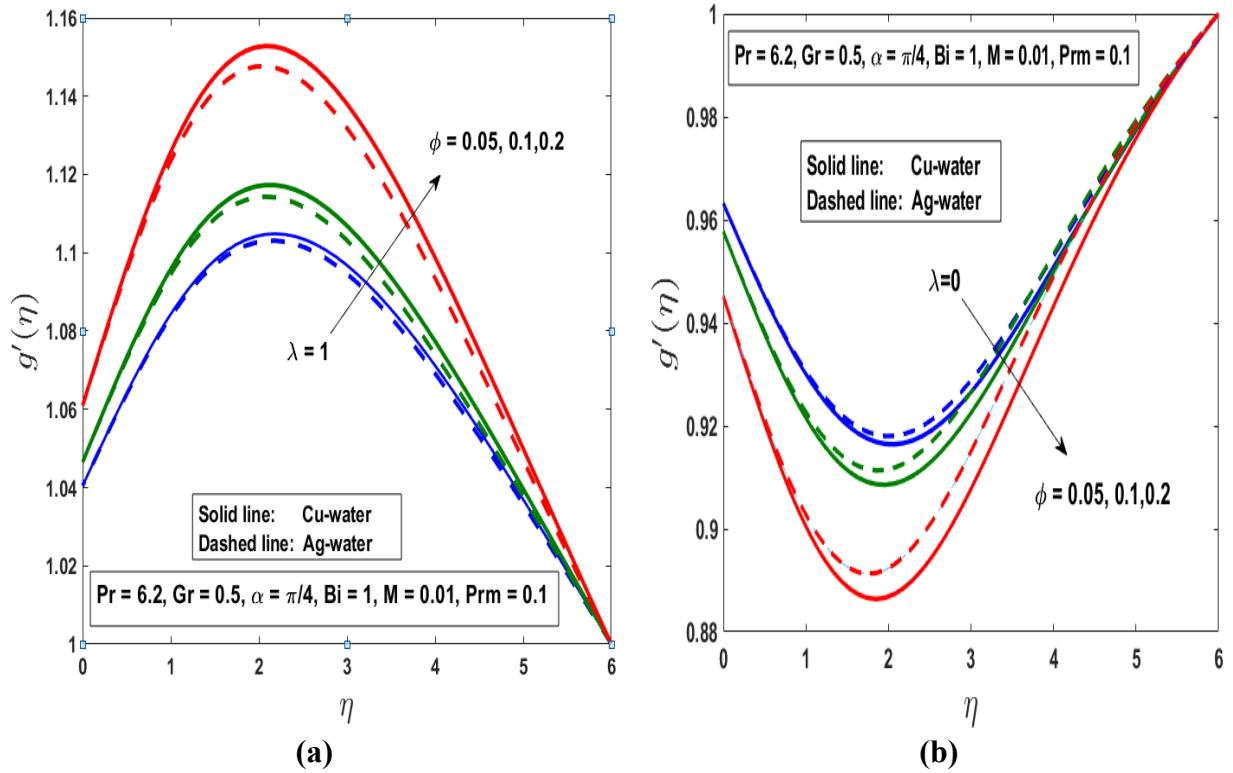


Fig. 4.3 Effect of nanoparticle value fraction ϕ on induced magnetic field for (a) $\lambda = 1$ and (b) $\lambda = 0$

Therefore, the thickness of the thermal boundary layer increases. The flow distributions indeed confirm the non-trivial effect of nanoparticle doping as a robust mechanism for elevating both convection and conduction coefficients. Hence, the use of nanofluids is an effective method for energizing base fluids without the clogging effects encountered with micro-scaled particles. They increase the thermal efficiency of processes, which is beneficial in coating dynamics since an extra mechanism is available for regulating heat transfer effects and more precisely manipulating finishing characteristics. It is observed that thickening of the thermal boundary layer and velocity are less pronounced in an *Ag*-water nanofluid than in a *Cu*-water nanofluid. In addition, since silver has a higher conductivity than copper, the temperature distribution in the *Ag*-water nanofluid is greater than in the *Cu*-water nanofluid.

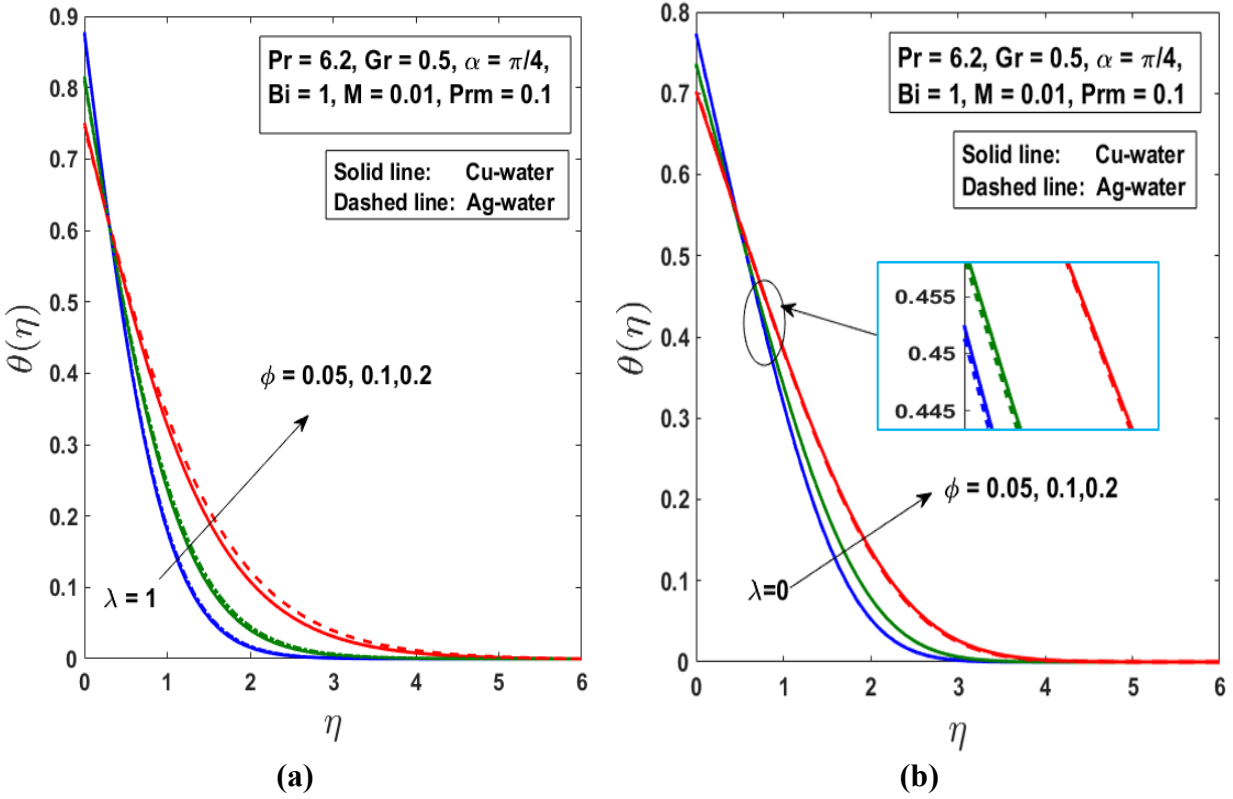
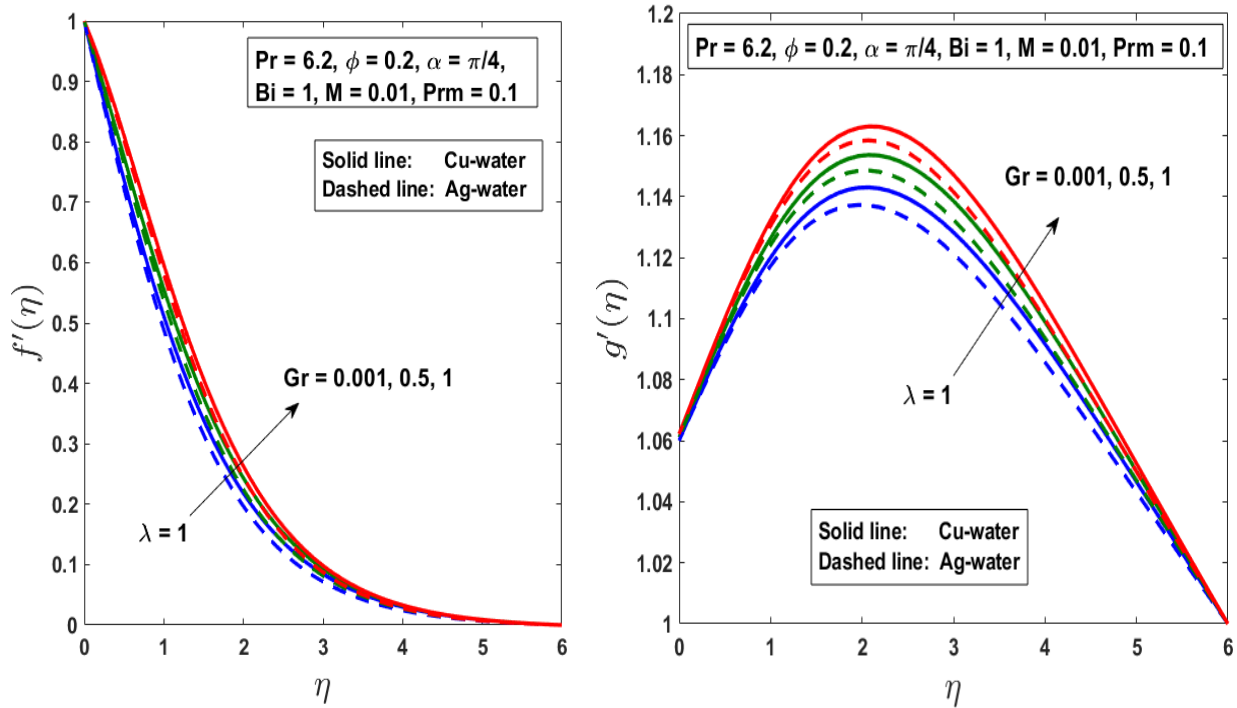


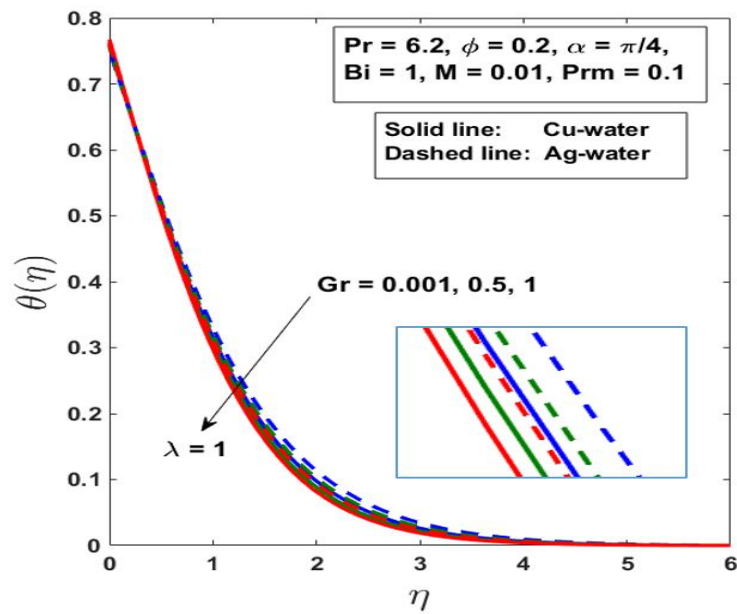
Fig. 4.4 Effect of nanoparticle value fraction ϕ on temperature for (a) $\lambda = 1$ and (b) $\lambda = 0$

The velocity, induced magnetic field, and temperature profiles for different values of the thermal Grashof number Gr are illustrated in Fig. 4.5 (a–c) for a moving plate ($\lambda = 1$). An increase in the thermal buoyancy parameter (the ratio of thermal buoyancy force to viscous hydrodynamic force, Gr) significantly boosts the velocity distribution by mobilizing more intense thermal convection currents near the wall (Fig. 4.5 (a)). As the buoyancy effect increases, the thermal convective influence on the nanoparticles is enhanced due to the intensification of free convection currents in the energy boundary layer, reducing the ambient heat diffusion. Hence, the thermofluid characteristics are strongly influenced by the Grashof number. Fig. 4.5 (b) shows that the induced magnetic field strengthens rapidly with increasing Gr .



(a)

(b)



(c)

Fig. 4.5 Effect of Grashof number Gr for $\lambda = 1$ on (a) velocity, (b) induced magnetic field, and (c) temperature

Despite the absence of the thermal buoyancy effect in the magnetic induction equation (4.9), there is a robust coupling between the magnetic induction and linear velocity fields via coupling equations (4.8) and (4.9). Therefore, the influence of the thermal buoyancy term in equation (4.8) is considerable. Fig. 4.5 (c) displays the physical behaviour of thermal buoyancy on the evolution of nanofluid temperature. A Grashof number $Gr > 0$ corresponds to free convection in which intensified thermal convection currents cool the moving plate, i.e., depletion of temperature near the plate with a point of inflection computed in the vicinity $\eta < 4$. Beyond this point, however, a heating effect is observed, i.e., the thermal boundary layer is thickened.

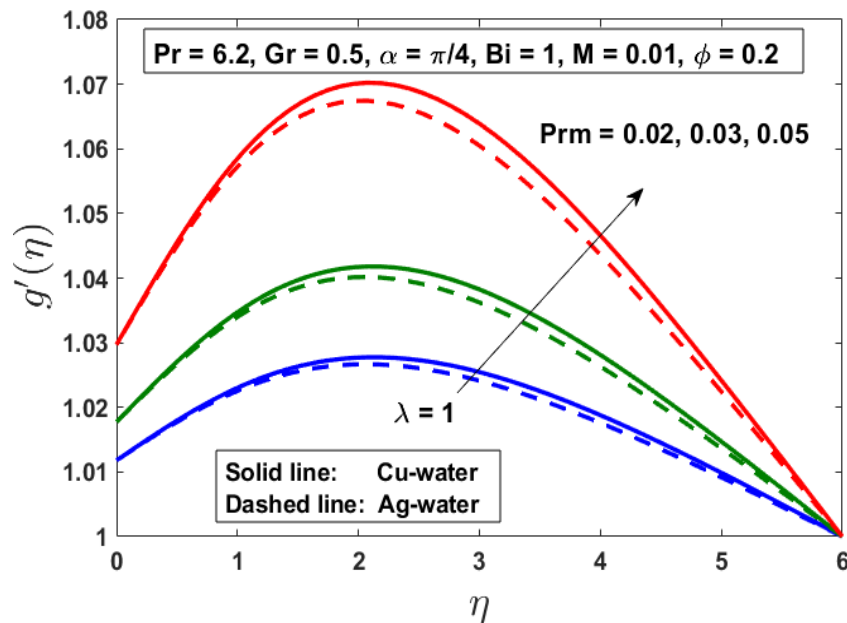


Fig. 4.6 Effect of magnetic Prandtl number Prm on induced magnetic field for $\lambda = 1$

Fig. 4.6 shows the response of the induced magnetic field component to an expanding dimensionless distance η , for several values of the dependent parameter magnetic Prandtl number, for moving flat plates with different nanoparticles. The nanofluid-induced magnetic field strengthens with rising values of the magnetic Prandtl number, because the boundary layer becomes thinner as the surface is moved. The copper nanoparticles consistently achieve the highest induced magnetic effect, while silver corresponds to a lower induced magnetic impact.

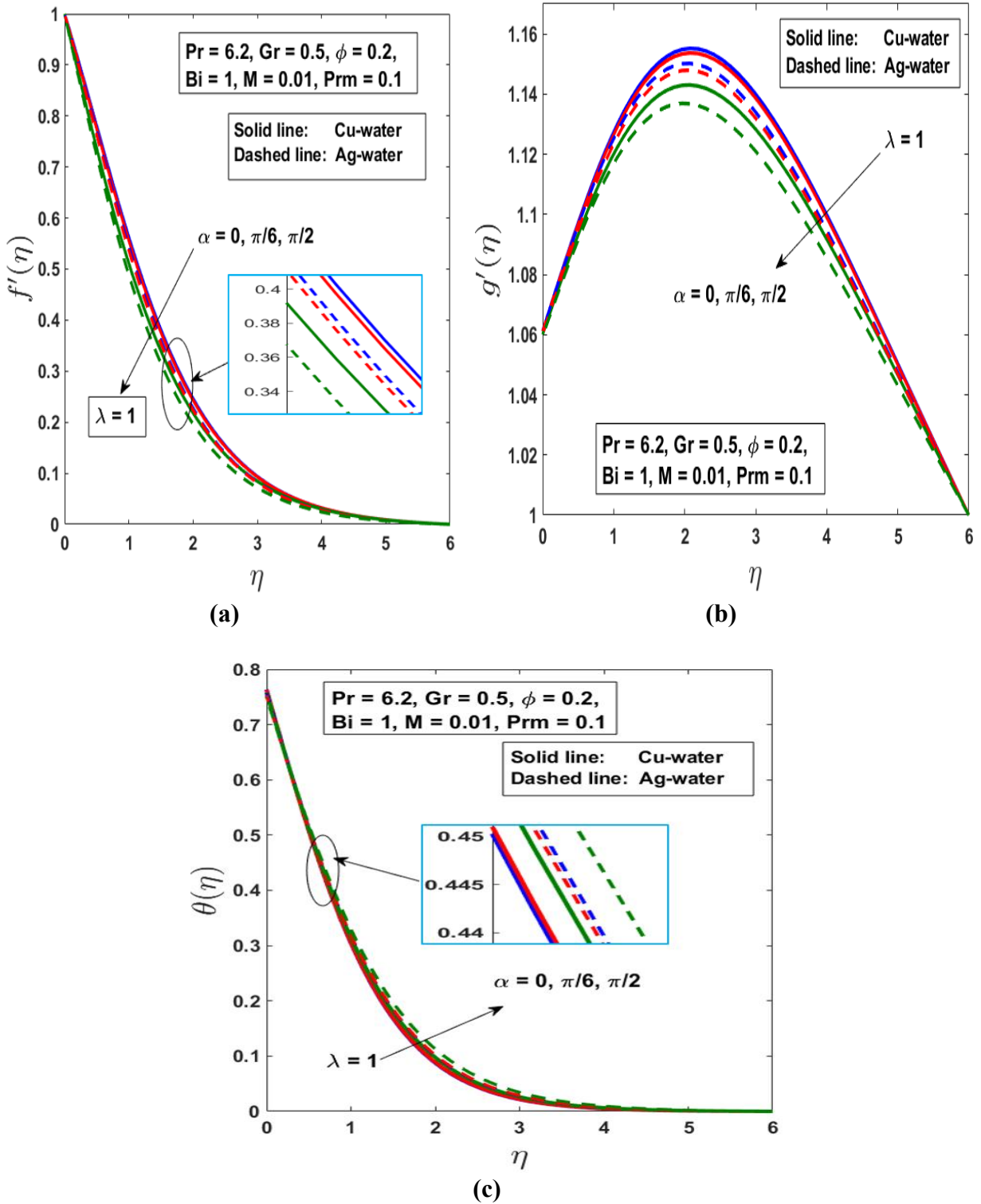


Fig. 4.7 Effect of inclined angle α for $\lambda = 1$ on (a) velocity, (b) induced magnetic field, and (c) temperature

Fig. 4.7 (a–c) demonstrates the influence of the angle of inclination α on the dimensionless velocity, induced magnetic field, and temperature profile for a moving flat plate for both the *Cu*-water and *Ag*-water nanofluids. The velocity and induced magnetic field strength both decrease with increasing values of α because the effect of the buoyancy force due to the thermal variations decreases by a factor of $\cos \alpha$, and consequently, the buoyancy force is maximum when $\alpha = 0$. The momentum boundary-layer thickness reduces due to the increasing values of α for both the *Cu*-water and *Ag*-water nanofluids. It is also observed that the nanofluid temperature increases with the angle of inclination, and that the thermal boundary-layer thickness for the *Ag*-water nanofluid is higher than for the *Cu*-water nanofluid.

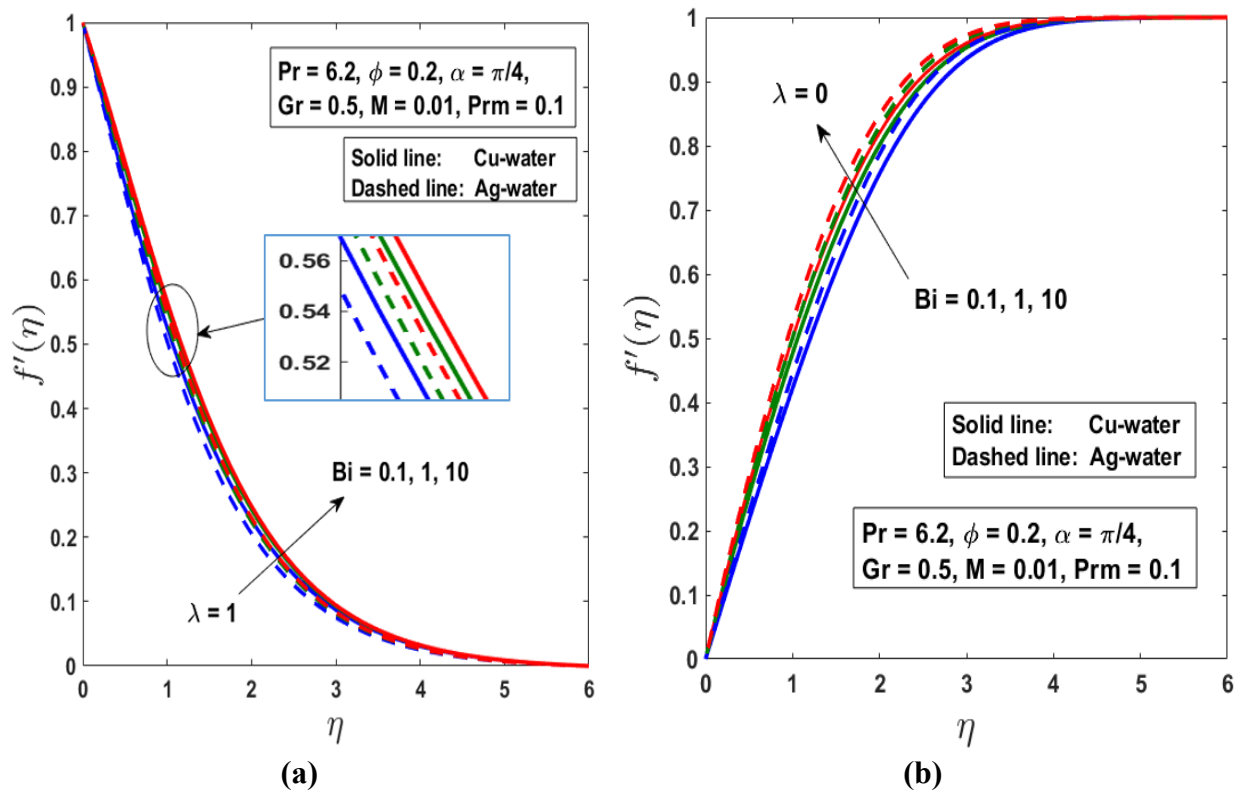


Fig. 4.8 Effect of Biot number Bi on velocity for (a) $\lambda = 1$ and (b) $\lambda = 0$

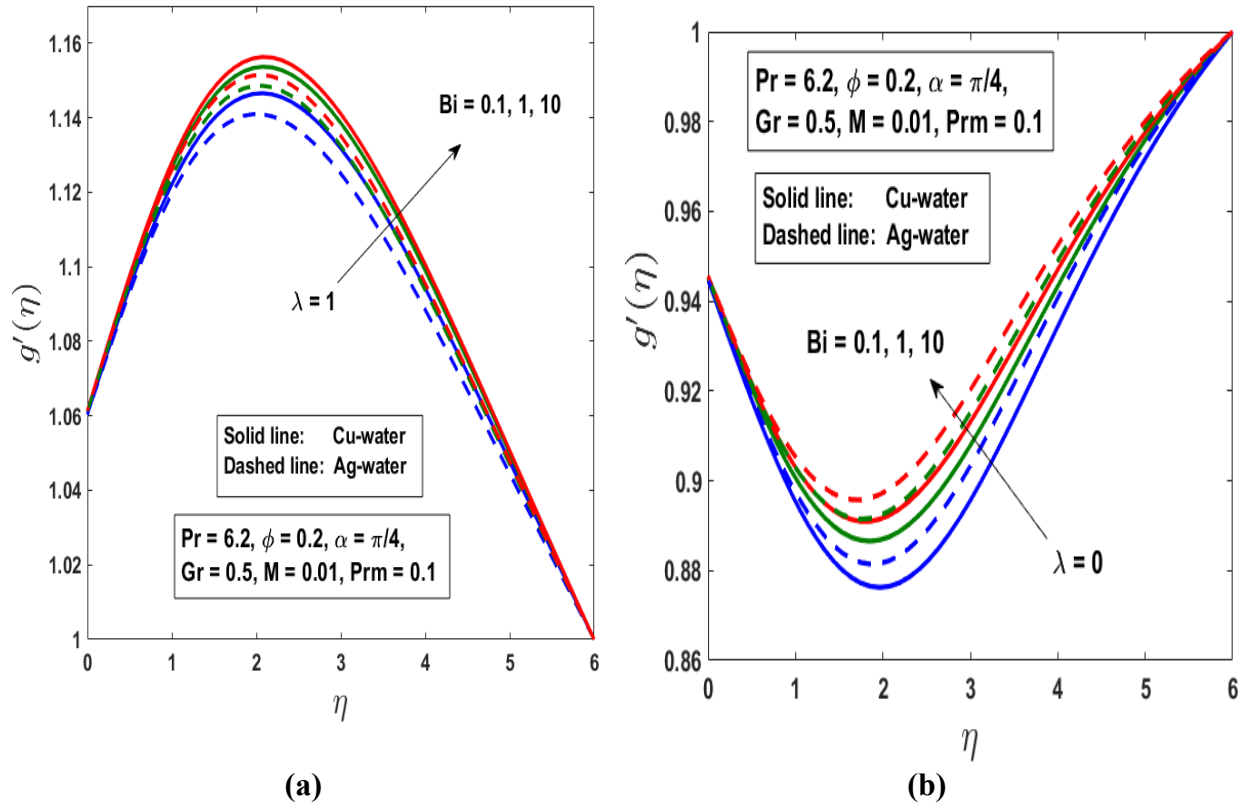


Fig. 4.9 Effect of Biot number Bi on induced magnetic field for (a) $\lambda = 1$ and (b) $\lambda = 0$

The impact of the nanoscale Biot number (Bi) on the nanofluid velocity, induced magnetic field, and temperature is displayed in Figs. 4.8–4.10 for the case of a stationary flat plate ($\lambda = 0$) and a moving flat plate ($\lambda = 1$) with Cu -water and Ag -water nanofluids, respectively. The Biot number measures the heat transfer in the form of a ratio of the resistance inside the body and at its surface. The momentum boundary-layer thickness and the induced magnetic field strength increase with the Biot number. In the case of the Cu -water nanofluid, the velocity and induced magnetic field are higher than those of the Ag -water nanofluid for a moving flat plate. The opposite trend is observed for a stationary flat plate. Higher values of Biot number ($\gg 1$) correspond to non-uniformity of the temperature fields within the object and are known as “thermally thick”. On the other hand, small Biot numbers ($\ll 1$) imply thermally simple or “thermally thin” scenarios due to uniform temperature fields inside the body. Temperatures significantly increase with the Biot number for both a stationary and moving flat plate. The silver nanoparticles consistently achieve the highest temperatures, while copper corresponds to the lowest temperatures. Hence, smooth

distributions are computed in the free stream, confirming that the MATLAB quadrature solution has employed a sufficiently large infinity boundary condition.

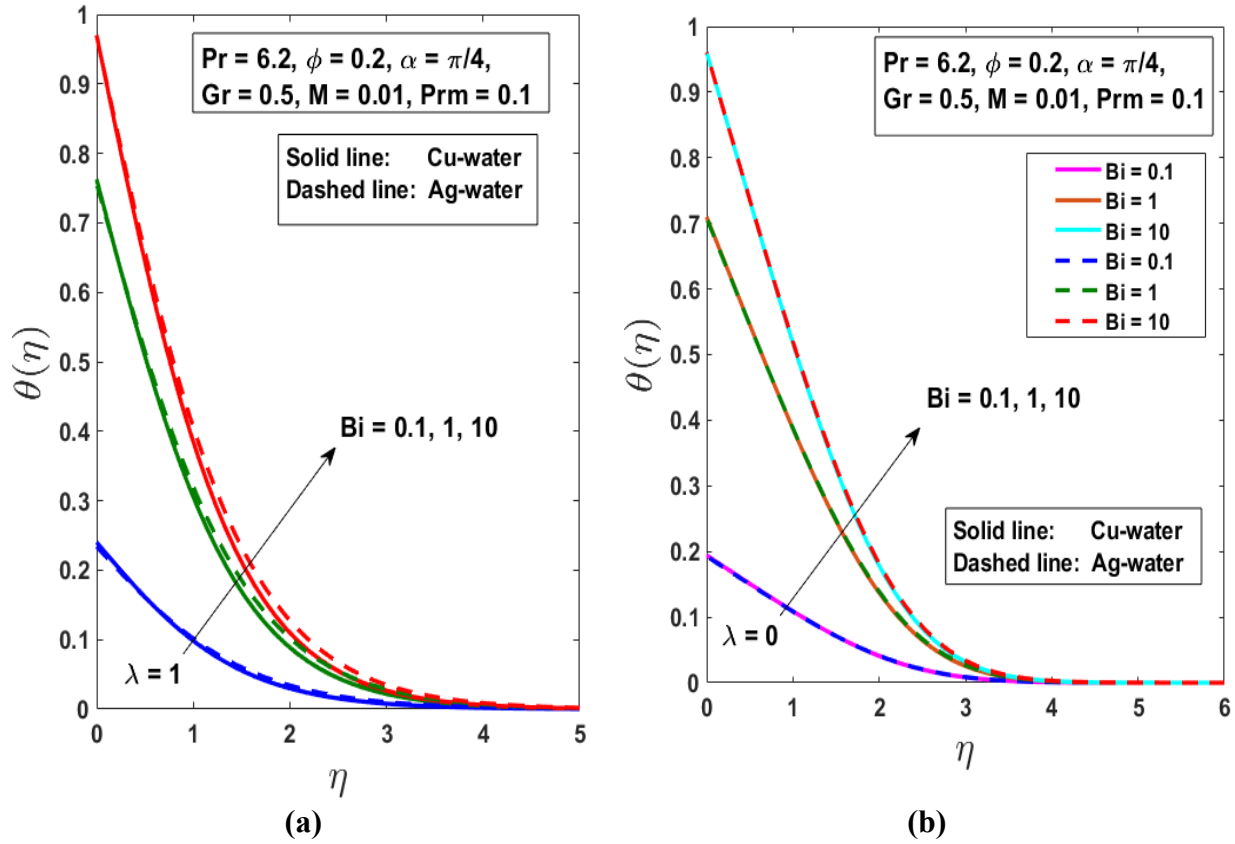


Fig. 4.10 Effect of Biot number Bi on temperature for (a) $\lambda = 1$ and (b) $\lambda = 0$

Shown in Fig. 4.11 (a–c) are the impacts of the magnetic parameter M on the velocity, induced magnetic field, and temperature for the moving flat plate with different nanoparticles. The body force inhibits the flow and acts transverse to the applied magnetic field, i.e., along the plate extrusion direction. The velocity and induced magnetic field increase with M for both nanoparticles, and this is associated with the anticipating nature of the body Lorentz force. The decrease in temperature for both metallic nanoparticles is reduced slightly as M increases.

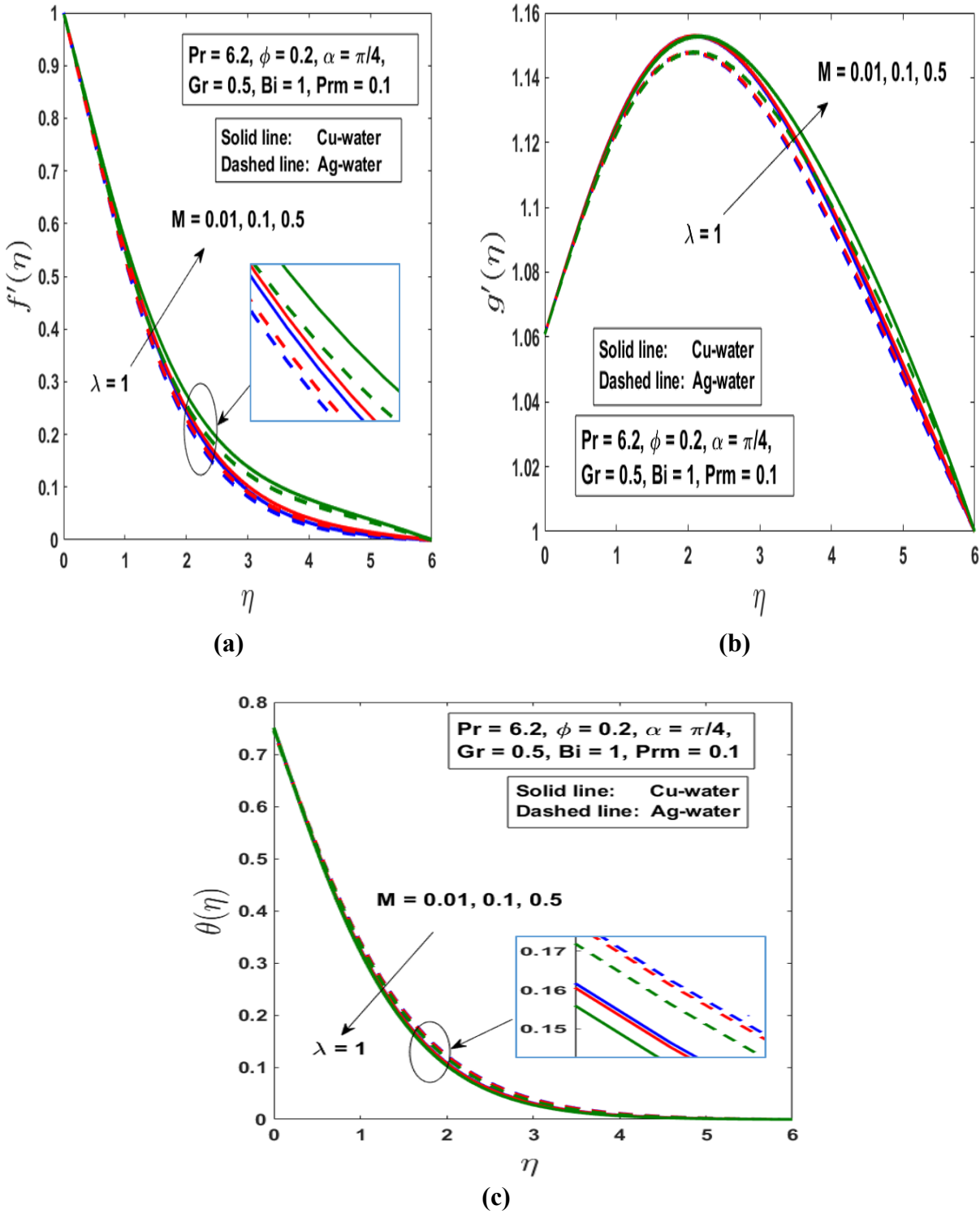
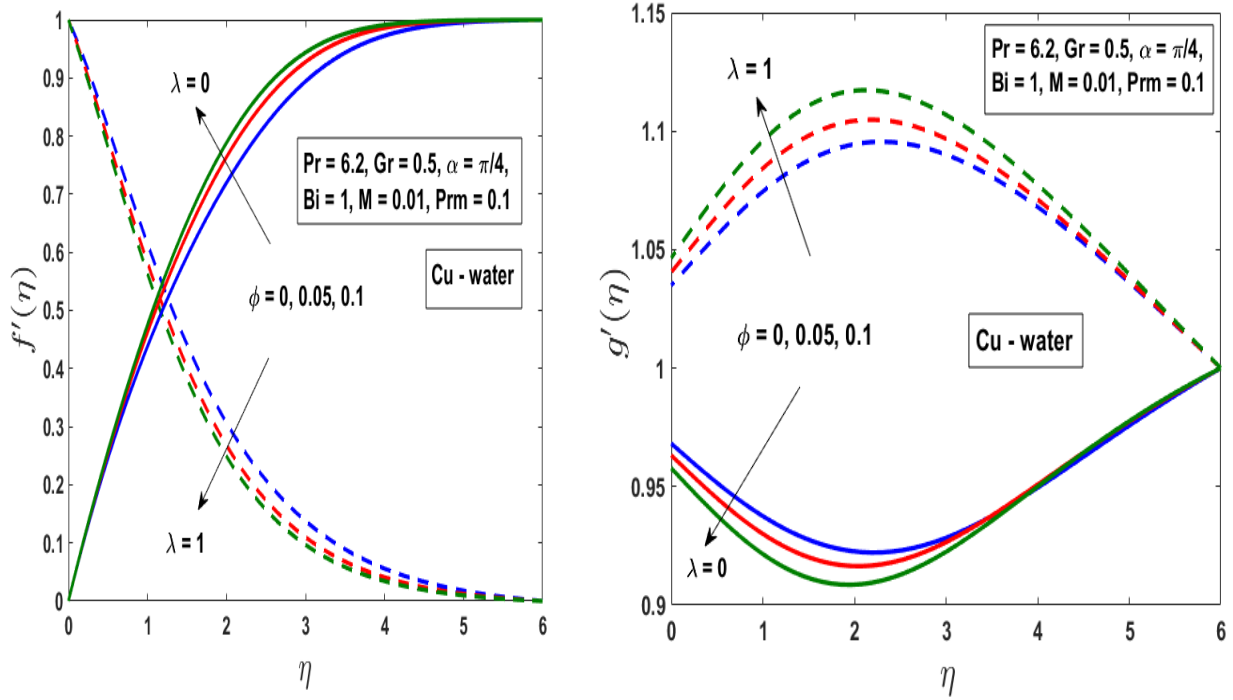


Fig. 4.11 Effect of magnetic interaction parameter M for $\lambda = 1$ on (a) velocity, (b) induced magnetic field, and (c) temperature

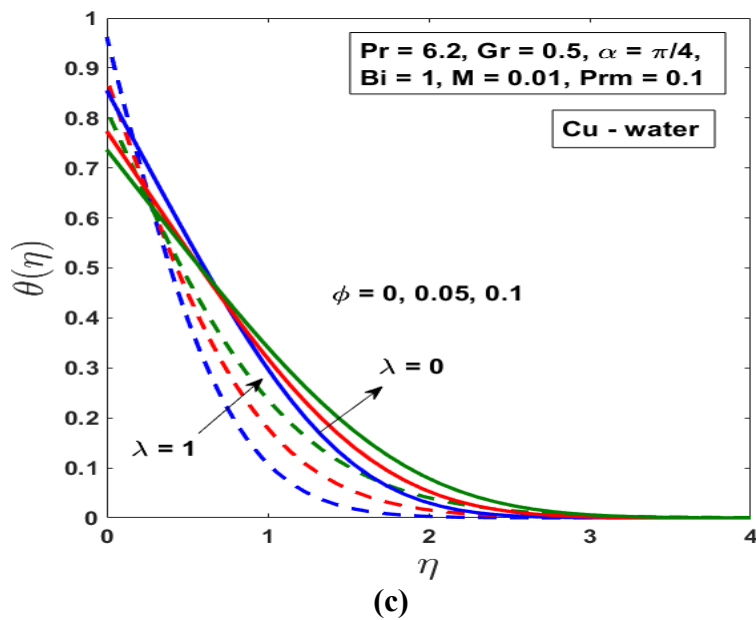
Fig. 4.12 (a–c) depicts the influence of the nanoparticle volume fraction ϕ on the velocity, induced magnetic field, and temperature profiles of *Cu*–water nanofluid for both a flat plate and a moving plate. As ϕ increases, the velocity is reduced, and the momentum boundary-layer thickness is increased for a moving flat plate, but the reverse phenomenon is observed for a stationary flat plate (Fig. 4.12(a)). The induced magnetic flow is strongly reduced with a higher fractional volume of nanoparticles for a stationary flat plate, and the opposite effect is observed for a moving plate (Fig. 4.12 (b)). Surprisingly, a strong increase in temperature is seen with higher nanoparticle volume fractions for both stationary and moving flat plates (Fig. 4.12 (c)). The flow distributions confirm the non-trivial effect of nanoparticle doping as a vital mechanism for elevating both convection and conduction coefficients. Hence, copper nanoparticles are effective for energizing base fluids without the clogging effects encountered with micro-scaled particles. The influence of the Magnetic field parameter M on velocity, induced magnetic field, and temperature profiles for *Ag*–water nanofluid, for both a flat plate and a moving plate, is shown in Fig. 4.13 (a–c). A higher magnetic parameter reduces the velocity in the case of a stationary flat plate and increases it in the case of a moving flat plate (Fig. 4.13 (a)). Meanwhile, the induced magnetic field decreases with the magnetic field for a stationary flat plate and increases for a moving flat plate (Fig. 4.13 (b)). The temperature profiles increase for a stationary flat plate and decrease for a moving flat plate (Fig. 4.13 (c)).

The influence of the skin friction coefficient C_f and the reduced Nusselt number Nu for various values of nanoparticle volume fraction ϕ and magnetic interaction parameter M , for both the *Cu*–water and *Ag*–water nanofluids in the case of $\lambda = 0$, are highlighted in Figs. 4.14 and 4.15. The skin friction coefficient C_f increases monotonically with ϕ and M for both types of nanofluids. The opposite trend is observed for the heat transfer rate. The maximum skin friction value in the *Ag*–water nanofluid case is achieved at a higher nanoparticle volume fraction ϕ and magnetic parameter M . The *Ag*–water nanofluid exhibits a lower wall heat transfer rate than the *Cu*–water nanofluid. The presence of nanoparticles increases the skin friction coefficient and decreases the wall heat transfer rate with increasing values of ϕ and M for the stationary flat plate.



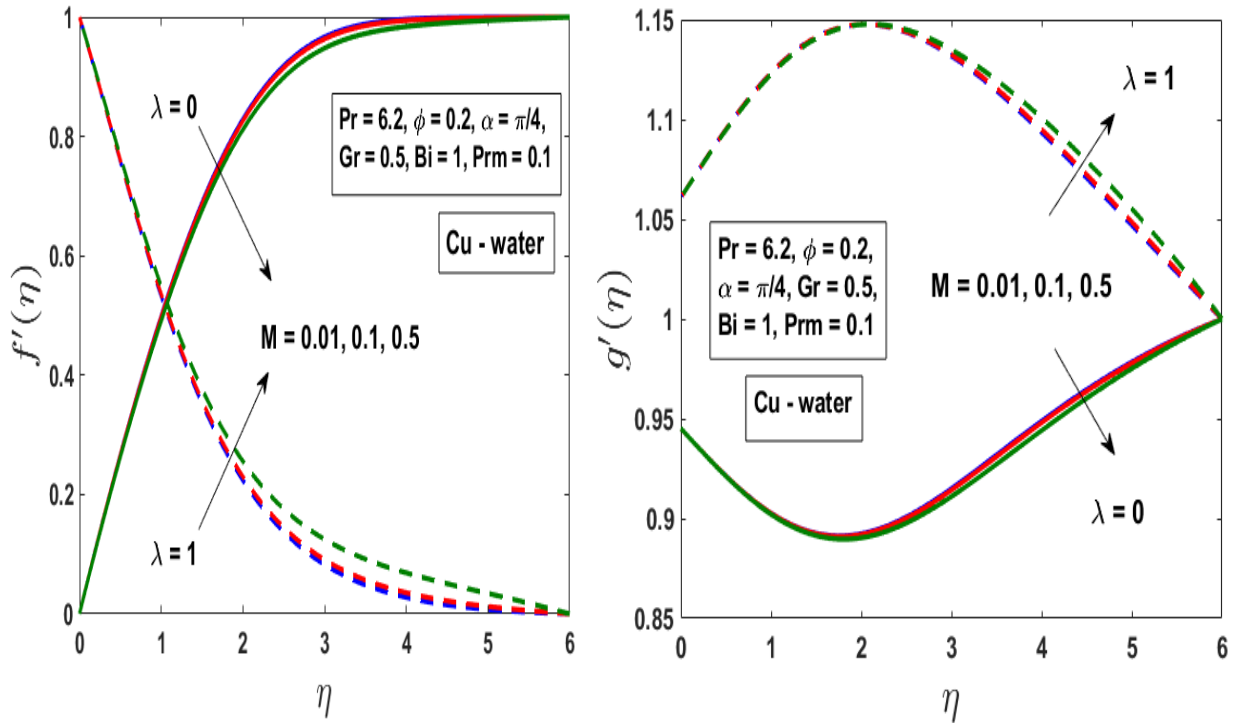
(a)

(b)



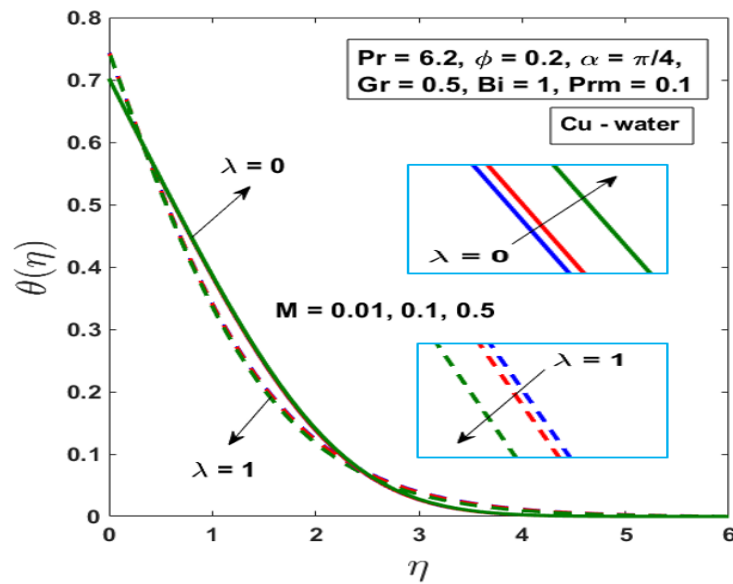
(c)

Fig. 4.12 Effect of nanoparticle value fraction ϕ for both $\lambda = 0$ and $\lambda = 1$ on (a) velocity, (b) induced magnetic field, and (c) temperature



(a)

(b)



(c)

Fig. 4.13 Effect of magnetic interaction parameter M for both $\lambda = 0$ and $\lambda = 1$ on (a) velocity, (b) induced magnetic field, and (c) temperature

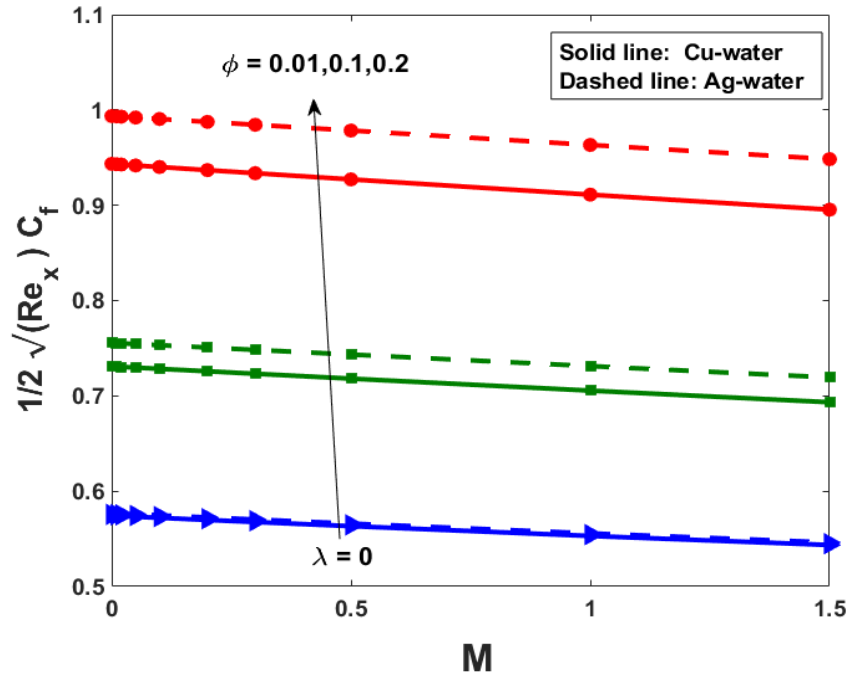


Fig 4.14 Influence of ϕ and M on skin friction coefficient C_f for $\lambda = 0$ when $Gr = 0.5$, $Pr = 6.2$, $\alpha = 45^\circ$, $Bi = 1$, and $Prm = 0.1$

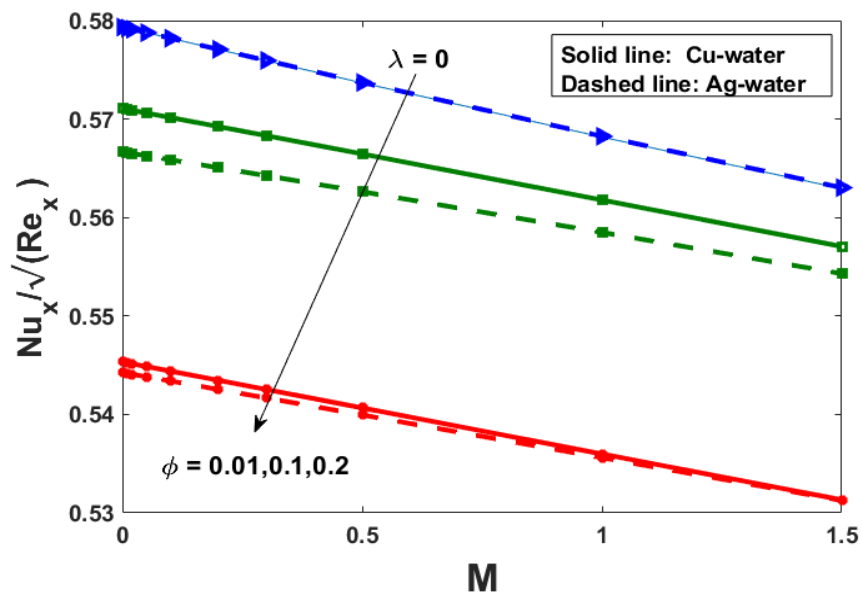


Fig 4.15 Influence of ϕ and M on reduced Nusselt number Nu for $\lambda = 0$ when $Gr = 0.5$, $Pr = 6.2$, $\alpha = 45^\circ$, $Bi = 1$, and $Prm = 0.1$

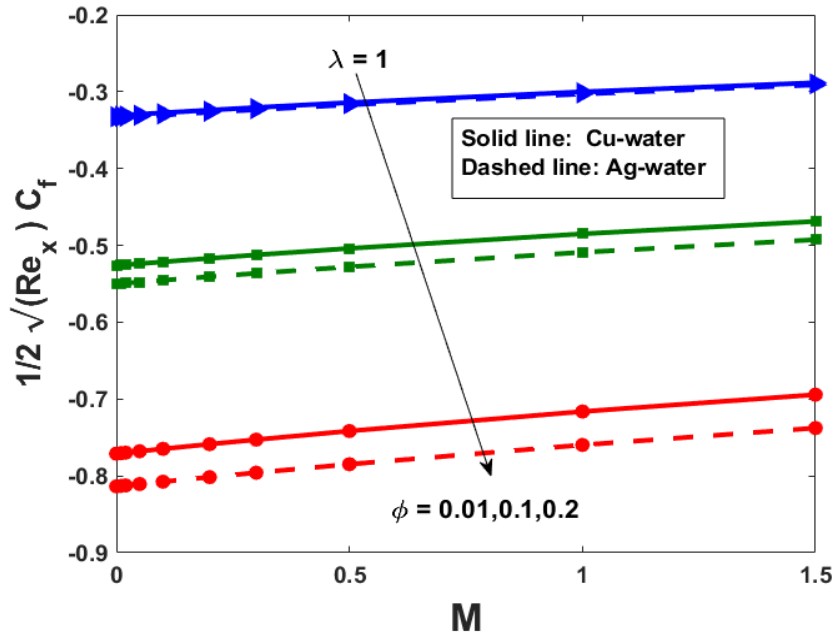


Fig. 4.16 Influence of ϕ and M on skin friction coefficient C_f for $\lambda = 1$ when $Gr = 0.5$, $Pr = 6.2$, $\alpha = 45^\circ$, $Bi = 1$, and $Prm = 0.1$

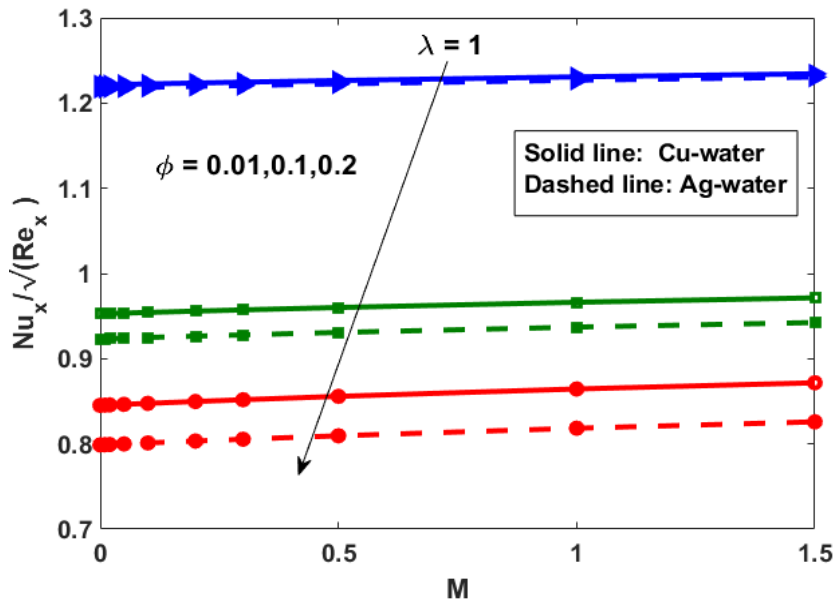


Fig. 4.17 Influence of ϕ and M on reduced Nusselt number Nu for $\lambda = 1$ when $Gr = 0.5$, $Pr = 6.2$, $\alpha = 45^\circ$, $Bi = 1$, $Prm = 0.1$

Figs. 4.16 and 4.17 show the combined effect of nanoparticle value fraction ϕ and magnetic interaction parameter M on the skin friction coefficient C_f and the reduced Nusselt number Nu in the case of $\lambda = 1$ for Cu -water and Ag -water nanofluids. The values of the skin friction coefficient and reduced Nusselt number decrease as ϕ and M increase for both types of nanofluids. It is found that the Cu -water nanofluid exhibits higher drag than the Ag -water nanofluid. It is also noted that the nanofluid with Cu particles has a higher heat transfer rate for a moving plate than the nanofluid with Ag nanoparticles.

4.4 Summary

A computational and theoretical study of hydromagnetic metallic nanofluid flows with induced magnetic field effects on an inclined stationary/moving flat plate has been conducted, adopting convective boundary conditions. A nanoscale formulation with the Tiwari–Das model has been employed, assuming that the nanoparticle volume fraction at the boundary surface can be actively regulated. Validation of the MATLAB SRM code with published results is included. The numerical solutions obtained have been compared with previously published results, showing good agreement. The influence of the different dimensionless parameters on the velocity, induced magnetic field, and temperature profiles have been illustrated and discussed.

Chapter 5

MHD Boundary-Layer Slip Flow with an Induced Magnetic Field Simulated by Space- and Temperature-Dependent Internal Heat Generation/Absorption over a Moving Plate

This chapter investigates the combined effects of space- and temperature-dependent internal heat generation/absorption on the MHD heat transfer flow of an electrically conducting water-based nanofluid, under the influence of slip, over a moving plate, with the effect of an induced magnetic field. The physical laws governing the fluid flow are modelled as a system of PDEs and then condensed into equivalent nonlinear ODEs with similar variables. The solutions for the flow and heat transfer characteristics are evaluated numerically for various values of the embedded parameters describing the motion, induced magnetic field, and heat transfer properties. These are presented with plots and tables and discussed in detail. The skin friction coefficient and heat transfer rate are also studied. To obtain a clear insight into the physical problem, the results are discussed with the help of graphical illustrations for Cu -water nanofluid.

5.1 Problem Formulation

Consider a steady two-dimensional laminar boundary-layer flow of a nanofluid with an induced magnetic field over a flat plate moving in the same direction, or the opposite direction, to the free stream. The physical model with detailed geometries is shown in Fig. 5.1 (a–b). The basic equations for incompressible flow and electrically conducting nanofluid, as described by Cowling (1957), can be represented in vectorial form as follows:

$$\nabla \cdot \mathbf{v} = 0$$

$$\nabla \cdot \mathbf{H} = 0$$

$$(\mathbf{v} \cdot \nabla) \mathbf{v} - \frac{\mu_e}{4\pi\rho_{nf}} (\mathbf{H} \cdot \nabla) \mathbf{H} = \frac{\mu_{nf}}{\rho_{nf}} \nabla^2 \mathbf{v}$$

$$\nabla \times (\nabla \times \mathbf{H}) + \zeta_0 \frac{\sigma_{nf}}{\sigma_f} \nabla^2 \mathbf{H} = 0$$

$$(\mathbf{v} \cdot \nabla) T = \frac{k_{nf}}{(\rho C_p)_{nf}} \nabla^2 T$$

Where $\zeta_0 = 1/4\pi\sigma_f\mu_e$ is the magnetic diffusivity, and the wall temperature is $T_w > T_\infty$. An induced magnetic field of strength H_0 is applied orthogonal to the plate; in the free stream, H_x becomes H_0 while H_y vanishes near the wall.

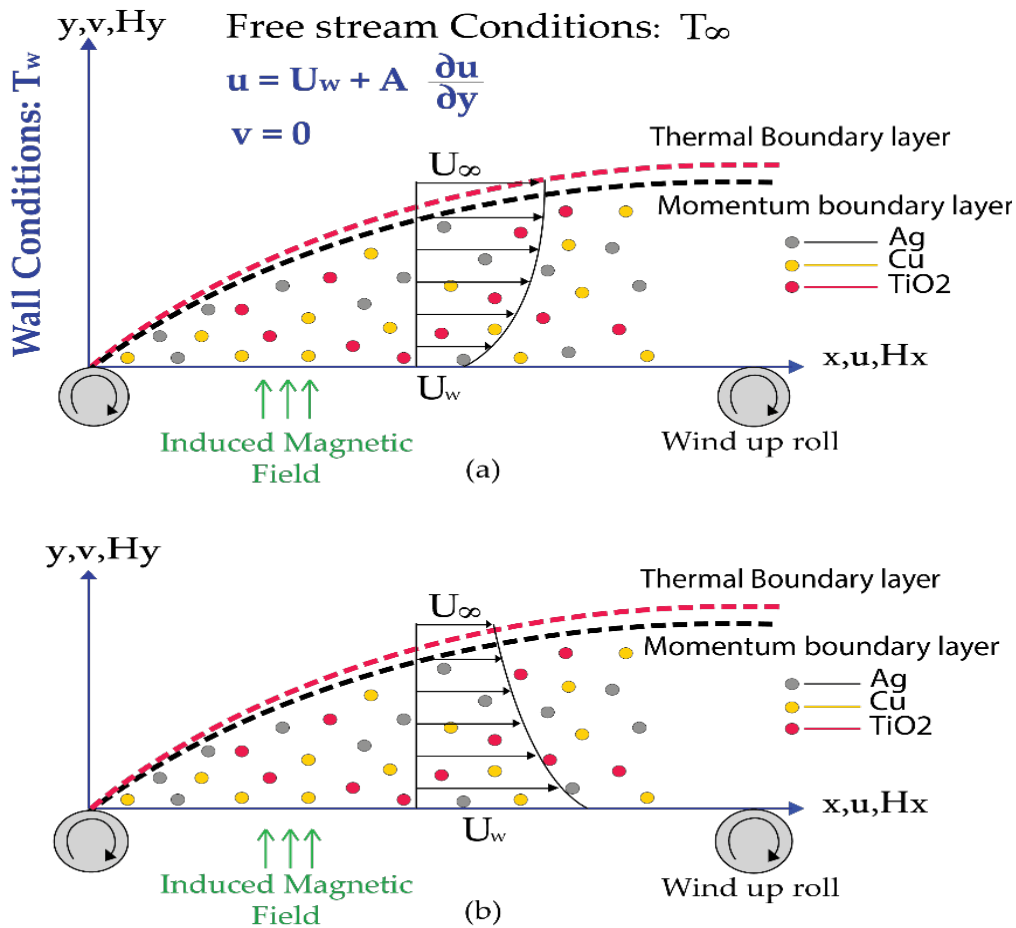


Fig. 5.1 Coordinates and the physical model

With the assumptions and approximations mentioned above, and following the nanofluid model proposed by Tiwari (2007), the governing mass, momentum-induced magnetic field, and energy equations are described by

$$\frac{\partial u}{\partial x} + \frac{\partial v}{\partial y} = 0 \quad (5.1)$$

$$\frac{\partial H_x}{\partial x} + \frac{\partial H_y}{\partial y} = 0 \quad (5.2)$$

$$u \frac{\partial u}{\partial x} + v \frac{\partial u}{\partial y} = \frac{\mu_{nf}}{\rho_{nf}} \frac{\partial^2 u}{\partial y^2} + \frac{\mu_e}{4\pi\rho_{nf}} \left(H_x \frac{\partial H_x}{\partial x} + H_y \frac{\partial H_x}{\partial y} \right) \quad (5.3)$$

$$u \frac{\partial H_x}{\partial x} + v \frac{\partial H_x}{\partial y} - H_x \frac{\partial u}{\partial x} - H_y \frac{\partial u}{\partial y} = \zeta_0 \frac{\sigma_{nf}}{\sigma_f} \frac{\partial^2 H_x}{\partial y^2} \quad (5.4)$$

$$u \frac{\partial T}{\partial x} + v \frac{\partial T}{\partial y} = \frac{k_{nf}}{(\rho C_p)_{nf}} \frac{\partial^2 T}{\partial y^2} + \frac{q'''}{(\rho C_p)_{nf}} \quad (5.5)$$

Here, q''' is the space- and temperature-dependent internal heat generation (> 0) or absorption (< 0 ; Abdul *et al.*, 2014), which can be expressed for this problem as

$$q''' = \left(\frac{K_{nf} U_w}{x \nu_{nf}} \right) [A^*(T_w - T_\infty) f'(\eta) + B^*(T - T_\infty)] \quad (5.6)$$

Therefore, equation (5.5) can be simplified to

$$u \frac{\partial T}{\partial x} + v \frac{\partial T}{\partial y} = \frac{k_{nf}}{(\rho C_p)_{nf}} \frac{\partial^2 T}{\partial y^2} + \left(\frac{K_{nf} U_w}{x \nu_{nf} (\rho C_p)_{nf}} \right) [A^*(T_w - T_\infty) f'(\eta) + B^*(T - T_\infty)] \quad (5.7)$$

The appropriate boundary conditions for the current study are as follows:

$$\left. \begin{aligned} u = U_w + A \frac{\partial u}{\partial y}, \quad v = 0, \quad \frac{\partial H_x}{\partial y} = H_y = 0, \quad T = T_w \quad \text{At} \quad y = 0 \\ u \rightarrow U_\infty, \quad H_x \rightarrow H_0, \quad T \rightarrow T_\infty \quad \text{At} \quad y \rightarrow \infty \end{aligned} \right\} \quad (5.8)$$

Taken from the work of Abu Nada (2008), the thermophysical properties of fluid and nanoparticles are listed in Table 5.1. The fluid is water-based and contains a variety of nanoparticles, including

copper (Cu), silver (Ag), and titanium oxide (TiO_2). Oztop *et al.* (2008) provide the characteristics of nanofluids, which are noted to be independent of nanoparticle motion:

$$\begin{aligned} \nu_{nf} &= \frac{\mu_{nf}}{\rho_{nf}}, & \mu_{nf} &= \frac{\mu_f}{(1-\phi)^{2.5}}, & \rho_{nf} &= (1-\phi)\rho_f + \phi\rho_s \\ \alpha_{nf} &= \frac{k_{nf}}{(\rho C_p)_{nf}}, & (\rho C_p)_{nf} &= (1-\phi)(\rho C_p)_f + \phi(\rho C_p)_s \\ \frac{\sigma_{nf}}{\sigma_f} &= 1 + \frac{3((\sigma_s/\sigma_f)-1)\phi}{((\sigma_s/\sigma_f)+2)-\phi((\sigma_s/\sigma_f)-1)}, & \frac{k_{nf}}{k_f} &= \frac{1-\phi+2\phi\frac{k_s}{k_s-k_f}\ln\frac{k_s+k_f}{2k_f}}{1-\phi+2\phi\frac{k_f}{k_s-k_f}\ln\frac{k_s+k_f}{2k_f}} \end{aligned}$$

Table 5.1 Thermophysical properties of the base fluid and nanoparticles

Physical property	Base fluid (water)	Cu	Ag	TiO_2
C_p ($J/kg \cdot K$)	4,179	385	235	686.2
ρ (kg/m^3)	997.1	8,933	10,500	4250
k ($W/m \cdot K$)	0.613	401	429	8.9538
σ (S/m)	0.05	5.96×10^7	3.6×10^7	2.6×10^6

In accordance with Ellahi *et al.* (2018), we will now introduce the following non-dimensional variables in order to streamline the mathematical analysis:

$$\psi = (U_\infty \nu_f x)^{\frac{1}{2}} f(\eta), \quad \Phi = \left(\frac{\nu_f x}{U_\infty}\right)^{\frac{1}{2}} H_0 g(\eta), \quad \theta(\eta) = \frac{T-T_\infty}{T_w-T_\infty}, \quad \eta = \frac{y}{2} \left(\frac{U_\infty}{\nu_f x}\right)^{\frac{1}{2}} \quad (5.9)$$

The continuity equations are satisfied by the stream functions in such a way that

$$u = \frac{\partial \psi}{\partial y} \quad \text{and} \quad v = -\frac{\partial \psi}{\partial x} \quad (5.10)$$

$$H_x = \frac{\partial \Phi}{\partial y} \quad \text{and} \quad H_y = -\frac{\partial \Phi}{\partial x} \quad (5.11)$$

Modifying the governing equations (5.1)–(5.5) by using (5.9)–(5.11), along with the boundary conditions (5.8), reduces them to the following non-dimensional form:

$$\frac{1}{a_1} f'''' + f f'' - \frac{M}{a_2} g g'' = 0 \quad (5.12)$$

$$a_3 \chi g'''' + f g'' - g f'' = 0 \quad (5.13)$$

$$a_4 \theta'' + Pr a_5 f \theta' + 2\lambda a_1 a_4 [A^* f' + B^* \theta] = 0 \quad (5.14)$$

where

$$a_1 = (1 - \phi)^{2.5} \left(1 - \phi + \phi \frac{\rho_s}{\rho_f}\right)$$

$$a_2 = 1 - \phi + \phi \frac{\rho_s}{\rho_f}$$

$$a_3 = \frac{\sigma_{nf}}{\sigma_f} = 1 + \frac{3((\sigma_s/\sigma_f) - 1)\phi}{((\sigma_s/\sigma_f) + 2) - \phi((\sigma_s/\sigma_f) - 1)}$$

$$a_4 = \frac{k_{nf}}{k_f} = \frac{(k_s + 2k_f) - 2\phi(k_f - k_s)}{(k_s + 2k_f) + \phi(k_f - k_s)}$$

$$a_5 = 1 - \phi + \phi \frac{(\rho C_p)_s}{(\rho C_p)_f}$$

The corresponding boundary conditions are

$$\left. \begin{aligned} f(0) = 0, f'(0) = \lambda + \alpha f''(0), g(0) = g''(0) = 0, \theta(0) = 1 \text{ as } \eta = 0 \\ f' \rightarrow 1, g' \rightarrow 1, \theta \rightarrow 0 \quad \text{as } \eta \rightarrow \infty \end{aligned} \right\} \quad (5.15)$$

In the above equations, $\lambda = U_w/U_\infty$ represents the velocity ratio of the plate, $\alpha = A\sqrt{u_\infty/2\nu_f x}$ is the slip parameter, $M = \mu_e H_0^2 / 4\pi\mu_\infty^2 \rho_f$ is the magnetic parameter, $\chi = \zeta_0/\nu_f$ is the reciprocal magnetic parameter, and $Pr = \nu_f(\rho C_p)_f/k_f$ is the Prandtl number.

Other quantities of interest are given by

$$C_f = \frac{\tau_w}{\rho_f U_\infty^2} \quad \text{and} \quad Nu_x = \frac{x q_w}{K_f (T_w - T_\infty)} \quad (5.16)$$

where C_f denotes the skin friction coefficient and Nu_x denotes the rate of heat transfer.

Moreover, τ_w and q_w are given by

$$\tau_w = \mu_{nf} \left(\frac{\partial u}{\partial y} \right)_{y=0} \quad \text{and} \quad q_w = -k_{nf} \left(\frac{\partial T}{\partial y} \right)_{y=0} \quad (5.17)$$

Using variables (5.10), (5.11), (5.16), and (5.17), we obtain

$$\sqrt{Re_x} C_f = \frac{1}{4(1-\phi)^{2.5}} f''(0) \quad \text{and} \quad (Re_x/2)^{-1/2} Nu_x = -\phi_4 \theta'(0) \quad (5.18)$$

5.2 Spectral Relaxation Method Simulation

The SRM is used to solve the system of nonlinear PDEs (5.1)–(5.5). We define $f'(\eta) = F(\eta)$ and $g'(\eta) = G(\eta)$ and then arrange the problem into the following iteration scheme:

$$f'_{r+1} = F_{r+1} \quad (5.19)$$

$$\frac{1}{a_1} F''_{r+1} + f_r F'_{r+1} - \frac{M}{a_2} g_r G'_r = 0 \quad (5.20)$$

$$g'_{r+1} = G_{r+1} \quad (5.21)$$

$$a_3 \chi G''_{r+1} + f_{r+1} G'_{r+1} - g_r F'_{r+1} = 0 \quad (5.22)$$

$$a_4 \theta''_{r+1} + Pr a_5 f_{r+1} \theta'_{r+1} + 2\lambda a_1 a_4 [A^* F_{r+1} + B^* \theta_{r+1}] = 0 \quad (5.23)$$

The boundary conditions are as follows:

$$F_{r+1}(0) = \lambda + \alpha F'_{r+1}(0), \quad F_{r+1}(\infty) = 1 \quad (5.24)$$

$$f_{r+1}(0) = 0 \quad (5.25)$$

$$G'_{r+1}(0) = 0, \quad G'_{r+1}(\infty) = 1 \quad (5.26)$$

$$g_{r+1}(0) = 0 \quad (5.27)$$

$$\theta'_{r+1}(0) = 1, \theta_{r+1}(\infty) = 0 \quad (5.28)$$

The following matrix equations are obtained in discretizing equations (5.19)–(5.28), employing the Chebyshev pseudo-spectral method:

$$S_1 \mathbf{F}_{r+1} = R_1, \quad F_{r+1}(\xi_N) = 1, F_{r+1}(\xi_0) = \lambda + \alpha F'_{r+1}(\xi_0) \quad (5.29)$$

$$S_2 \mathbf{f}_{r+1} = R_2, \quad f_{r+1}(\xi_N) = 0 \quad (5.30)$$

$$S_3 \mathbf{G}_{r+1} = R_3, \quad G_{r+1}(\xi_N) = 1, G'_{r+1}(\xi_0) = 0 \quad (5.31)$$

$$S_4 \mathbf{g}_{r+1} = R_4, \quad g_{r+1}(\xi_N) = 0 \quad (5.32)$$

$$S_5 \boldsymbol{\theta}_{r+1} = R_5, \quad \theta_{r+1}(\xi_N) = 0, \theta'_{r+1}(\xi_0) = 1 \quad (5.33)$$

where

$$S_1 = \text{diag}\left(\frac{1}{a_1}\right) \mathbf{D}^2 + \text{diag}(\mathbf{f}_r) \mathbf{D}, \quad R_1 = \frac{M}{a_2} \mathbf{g}_r \mathbf{G}'_r \quad (5.34)$$

$$S_2 = \mathbf{D}, \quad R_2 = \mathbf{F}_{r+1} \quad (5.35)$$

$$S_3 = \text{diag}(a_3 \chi) \mathbf{D}^2 + \text{diag}(\mathbf{f}_{r+1}) \mathbf{D}, \quad R_3 = \mathbf{g}_r \mathbf{F}'_{r+1} \quad (5.36)$$

$$S_4 = \mathbf{D}, \quad R_4 = \mathbf{G}_{r+1} \quad (5.37)$$

$$S_5 = \text{diag}(a_4) \mathbf{D}^2 + \text{diag}(\text{Pr} a_5 \mathbf{f}_{r+1}) \mathbf{D} + 2\lambda a_1 a_4 B^* \mathbf{I}, \quad R_5 = -2\lambda a_1 a_4 A^* \mathbf{F}_{r+1} \quad (5.38)$$

The SRM scheme is represented by equations (5.29) to (5.38), which can be resolved through the application of the spectral collocation technique. The initial approximation needed to begin the iteration process can be chosen as a function that fulfils the underlying boundary conditions and is based on known physical considerations of the flow parameters. For the governing problem, a suitable set of initial assumptions is

$$f_0(\eta) = (1 + \lambda + \alpha)\eta + e^{-\eta}, \quad g_0(\eta) = \eta - (1 + \eta)e^{-\eta} + 1, \quad \theta_0(\eta) = e^{-\eta} \quad (5.39)$$

Starting with the preliminary predictions (5.39), the SRM scheme (5.29)–(5.38) is executed iteratively until the following criterion is attained:

$$\max(\|F_{r+1} - F_r\|; \|G_{r+1} - G_r\|; \|\theta_{r+1} - \theta_r\|) < E_r$$

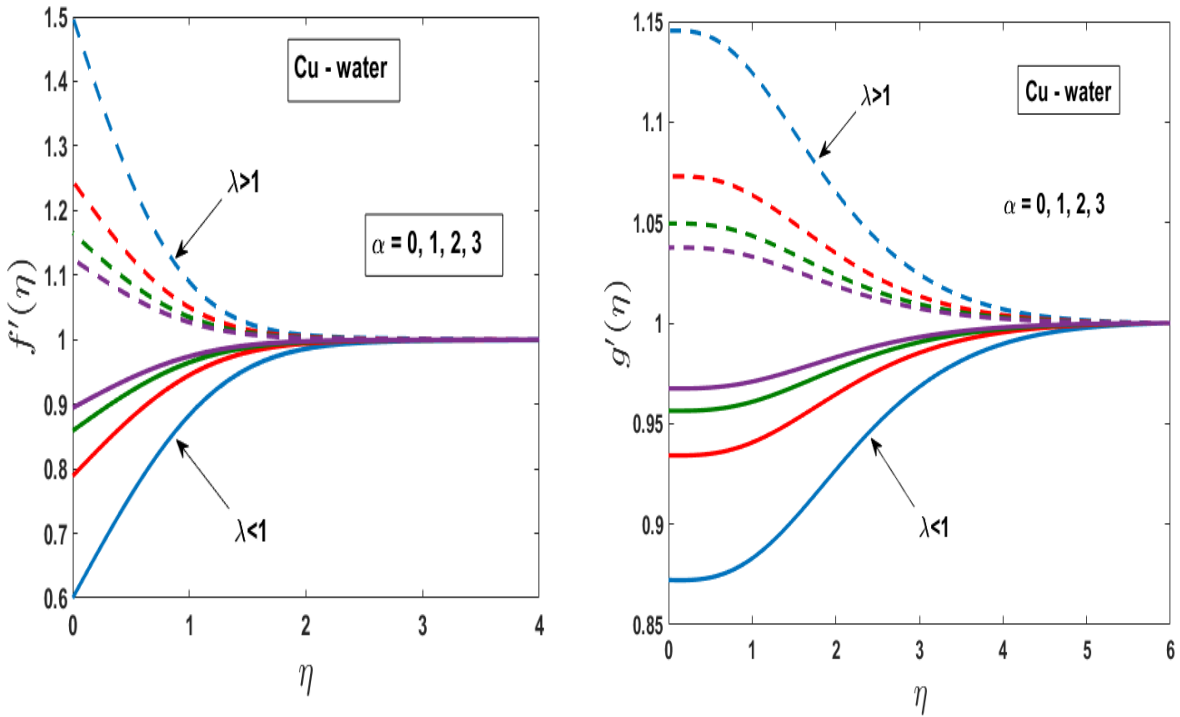
where E_r is a pre-set error tolerance. For the purposes of this study, $E_r = 10^{-6}$.

5.3 Findings and Discussion

The nonlinear system of coupled equations (5.10)–(5.12), together with the boundary conditions (5.15), is solved numerically using the SRM. Fig. 5.1 (a) displays the hydrodynamic boundary layer over a plate when it moves more slowly than the free stream velocity, i.e., $\lambda < 1$. The boundary layer becomes narrower in this scenario because the difference between the maximum and minimum velocity vectors is smaller. This trend continues until the plate outpaces the fluid, i.e., $\lambda > 1$. When a plate pulls on the fluid adjacent to it, the friction force becomes inverse, and the boundary-layer thickness grows with λ , as shown in Fig. 5.1 (b).

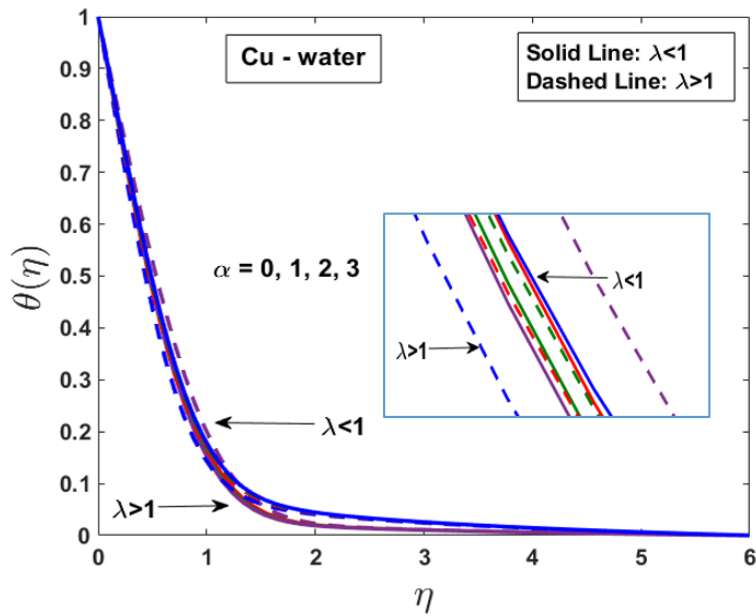
The current results are described using graphical depictions of *Cu*–water nanofluid to explain the physical situation thoroughly. Extensive computations have been conducted to identify the influences of slip parameter, magnetic parameter, nanoparticle volume fraction, and space- and temperature-dependent internal heat generation/absorption on the velocity field, induced magnetic field, and thermal field, as well as the skin friction coefficient and the local Nusselt number, for the nanoparticles *Cu*, *Ag*, and *TiO₂* when the base fluid is water. The Prandtl number is fixed at 6.2 (water), following Oztop *et al.* (2008).

Fig. 5.2 (a–c) shows the variation of the slip boundary layer, for various values of λ , for the velocity profile of *Cu*–water nanofluid. The slip boundary-layer profiles differ for $\lambda > 1$ and $\lambda < 1$. When $\lambda > 1$, the slip parameter α increases the momentum and induced magnetic field boundary-layer thicknesses, and subsequently, the velocity decreases; if $\lambda < 1$, then α enhances the energy boundary-layer thickness and consequently, the velocity increases. Fig. 5.2 (c) illustrates the effect of α on the nanofluid thermal field. The distributions of the slip boundary layer differ for $\lambda > 1$ and $\lambda < 1$. As the value of the slip parameter increases for $\lambda > 1$, the thickness of the thermal boundary layer grows, while for $\lambda < 1$, the surface experiences a drop in the heat transmission rate.



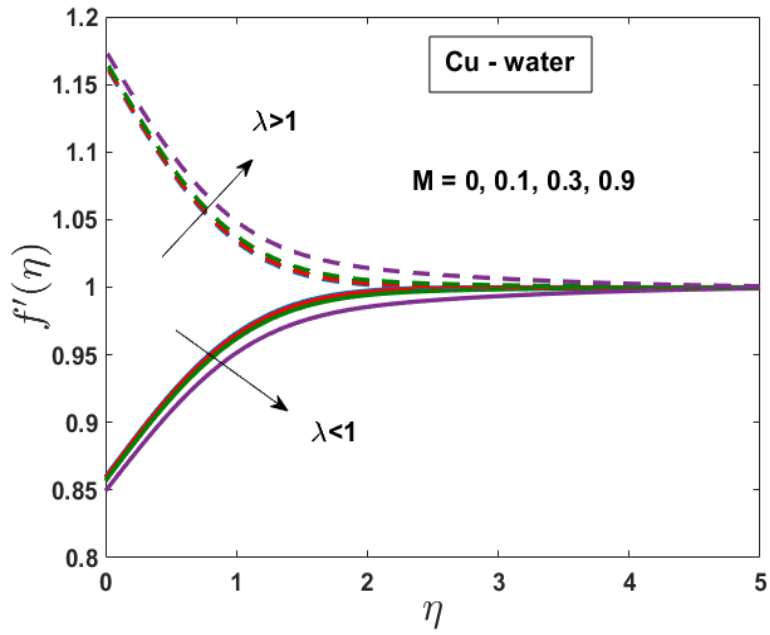
(a)

(b)

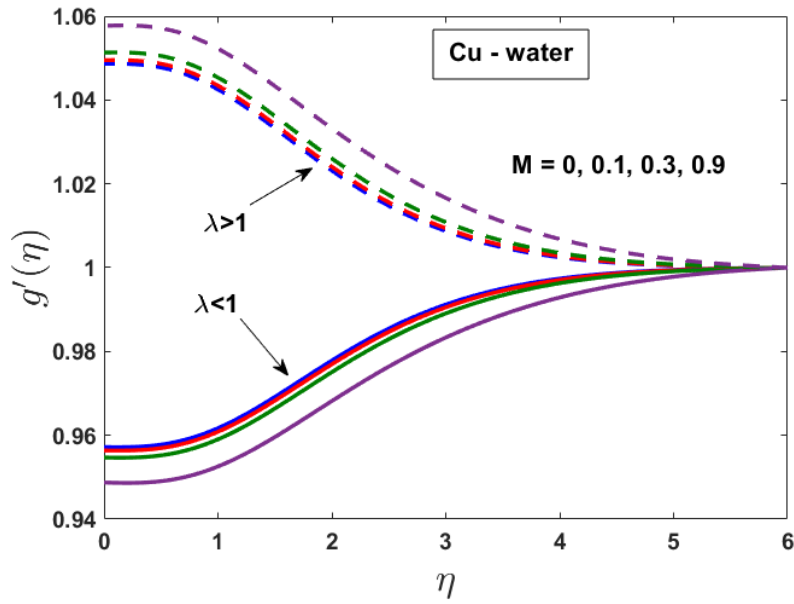


(c)

Fig. 5.2 Impact of slip parameter α for Cu-water on (a) velocity, (b) induced magnetic field, and (c) temperature



(a)



(b)

Fig. 5.3 Impact of magnetic Prandtl number Prm for Cu -water on (a) velocity and (b) induced magnetic field

The influence of the magnetic parameter, for various values of λ , on the velocity and magnetic stream function gradients are shown in Fig. 5.3 (a–b). The MHD boundary-layer profiles diverge for $\lambda > 1$ and $\lambda < 1$. It is apparent that the momentum boundary layers thicken as the value of M increases for $\lambda > 1$. The fluid receives a push from the magnetic field after first slowing down due to viscous force since it can be observed that the magnetic lines of forces flow past the plate towards wall velocity. Consequently, when the magnetic parameter M rises, the fluid's velocity reduces for $\lambda < 1$, as does the induced magnetic field profile, while the opposite trend is observed for $\lambda > 1$. Fig. 5.3 (b) depicts the effects of the magnetic parameter M on the induced magnetic field profile in the case of Cu -water nanofluid, for numerous values of λ . For $\lambda > 1$, increasing the value of M enhances the induced magnetic field. For $\lambda < 1$, the reverse trend is observed.

The effects of the reciprocal magnetic parameter χ on the induced magnetic field are illustrated in Fig. 5.4. The boundary-layer thickness grows as this parameter increases. Nanofluid with a larger χ value produces a higher magnetic diffusivity, which enhances the induced magnetic field on the fluid flow.

Figs. 5.5 and 5.6 demonstrate the influence of non-uniform space- and temperature-dependent internal heat generation or absorption parameters on the temperature profiles. The thermal boundary-layer thickness increases with the values of heat sources or sinks for all values of λ . In the case of heat sources ($A^* > 0$, Fig. 5.5) and ($B^* > 0$, Fig. 5.6), the boundary layer acquires energy, which leads to an increase in the temperature of the nanofluid. Due to the presence of nanoparticles, this rise in temperature causes an increase in the flow field. In the case of a heat sink ($A^* < 0$, Fig. 5.5) and ($B^* < 0$, Fig. 5.6), cooling the fluid has the reverse effect.

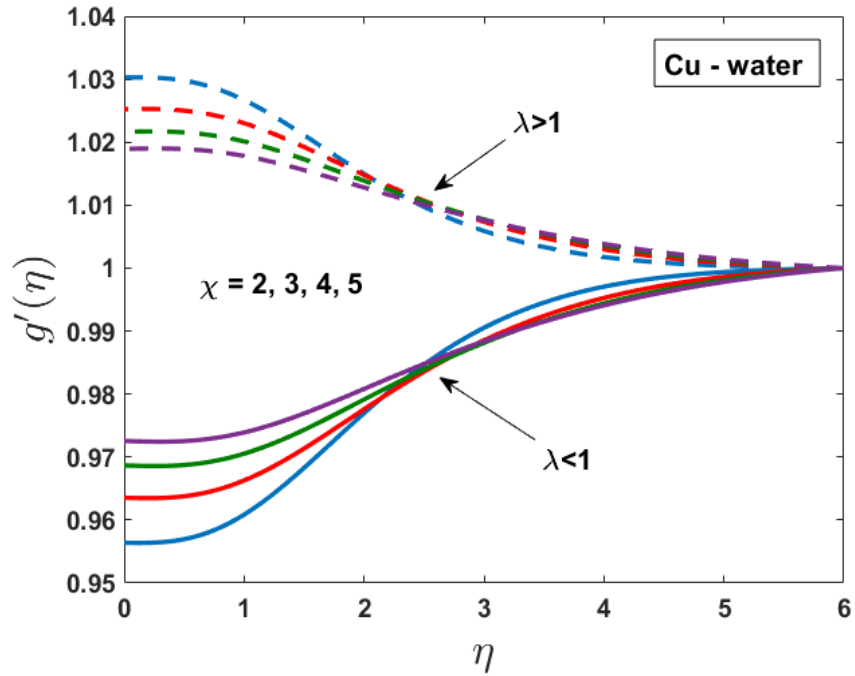


Fig. 5.4 Induced magnetic field for *Cu*-water nanofluid for different values of χ

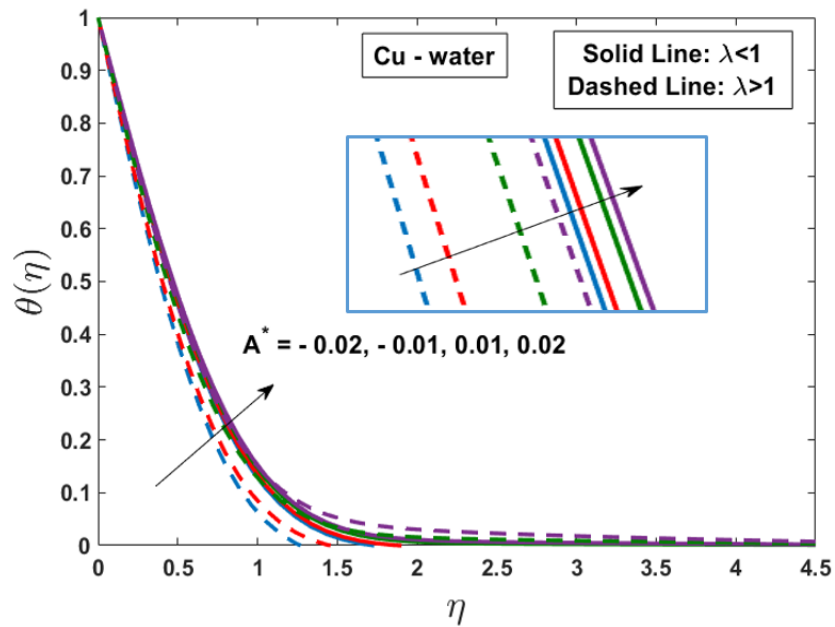


Fig. 5.5 Temperature distribution for *Cu*-water nanofluid for different values of A^*

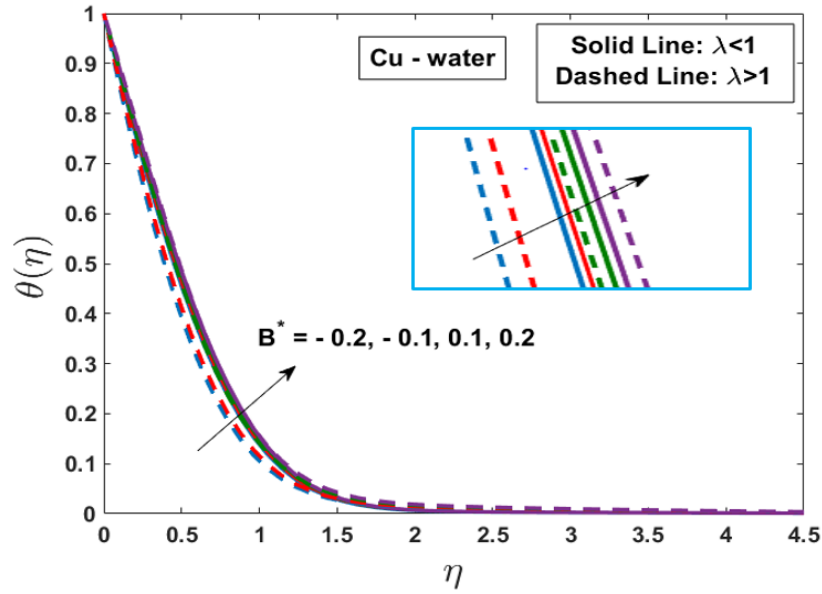


Fig. 5.6 Temperature distribution for *Cu*-water nanofluid for different values of B^*

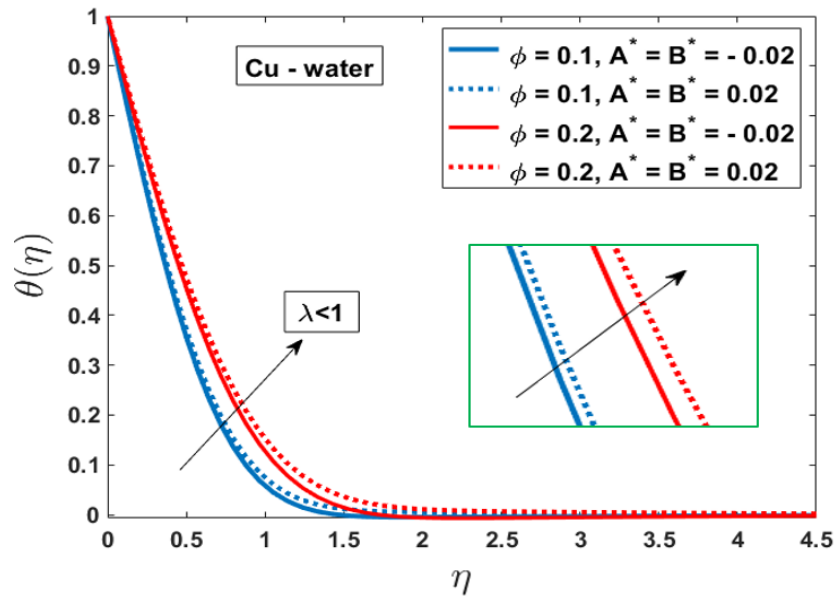


Fig. 5.7 Effect of ϕ on temperature profile with A^* and B^* for *Cu*-water nanofluid

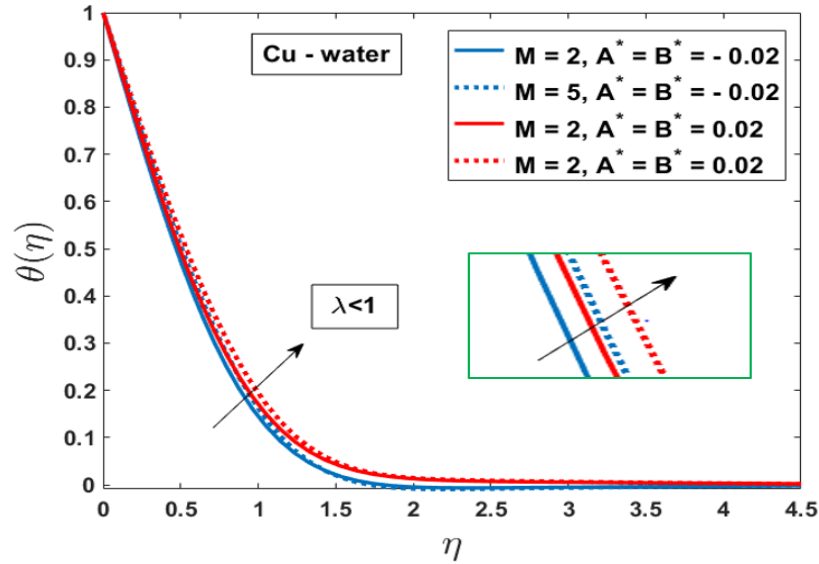


Fig. 5.8 Effect of M on temperature profile with A^* and B^* for Cu -water nanofluid

The impacts of the nanoparticle volume fraction ϕ and the magnetic parameter M on the thermal field, with non-uniform heat generation/absorption (A^*, B^*), are exhibited in Figs. 5.7 and 5.8. The change in the thermal boundary-layer thickness resembles the concentration of the nanoparticles. In the presence of a heat source/sink, the same value nanoparticle volume fraction ϕ has a different impact on temperature. In the case of a heat source ($A^* > 0, B^* > 0$), the temperature increases with ϕ due to the production of additional energy in the boundary layer. The cooling rate in conducting nanofluid is enhanced by the presence of a heat sink ($A^* < 0, B^* < 0$). The effect of a magnetic field on the thermal behaviour of nanofluid with a heat source/sink (A^*, B^*) is presented in Fig. 5.8. The nanofluid temperature rises when a magnetic field is present. The fluid warms as the value of the magnetic parameter M , grows. The temperature of the fluid changes according to the presence of a heat source/sink for identical values of the magnetic parameter.

Figs. 5.9–5.11 demonstrate how different nanoparticles affect the velocity, induced magnetic field, and temperature distributions of the nanofluid for various values of λ . The different nanofluids have distinct velocities; the titanium oxide nanofluid has a faster velocity and higher induced magnetic field profiles than the copper and silver nanofluids for $\lambda > 1$. The density of the nanoparticles determines the velocity field of the nanofluid. Compared to other materials, the silver–water nanofluid has a low velocity since silver has a far higher density than copper and

titanium dioxide. Conversely, when $\lambda < 1$, the opposite phenomenon is noted. The influence of the nanoparticles' thermal conductivity on the nanofluid thermal field is illustrated in Fig. 5.11. Nanofluids containing nanoparticles with a higher thermal conductivity have higher temperatures. It is evident from that for all values of λ , *Ag*-water has an elevated thermal field, whereas the thermal field is lower for *TiO₂*-water.

The fluctuations in the local skin friction coefficient and heat transfer rate depending on the magnetic parameter M are displayed in Figs. 5.12–5.15 for specific values of the nanoparticle volume parameter, with different nanoparticles, and in the cases of $\lambda > 1$ and $\lambda < 1$. The local skin friction appears to decrease with rising ϕ for large values of M for $\lambda < 1$, and *Ag*-water nanofluid exhibits a higher drag than *TiO₂*-water. When $\lambda > 1$, the opposite phenomenon is observed. Nanofluid with *TiO₂* particles has the highest reduced Nusselt number values, whereas *Ag*-water has the lowest. Consequently, *TiO₂*-water has a higher heat transfer rate than other materials at every possible value of λ .

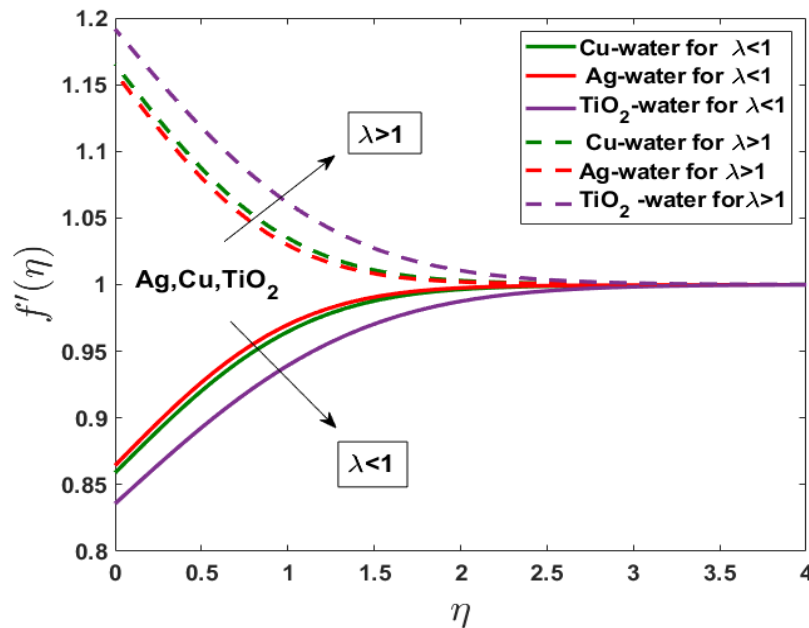


Fig. 5.9 Velocity distributions for different nanofluids

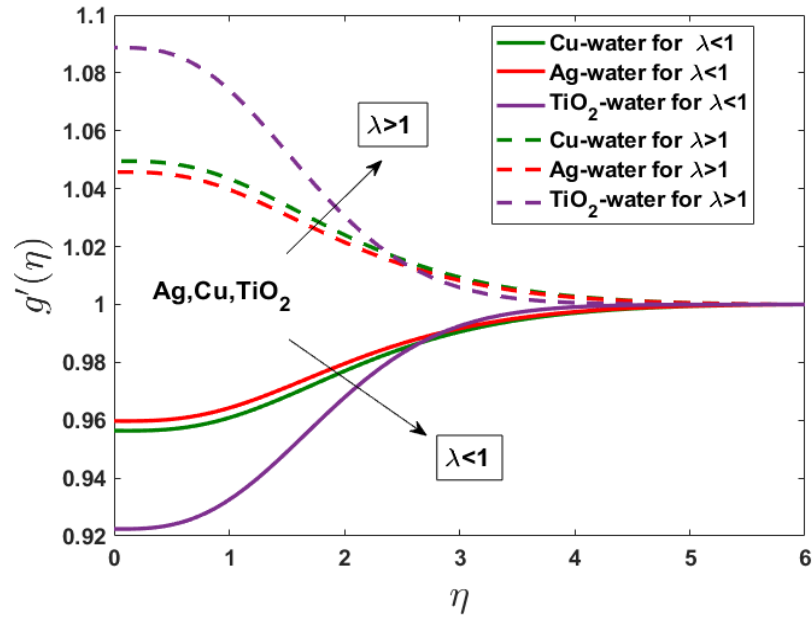


Fig. 5.10 Induced magnetic field distributions for different nanofluids

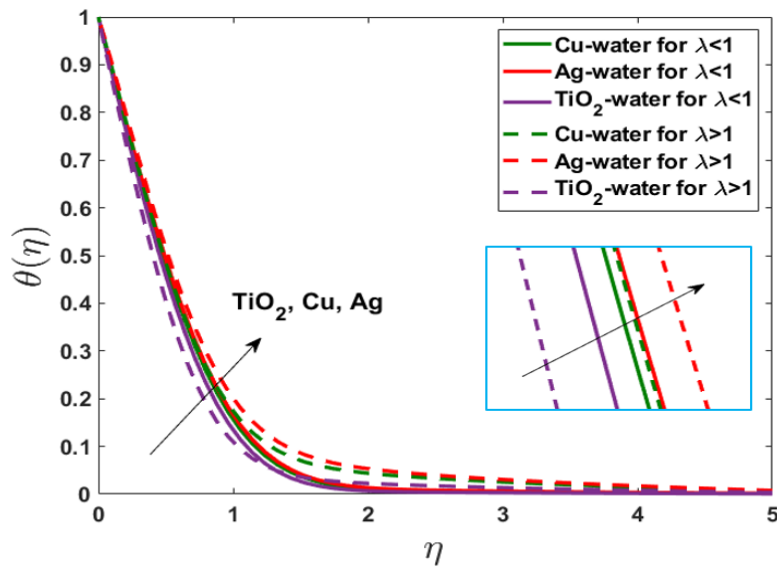


Fig. 5.11 Temperature distributions for different nanofluids

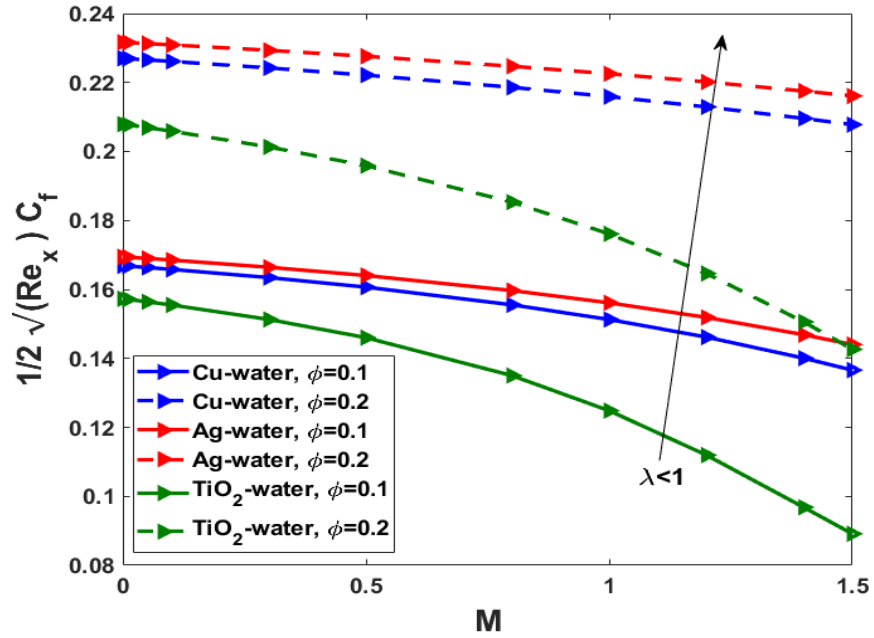


Fig. 5.12 Effects of ϕ and M on skin friction coefficient C_f when $\lambda < 1$

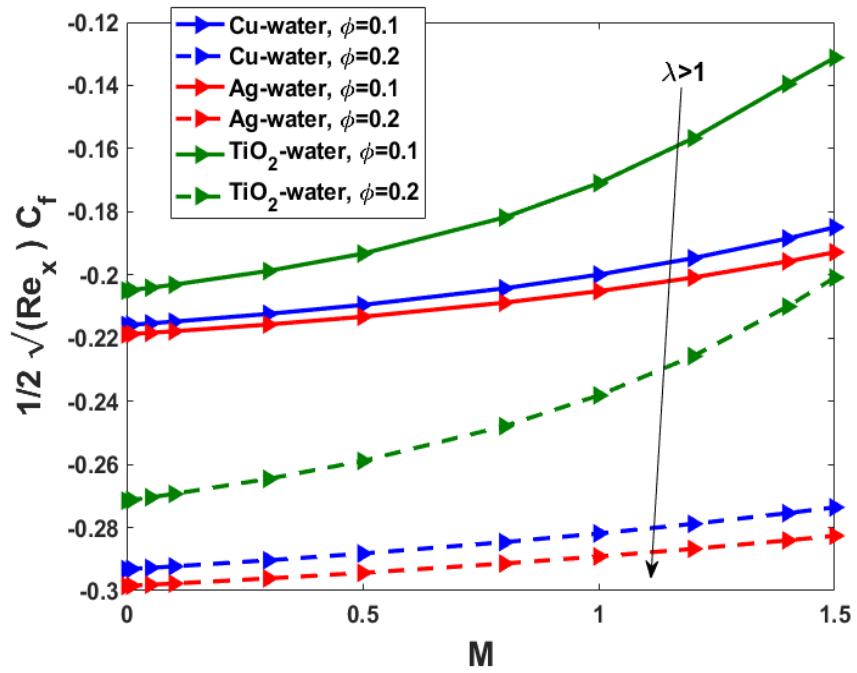


Fig. 5.13 Effects of ϕ and M on skin friction coefficient C_f when $\lambda > 1$

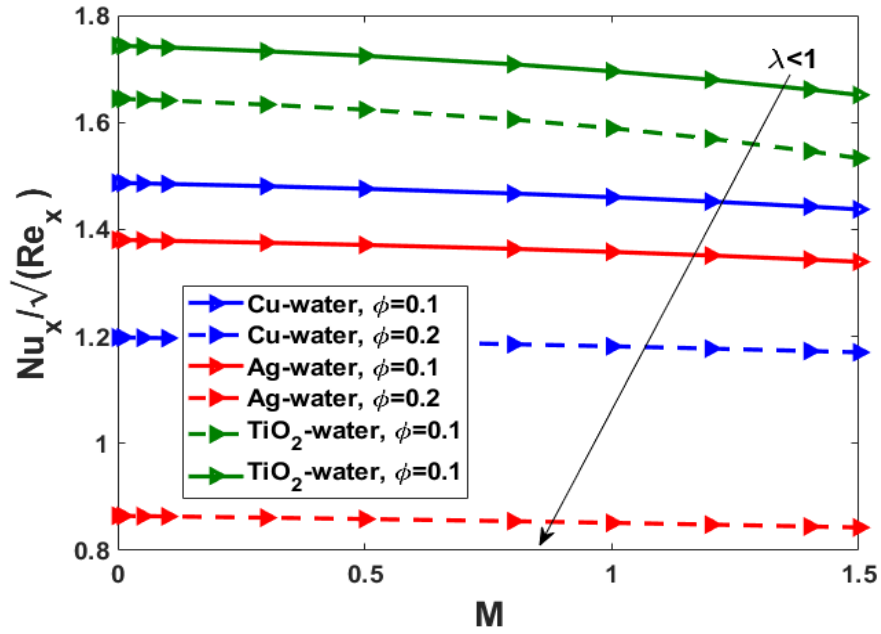


Fig. 5.14 Effects of ϕ and M on reduced Nusselt number Nu when $\lambda < 1$

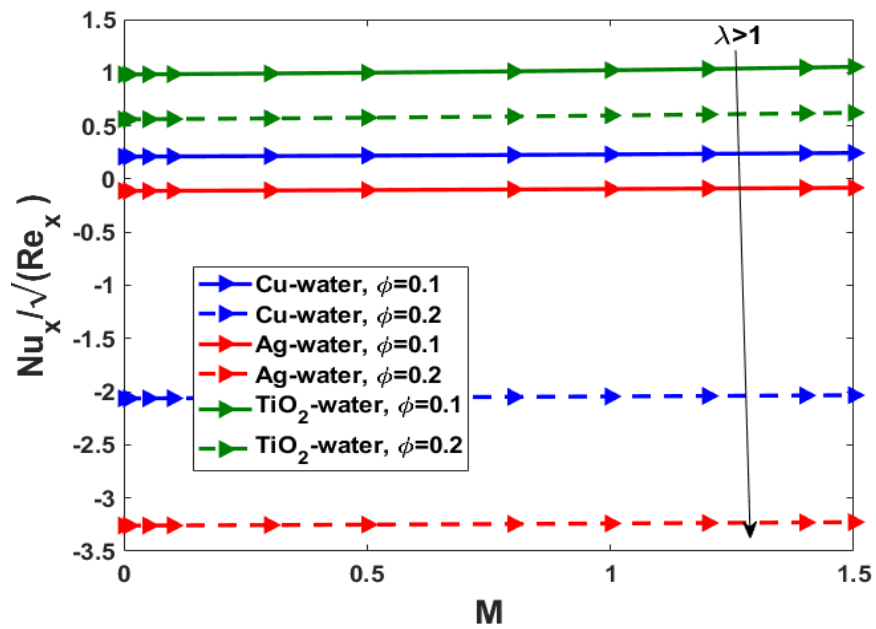


Fig. 5.15 Effects of ϕ and M on reduced Nusselt number Nu when $\lambda > 1$

5.4 Summary

This study has investigated the effects of space- and temperature-dependent internal heat generation/absorption on the boundary-layer flow of a water-based nanofluid, with different nanoparticles, past a moving surface under the combined impact of induced magnetic field and momentum slip condition. The consequences of the magnetic, slip, and velocity ratio parameters have been investigated. For different nanoparticles, the effects of magnetic parameter M , slip parameter α , reciprocal magnetic parameter χ , non-uniform heat generation/absorption (A^* , B^*), nanoparticle volume fraction ϕ , reduced Nusselt number, and local skin friction coefficient have been examined for various values of the velocity ratio parameter λ . The change in the skin friction coefficient and Nusselt number are higher for large values of ϕ with M . It was also observed that TiO_2 has thicker momentum, magnetic, and thermal boundary layers than Cu and Ag .

Chapter 6

Numerical Simulation for the Influence of Aligned-Field MHD Nanofluids on Heat Transfer over a Moving Flat Plate

This chapter examines the impacts of viscous dissipation on a convective aligned MHD flow of an incompressible, viscous, and electrically conducting water-based nanofluid across a semi-infinite moving flat surface, in which the flow velocity and magnetic field vectors far from the plate are parallel. The SRM technique is used to numerically solve the nonlinear coupled PDEs. To better understand how well external magnetic fields can regulate nanofluid and magnetic properties, a variety of different nanofluids are taken into consideration. The effects of various values of the incorporated parameters, namely the nanoparticle volume function ϕ , magnetic parameter M , magnetic Prandtl number Prm , and Eckert number Ec , on the motion, induced magnetic field, and heat transfer properties are investigated graphically and analysed in detail. The skin friction coefficient and heat transfer rate are also studied. Comparing the outcomes derived from the SRM and Maple shows strong agreement.

6.1 Mathematical Model with Flow Configuration

Consider a stable 2D MHD laminar free convective heat and mass transfer flow of nanofluid with consistent physical characteristics. This flow originates from a moving flat plate within a magnetic field aligned with the motion. Parallel to the plate, an induced magnetic field with intensity H_0 is applied and the velocity of the plate is $U_w = \epsilon U_\infty$, where ϵ is the velocity parameter. Fig. 6.1 shows a schematic illustration and the coordinate system. We also note that both the viscous dissipation and ohmic heating terms are considered in the energy equation. With these physical assumptions and taking a boundary-layer approach, the governing equations for conservation of mass, momentum, and thermal energy are expressed as follows:

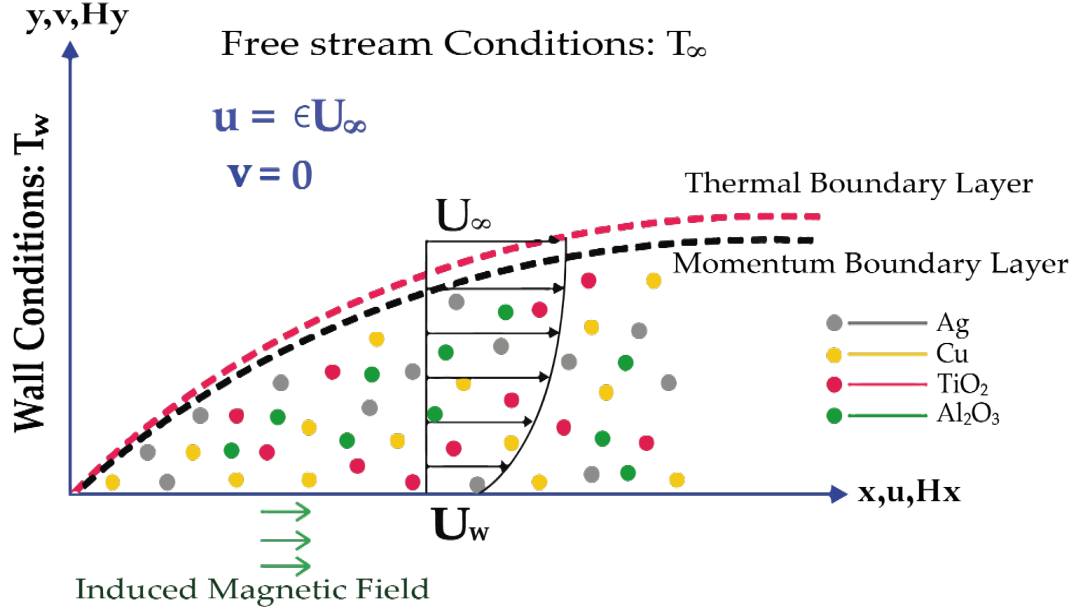


Fig. 6.1 Geometry of flat moving plate

Continuity:

$$\frac{\partial u}{\partial x} + \frac{\partial v}{\partial y} = 0 \quad (6.1)$$

$$\frac{\partial H_x}{\partial x} + \frac{\partial H_y}{\partial y} = 0 \quad (6.2)$$

Momentum:

$$u \frac{\partial u}{\partial x} + v \frac{\partial u}{\partial y} = \nu_{nf} \frac{\partial^2 u}{\partial y^2} + \frac{\mu_e}{\rho_{nf}} \left(H_x \frac{\partial H_x}{\partial x} + H_y \frac{\partial H_x}{\partial y} \right) \quad (6.3)$$

Induced magnetic field:

$$u \frac{\partial H_x}{\partial x} + v \frac{\partial H_x}{\partial y} = H_x \frac{\partial u}{\partial x} + H_y \frac{\partial u}{\partial y} + \frac{1}{\mu_e \sigma_{nf}} \frac{\partial^2 H_x}{\partial y^2} \quad (6.4)$$

Thermal energy:

$$u \frac{\partial T}{\partial x} + v \frac{\partial T}{\partial y} = \alpha_{nf} \frac{\partial^2 T}{\partial y^2} + \frac{\mu_{nf}}{(\rho C_p)_{nf}} \left(\frac{\partial u}{\partial y} \right)^2 + \frac{1}{\sigma_{nf} (\rho C_p)_{nf}} \left(\frac{\partial H_x}{\partial y} \right)^2 \quad (6.5)$$

The appropriate boundary conditions for the current study are described by

$$\left. \begin{aligned} u = \epsilon U_\infty, v = 0, \frac{\partial H_x}{\partial y} = H_y = 0, T = T_w \quad \text{At } y = 0 \\ u \rightarrow U_\infty, H_x \rightarrow H_0, T \rightarrow T_\infty \quad \text{At } y \rightarrow \infty \end{aligned} \right\} \quad (6.6)$$

The appropriate similarity transformations that convert the governing PDEs into ODEs are as follows:

$$\psi = (U_\infty \nu_f x)^{\frac{1}{2}} f(\eta), \quad \Phi = \left(\frac{\nu_f x}{U_\infty}\right)^{\frac{1}{2}} H_0 g(\eta), \quad \theta(\eta) = \frac{T - T_\infty}{T_w - T_\infty}, \quad \eta = \frac{y}{2} \left(\frac{U_\infty}{\nu_f x}\right)^{\frac{1}{2}} \quad (6.7)$$

Using (6.7) along with the boundary conditions (6.6), the governing equations (6.3)–(6.5) are transformed to the following non-dimensional form:

$$f''' + A f f'' - B M g g'' = 0 \quad (6.8)$$

$$g''' + C P r m (f g'' - g f'') = 0 \quad (6.9)$$

$$\frac{D}{P_r} \theta'' + E f \theta' + \frac{E c}{4B} (f'')^2 + \frac{M E c}{4C P r m} (g'')^2 = 0 \quad (6.10)$$

where

$$A = (1 - \phi)^{2.5} (1 - \phi + \phi \frac{\rho_s}{\rho_f})$$

$$B = (1 - \phi)^{2.5}$$

$$C = \frac{\sigma_{nf}}{\sigma_f} = 1 + \frac{3((\sigma_s/\sigma_f)-1)\phi}{((\sigma_s/\sigma_f)+2)-\phi((\sigma_s/\sigma_f)-1)}$$

$$D = \frac{k_{nf}}{k_f} = \frac{(k_s+2k_f)-2\phi(k_f-k_s)}{(k_s+2k_f)+2\phi(k_f-k_s)}$$

$$E = 1 - \phi + \phi \frac{(\rho c_p)_s}{(\rho c_p)_f}$$

The relevant converted boundary conditions are given by

$$\left. \begin{aligned} f(0) = 0, \quad f'(0) = 2\epsilon, \quad g(0) = g''(0) = 0, \quad \theta(0) = 1 \quad \text{as } \eta = 0 \\ f' \rightarrow 2, \quad g' \rightarrow 2, \quad \theta \rightarrow 0 \quad \text{as } \eta \rightarrow \infty \end{aligned} \right\} \quad (6.11)$$

In the above equations, $\epsilon = U_w/U_\infty$ represents the velocity ratio of the plate, $M = \mu_e H_0^2 / U_\infty^2 \rho_f$ is the magnetic parameter, $Pr = \nu_f (\rho C_p)_f / k_f$ is the Prandtl number, $Prm = \mu_e \nu_f \sigma_f$ is the magnetic Prandtl number, and $Ec = U_\infty^2 / \Delta T (C_p)_f$ is the Eckert number.

The physical quantities of interest are the skin friction coefficient C_f and the local Nusselt number Nu_x , defined by

$$C_f = \frac{\tau_w}{\rho_f U_\infty^2} \quad \text{and} \quad Nu_x = \frac{x q_w}{K_f (T_w - T_\infty)} \quad (6.12)$$

where τ_w is the surface shear stress or skin friction, and q_w is the heat flux from the plate; these are given by

$$\tau_w = \mu_{nf} \left(\frac{\partial u}{\partial y} \right)_{y=0} \quad \text{and} \quad q_w = -k_{nf} \left(\frac{\partial T}{\partial y} \right)_{y=0} \quad (6.13)$$

Substituting equation (6.7) into (6.12) and (6.13), the skin friction coefficient and the local Nusselt number are obtained as

$$\sqrt{Re_x} C_f = \frac{1}{4(1-\phi)^{2.5}} f''(0) \quad \text{and} \quad (Re_x/2)^{-1/2} Nu_x = -\frac{1}{2} a_4 \theta'(0) \quad (6.14)$$

where $Re_x = U_\infty x / \nu_f$ is the local Reynolds number.

The dynamic viscosity of the nanofluid, as given by Brinkman (1952), is

$$\mu_{nf} = \frac{\mu_f}{(1-\phi)^{2.5}}$$

where ϕ is the solid volume fraction of spherical nanoparticles. The effective density and heat capacitance of the nanofluid are defined as

$$\begin{aligned} \rho_{nf} &= (1-\phi)\rho_f + \phi\rho_s \\ (\rho C_p)_{nf} &= (1-\phi)(\rho C_p)_f + \phi(\rho C_p)_s \end{aligned}$$

The effective electrical conductivity of the nanofluid can be approximated, following Maxwell (1881), as

$$\frac{\sigma_{nf}}{\sigma_f} = 1 + \frac{3((\sigma_s/\sigma_f) - 1)\phi}{((\sigma_s/\sigma_f) + 2) - \phi((\sigma_s/\sigma_f) - 1)}$$

The effective thermal conductivity of the nanofluid is expressed by the Maxwell Garnett (1904) model as

$$\frac{k_{nf}}{k_f} = \frac{1 - \phi + 2\phi \frac{k_s}{k_s - k_f} \ln \frac{k_s + k_f}{2k_f}}{1 - \phi + 2\phi \frac{k_f}{k_s - k_f} \ln \frac{k_s + k_f}{2k_f}}$$

Taken from the work of Abu-Nada (2008), the thermophysical properties of the base fluid and the nanoparticles are provided in Table 6.1.

Table 6.1 Thermophysical characteristics of fluid and nanoparticles

Physical property	Base fluid (water)	<i>Cu</i>	<i>Ag</i>	<i>Al₂O₃</i>	<i>TiO₂</i>
C_p (J/kg · K)	4,179	385	235	765	686.2
ρ (Kg/m ³)	997.1	8,933	10,500	3970	4250
k (W/m · K)	0.613	401	429	40	8.9538
σ (S/m)	0.05	5.96×10^7	3.6×10^7	3.5×10^7	2.6×10^6

6.2 Solution procedure with the Spectral Relaxation Method Scheme

The SRM iteration scheme can be described as follows:

$$F''_{r+1} + Af_r F'_{r+1} - BMg_r G'_r = 0 \quad (6.15)$$

$$f'_{r+1} = F_{r+1} \quad (6.16)$$

$$G''_{r+1} + CPrm(f_{r+1}G'_{r+1} - g_r F'_{r+1}) = 0 \quad (6.17)$$

$$g'_{r+1} = G_{r+1} \quad (6.18)$$

$$\frac{D}{Pr} \theta''_{r+1} + E f_{r+1} \theta'_{r+1} + \frac{Ec}{4B} (F'_{r+1})^2 + \frac{MEc}{4CPrm} (G_{r+1}')^2 = 0 \quad (6.19)$$

subject to the boundary conditions

$$F_{r+1}(0) = 2\epsilon, F_{r+1}(\infty) = 2 \quad (6.20)$$

$$f_{r+1}(0) = 0 \quad (6.21)$$

$$G'_{r+1}(0) = 0, G'_{r+1}(\infty) = 2 \quad (6.22)$$

$$g_{r+1}(0) = 0 \quad (6.23)$$

$$\theta_{r+1}(0) = 1, \theta_{r+1}(\infty) = 0 \quad (6.24)$$

The Chebyshev spectral collocation method is used to discretize the linear PDEs (6.8)–(6.10).

Applying the Chebyshev pseudo-spectral approach to equations (6.15) to (6.24) yields

$$A_1 F_{r+1} = B_1, \quad F_{r+1}(\xi_N) = 2, F_{r+1}(\xi_0) = 2\epsilon \quad (6.25)$$

$$A_2 f_{r+1} = B_2, \quad f_{r+1}(\xi_N) = 0 \quad (6.26)$$

$$A_3 G_{r+1} = B_3, \quad G_{r+1}(\xi_N) = 2, G'_{r+1}(\xi_0) = 0 \quad (6.27)$$

$$A_4 g_{r+1} = B_4, \quad g_{r+1}(\xi_N) = 0 \quad (6.28)$$

$$A_5 \theta_{r+1} = B_5, \quad \theta_{r+1}(\xi_N) = 0, \theta'_{r+1}(\xi_0) = 1 \quad (6.29)$$

where

$$A_1 = D^2 + \text{diag}(f_r)D, \quad B_1 = BMg_r G'_r \quad (6.30)$$

$$A_2 = D, \quad B_2 = F_{r+1} \quad (6.31)$$

$$A_3 = D^2 + \text{diag}(CPrm f_{r+1})D, \quad B_3 = CPrm g_r F'_{r+1} \quad (6.32)$$

$$A_4 = D, \quad B_4 = G_{r+1} \quad (6.33)$$

$$A_5 = \text{diag} \left(\frac{D}{Pr} \right) D^2 + \text{diag}(E f_{r+1}) D, \quad B_5 = -\frac{Ec}{4B} (F'_{r+1})^2 - \frac{MEc}{4CPrm} (G_{r+1}')^2 \quad (6.34)$$

Here, $\text{diag} []$ denotes a diagonal matrix of size $(N + 1) \times (N + 1)$, where N is the number of grid points and $f_r(\eta)$, $g_r(\eta)$, and $\theta_r(\eta)$ are the values of the functions f , g , and θ , respectively, when calculated at the grid points, and the subscript r is the number of iterations. The spectral collocation approach can be used to solve equations (6.25) to (6.34), which make up the SRM scheme, beginning with the initial conditions listed below, which are selected to fulfil the boundary constraints:

$$f_0(\eta) = 1 + 2\epsilon\eta - e^{-\eta}, \quad g_0(\eta) = 2\eta - (2 + \eta)e^{-\eta}, \quad \theta_0(\eta) = e^{-\eta} \quad (6.35)$$

6.3 Computational Results and Physical Interpretation

Numerical computations for the solution of the system of ODEs (6.8)–(6.10) with associated boundary constraints (6.11) are carried out using the SRM. The results are attained using $\bar{N} = 60$ grid points, and the infinity value η_∞ is taken as 15. To evaluate the accuracy and convergence of the SRM method, Table 6.2 compares the outcomes with numerical methods reported to be correct within a specified number of decimal digits. The numerical simulations for dimensionless velocity, temperature, skin friction, Nusselt numbers, and streamlines under the impact of the flow parameters are presented in this section and are displayed in Figs. 6.2–6.12. Figs. 6.2–6.6 present the results for an Al_2O_3 –water nanofluid.

Table 6.2 Comparison of $-\theta'(0)$ values for various values of Ec when $\epsilon = 0.1$, $Pr = 6.2$, $Prm = 0.1$, $M = 0.5$, and $\phi = 0$

Ec	SRM value	Maple value
–0.01	1.37696704	1.37552829551420052
0.01	1.35935417	1.35838992707996642
0.03	1.34174131	1.34125155862905387
0.05	1.32412844	1.32411319017906837

Fig. 6.2 (a–c) illustrates the influence of the velocity ratio parameter ϵ on the velocity, induced magnetic field, and thermal field, respectively. An increase in ϵ raises the speed and induced magnetic field profiles while reducing the temperature profile. The thickness of the thermal boundary layer decreases as the value of the plate velocity parameter ($\epsilon > 0$) rises, as seen in Fig. 6.2 (a–b). This is because an increase in ϵ causes the ratio of the plate velocity to the fluid velocity to increase. The fluid may circulate through the area more quickly due to the velocity differential, which reduces the thickness of the thermal boundary layer.

The effects of the applied magnetic field are depicted in Fig. 6.3 (a–c) for the nanofluid flow. The variable M , the reciprocal of the electromagnetic to the viscous force ratio, is the magnetic field parameter. It measures the intensity of the applied magnetic field. Fig. 6.3 (a–b) demonstrates that as M increases, the thickness of the momentum boundary layer decreases. An opposite force, the Lorentz force, is induced when a magnetic field affects an electrically conducting viscoelastic fluid. This force tends to reduce fluid flow in the boundary-layer region. Additionally, the fluid is slowed down by the viscous action. The magnetic field exerts a force on the fluid, which counteracts the effects of the viscous action that was dragging it down.

Fig. 6.3 (c) demonstrates that the temperature profile rises with M . It becomes apparent that viscous heating causes the temperature to rise; this effect is more pronounced when a magnetic field is present. A resistive force, the Lorentz force, is produced when a transverse magnetic field is applied to an electrically conducting fluid. The outcome is consistent with the idea that the magnetic field retards the free convection flow in the boundary layer and raises its temperature.

Fig. 6.4 (a–c) illustrates how the volumetric fraction of the nanoparticle affects the velocity, magnetic stream function gradient, and temperature field. It is evident that increasing the volume fraction causes the momentum and induced magnetic boundary-layer thicknesses to decrease, whereas thermal profiles show the opposite effect. With a rise in nanoparticle volume fraction in the range of $0 < \phi < 0.2$, there is an ongoing expansion in the thermal boundary layer. According to physical behaviour, the thickness of the boundary layer also increases when the thermal conductivity of the nanofluid and the volume fraction of the nanoparticles rise. The thermal conductivity of the nanofluid is enhanced with a corresponding rise in the volume fraction of the nanoparticles. Higher thermal diffusivity values and higher thermal conductivity values are frequently present. The temperature gradients are significantly reduced due to the high thermal

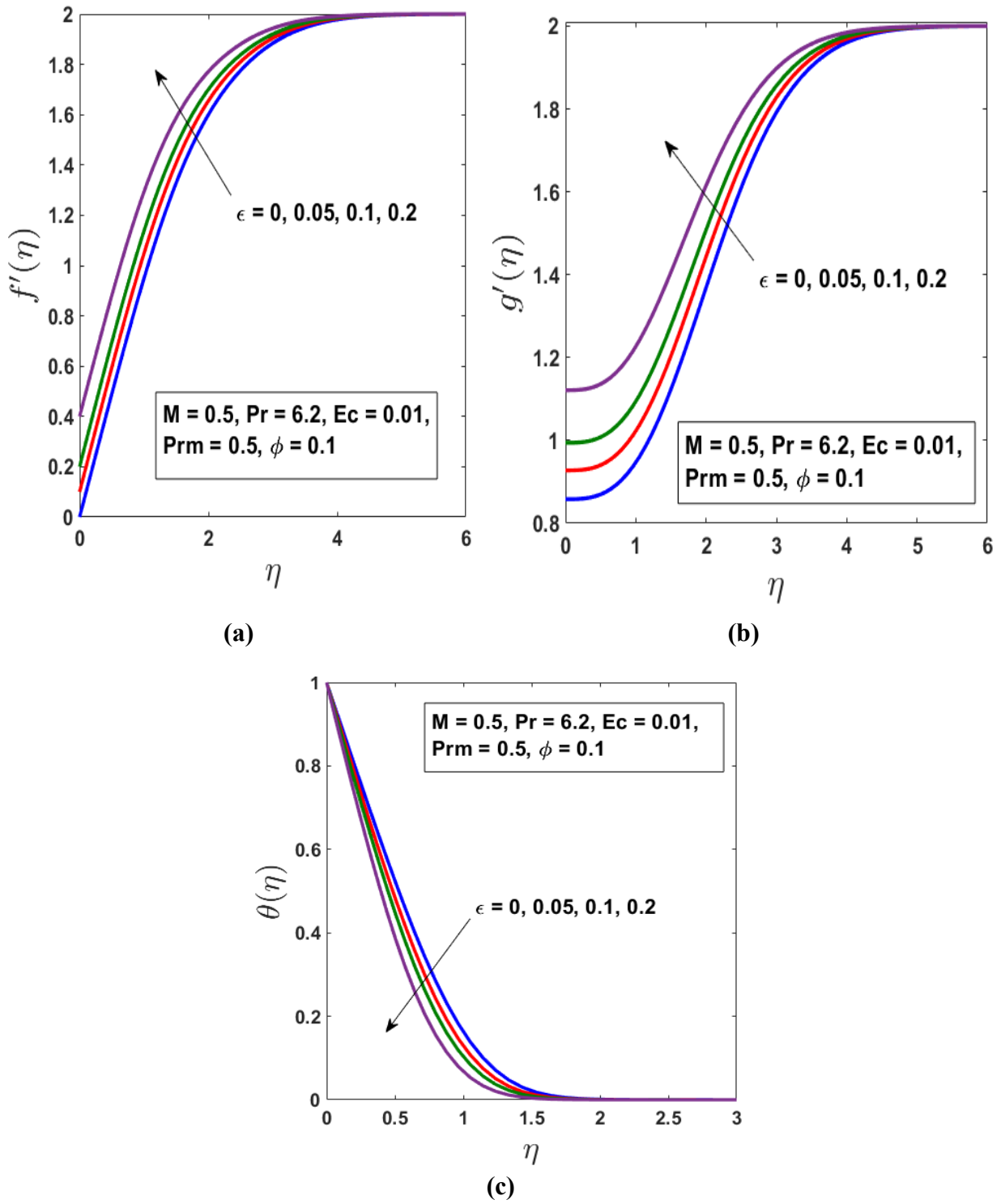


Fig. 6.2 Impact of velocity ratio parameter ϵ on (a) velocity, (b) induced magnetic field, and (c) temperature

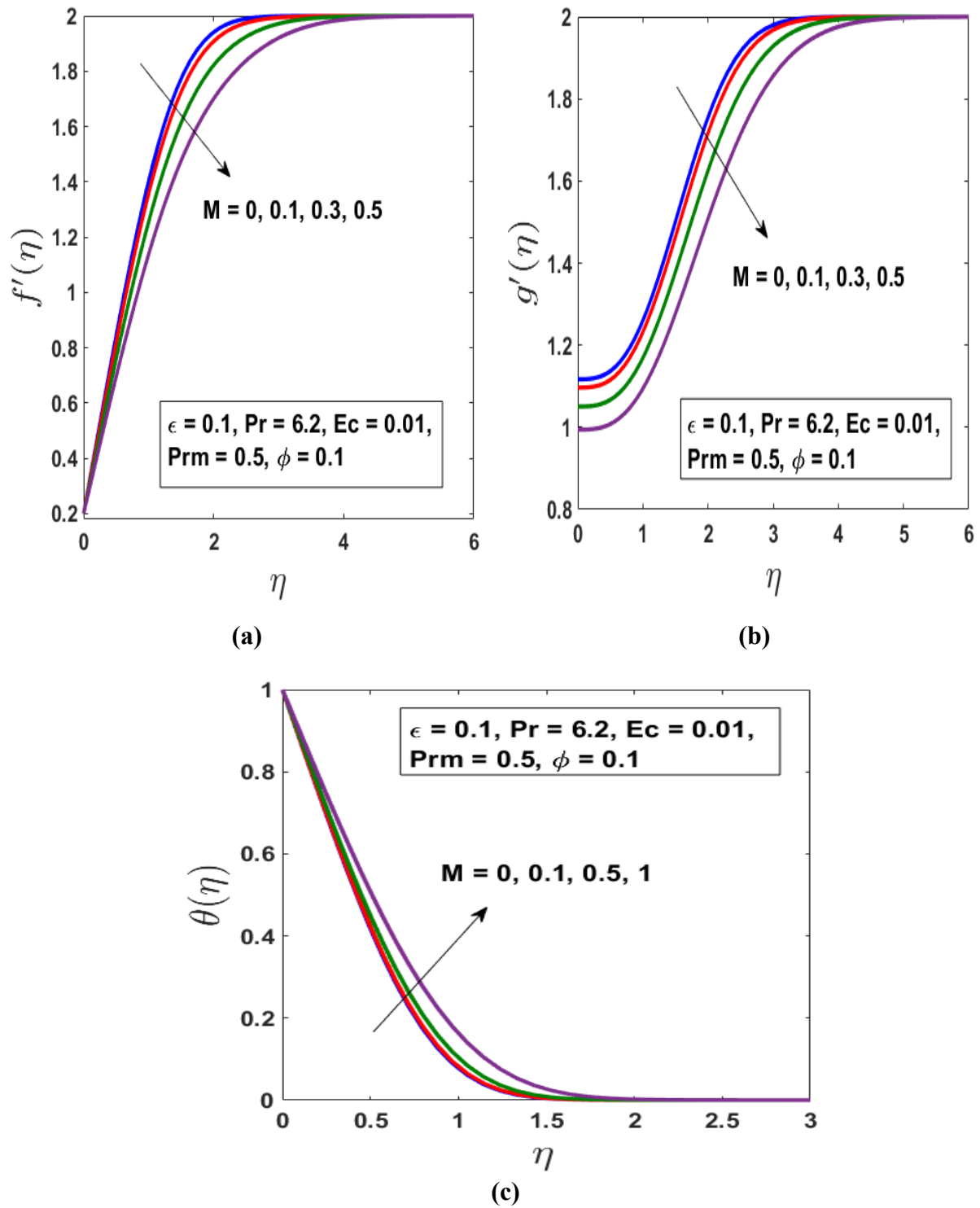


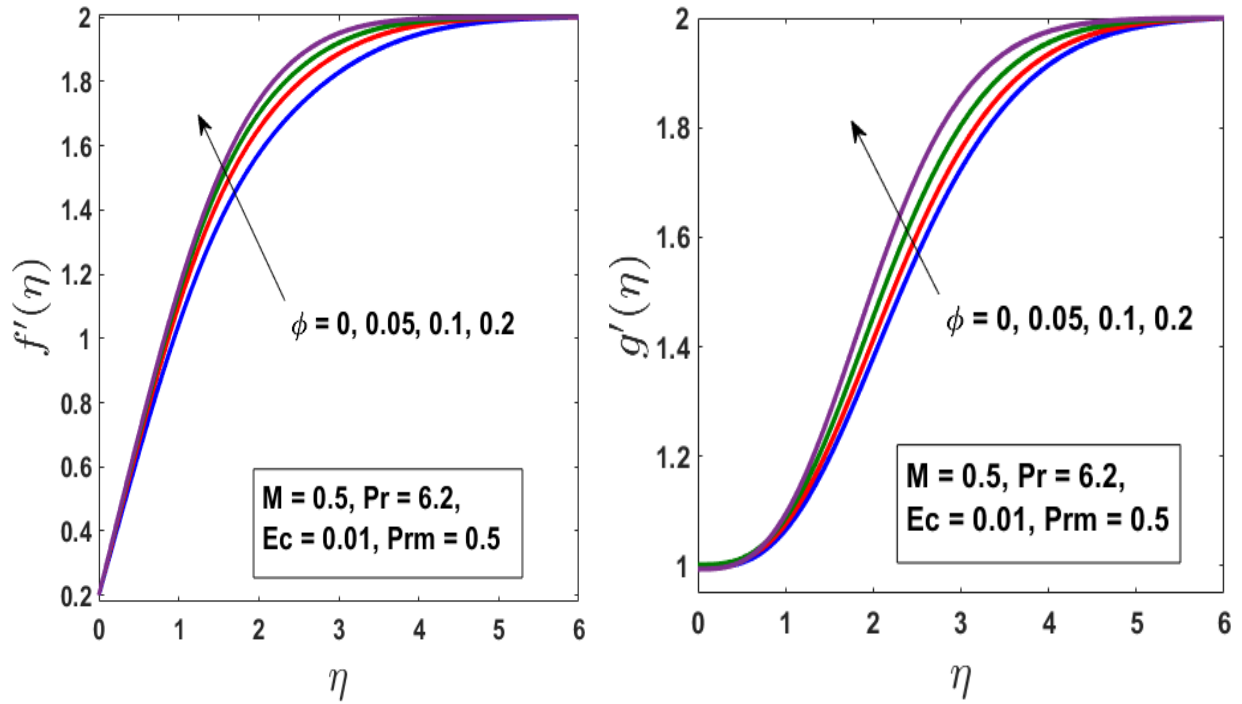
Fig. 6.3 Impact of magnetic parameter M on (a) velocity, (b) induced magnetic field, and (c) temperature

diffusivity. An increase in the nanoparticle volume fraction increases the thermal conductivity and boundary-layer thickness. The form, size, volume percentage, and substance of the nanoparticles can be adjusted to optimize the heat transfer process across the fluid volume. The convective heat transfer technique for nanofluids depends on thermal conductivity and other factors, including density, specific heat, and dynamic viscosity. Furthermore, it is apparent that combining these two improvement methods allows a substantially higher heat transfer rate.

The impact of the magnetic Prandtl number Prm on the velocity and the induced magnetic field profiles is apparent in Fig. 6.5 (a–b). The thickness of the boundary layer expands as this parameter grows. This occurs because nanofluids with larger Prm numbers produce higher magnetic diffusivities, which increase the induced magnetic field on the fluid flow.

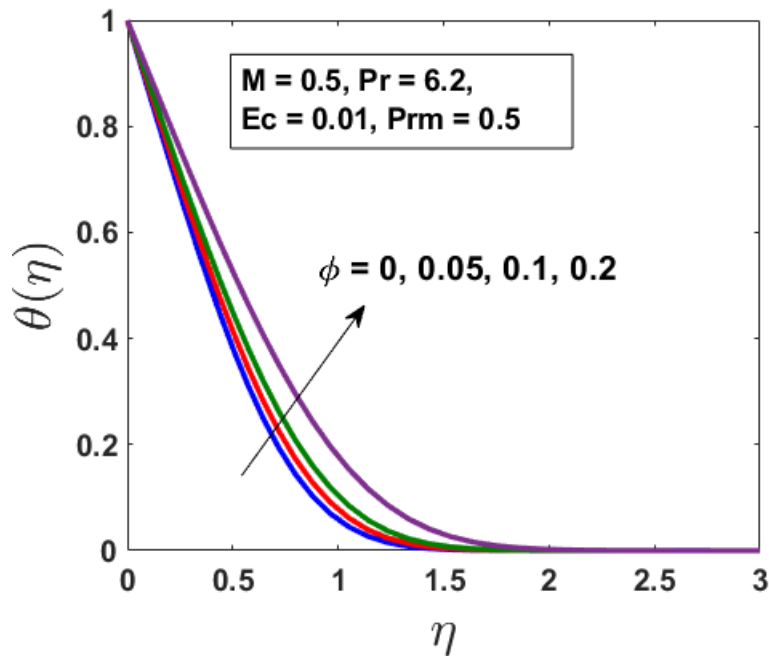
Fig. 6.6 demonstrates how the Eckert number Ec affects the temperature profile. It is observed that an increase in the Eckert number magnifies the temperature profile, and enhances the thermal boundary-layer thickness by improving the temperature dispersion in the vicinity of the boundary layer. Because of frictional heating, which results from viscous dissipation, thermal energy is stored in the fluid. The fluid's temperature increases monotonically with Ec . The ohmic heating effect raises the fluid's temperature and, as a result, reduces the surface temperature gradient.

The impact of different nanoparticles on the nanofluid's velocity, induced magnetic field, and temperature is shown in Fig. 6.7 (a–c). It is evident that different nanofluids move at different speeds, with Al_2O_3 nanofluids move faster than those of Cu , Ag , and TiO_2 . The density of the nanoparticles affects how quickly a fluid moves. In comparison to others, the silver–water nanofluid has a modest speed. This occurs due to the higher density of silver than copper, aluminium oxide, or titanium dioxide. Fig. 6.7 (c) provides a concise overview of the impact of nanoparticles on the thermal field when water is the base fluid. This figure depicts the influence of the nanoparticles' thermal conductivity on the nanofluid's thermal field. Nanofluids with high thermal conductivity have a greater temperature than those with low-thermal-conductivity nanoparticles. It is evident from Fig. 6.7 (c) that Ag –water has a stronger thermal field.



(a)

(b)



(c)

Fig. 6.4 Impact of volume fraction parameter ϕ on (a) velocity, (b) induced magnetic field, and (c) temperature

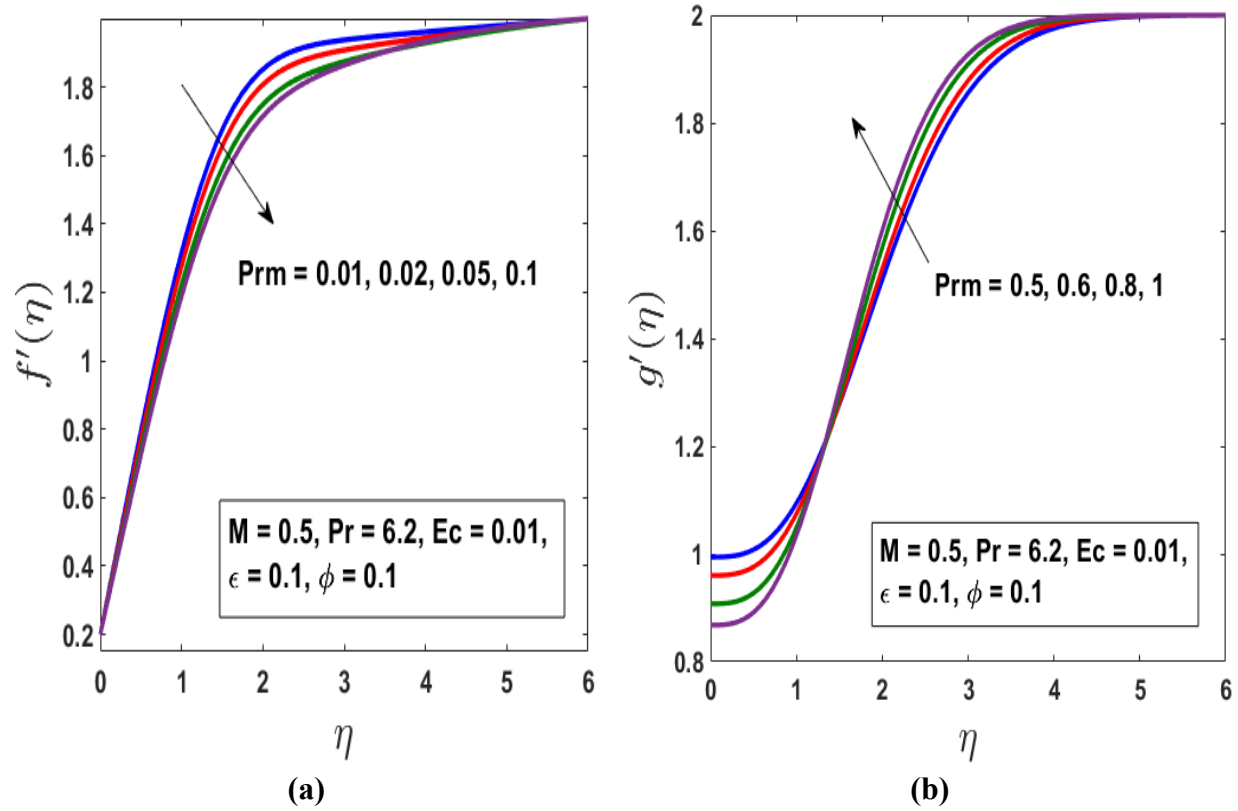


Fig. 6.5 Impact of Prm on (a) velocity and (b) induced magnetic field

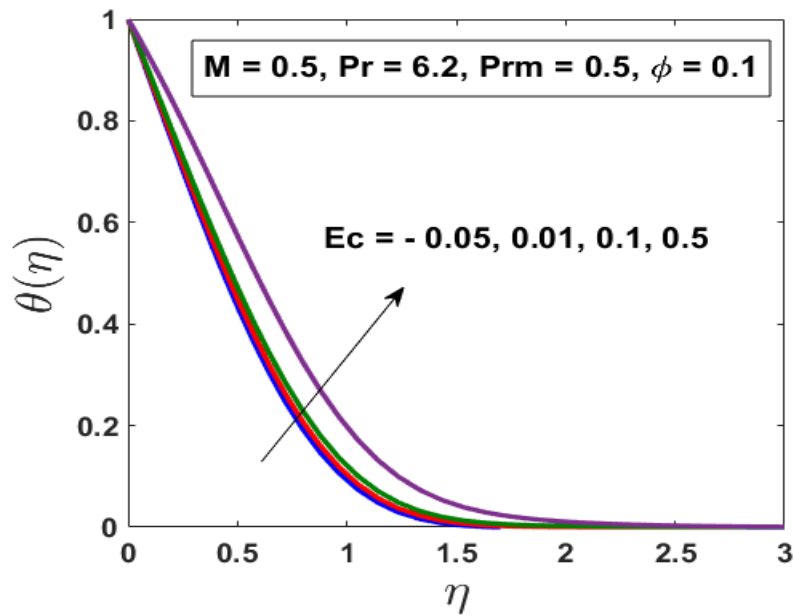
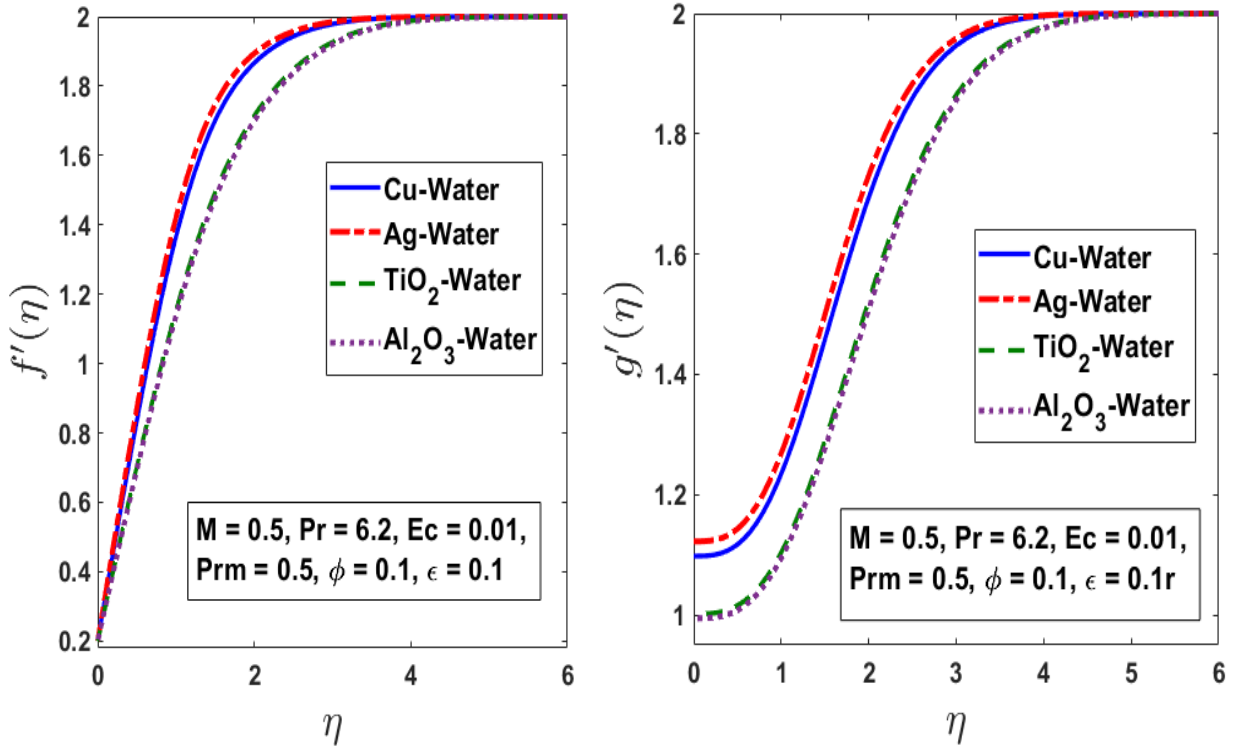
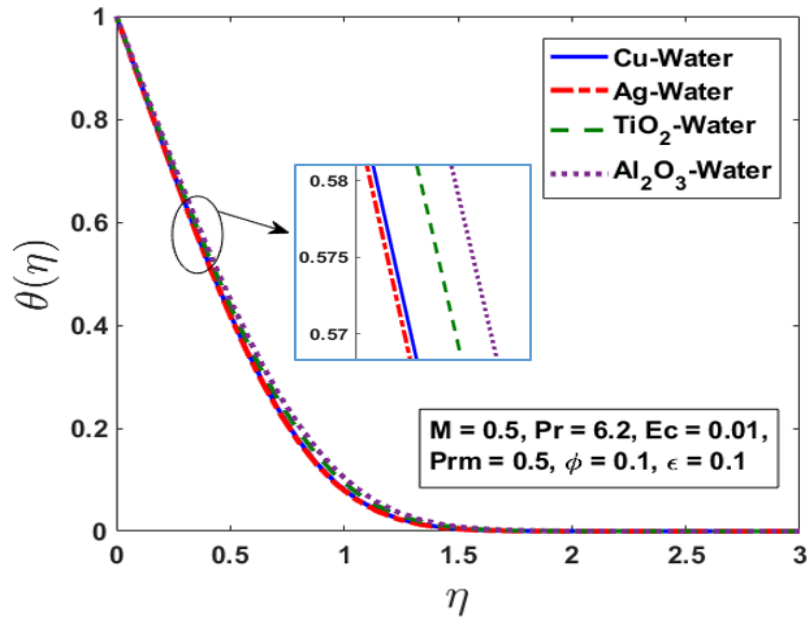


Fig. 6.6 Temperature distributions for different values of Eckert number Ec



(a)

(b)



(c)

Fig. 6.7 (a) Velocity, (b) induced magnetic field, and (c) temperature distributions for different nanofluids

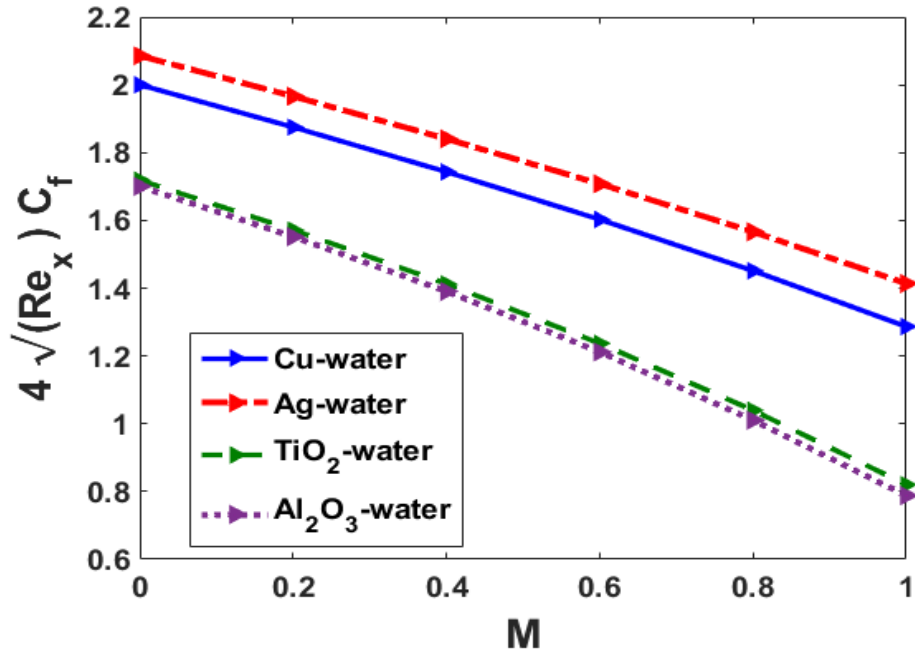


Fig. 6.8 Impact of M on skin friction for different nanofluids

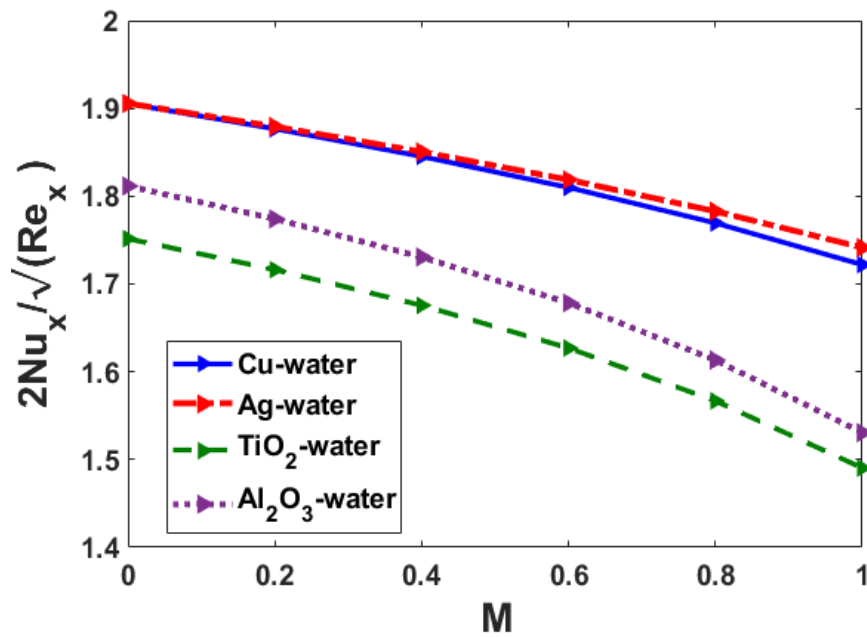


Fig. 6.9 Impact of M on Nusselt number for different nanofluids

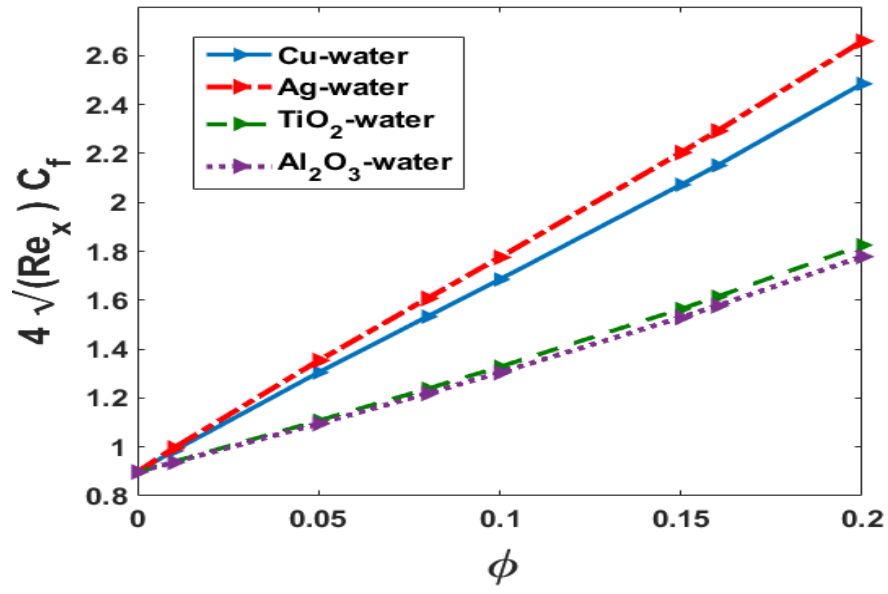


Fig. 6.10 Impact of ϕ on skin friction for different nanofluids

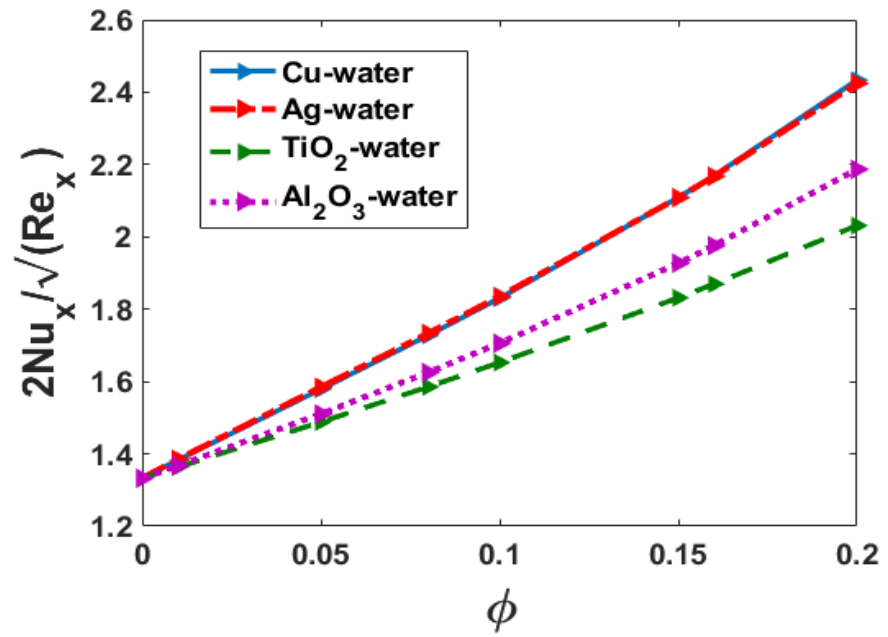


Fig. 6.11 Impact of ϕ on Nusselt number for different nanofluids

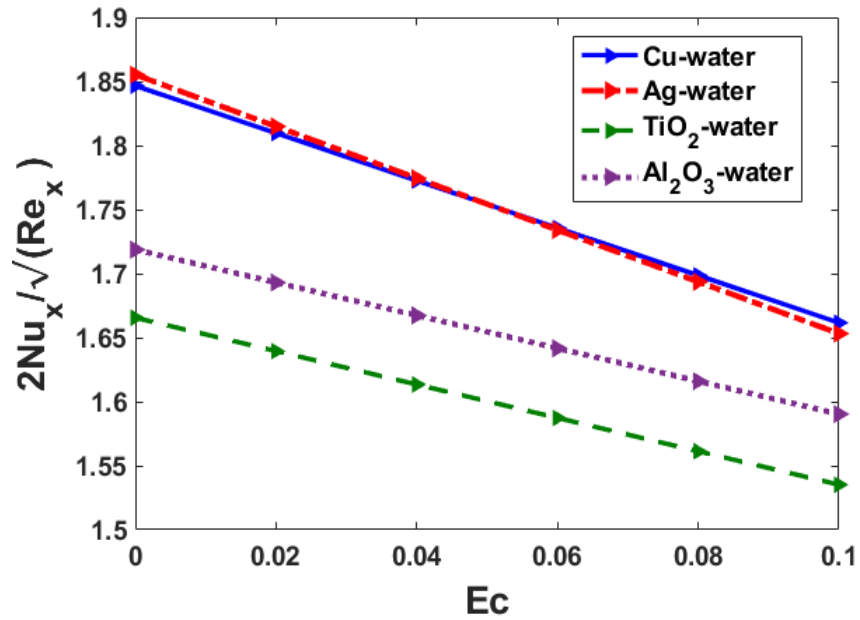


Fig. 6.12 Impact of Ec on Nusselt number for different nanofluids

Figs. 6.8 and 6.9 confirm the impact of the magnetic field parameter on the skin friction coefficient and heat transfer rate for various nanoparticles. These plots demonstrate how the magnetic field parameter enhances the wall's shear stress and maximizes the heat transmission rate as the magnetic parameter reduces due to the Lorentz force. *Ag*-water nanofluids exhibit higher drag and have the highest heat transfer enhancement than.

Figs. 6.10 and 6.11 show how the skin friction coefficient and the mean Nusselt number vary with volume fraction for various nanoparticles. The plots indicate that skin friction and heat transmission rise nearly monotonically with increasing volume fractions for all nanofluids. Nanofluids with *Ag* particles exhibit higher drag than those with the other three nanoparticles. This happens because silver has a higher density than copper, aluminium oxide, or titanium dioxide. The greatest heat transfer is observed for *Cu* nanofluids. Due to their high thermal diffusivity, copper nanoparticles reduce temperature gradients, impacting their performance. Since *TiO₂* has a lower thermal conductivity than *Ag*, *Cu*, and *Al₂O₃*, it has the lowest heat transfer due to the dominance of the conduction mode of heat transfer. The contribution of the convection mode grows as the volume fraction of nanoparticles rises, and the differences in mean Nusselt number increase. The variation of heat transfer rate with Eckert number Ec for various nanoparticles is

outlined in Fig. 6.12. It is noticeable that when the Eckert number rises, the Nusselt number drops, and that TiO_2 -water nanofluid has the lowest cooling rate.

6.4 Summary

External magnetic fields are exceptionally efficient in managing nanofluids' flow and heat transfer characteristics and their thermal and physical properties. The strength of the applied magnetic field influences the thermal conductivity of nanofluids. With this motivation, a water-based nanofluid with different nanoparticles was investigated numerically for an unstable aligned MHD boundary layer that flows across a moving surface, focusing on the impact of the induced magnetic field. The effects of the velocity ratio ϵ , magnetic parameter M , nanoparticle volumetric parameter ϕ , Eckert number Ec , and magnetic Prandtl number Prm on the momentum and thermal properties (including the coefficient of skin dragging and the energy gradient) have been thoroughly investigated. The temperature field is improved when the Eckert number and the viscous dissipation parameter have higher values. To solve the governing equations and investigate heat and fluid flow in nanofluids, we assumed the nanofluid to be homogeneous. The results demonstrated that the model is sufficiently reliable to accurately describe the thermal and hydrodynamic consequences of a nanofluid.

Chapter 7

Slip Effects and Heat Transfer of MHD Ferrofluid Flow across a Moving Flat Plate by Spectral Relaxation Simulation

This chapter examines the MHD heat transfer flow characteristics of an incompressible ferrofluid. The investigation focuses on the effects of slip over a mobile flat plate, incorporating the influence of an induced magnetic field and uniform heat flux. The physical scenario explored involves water as the base fluid with the incorporation of three diverse types of magnetic nanoparticles: Fe_3O_4 , $CoFe_2O_4$, and $Mn-ZnFe_2O_4$. Using a similarity transformation, the governing nonlinear PDEs are converted into a system of ODEs and then solved numerically, employing the SRM. The study explores the impact of different ferroparticles on the dimensionless velocity, temperature, skin friction, and Nusselt number by examining the effects of moving parameters, the slip parameter, and magnetic parameters. The analysis is presented with tables and plots, with comprehensive descriptions provided for each pertinent physical parameter.

7.1 Mathematical Formulation

Consider a steady two-dimensional forced convection MHD boundary-layer flow and heat transfer with magnetic nanoparticles over a moving horizontal flat plate in a variable magnetic field, as shown schematically in Fig. 7.1. The plate is immersed in a water-based ferrofluid, and it is assumed that the base fluid and nanoparticles are in thermal equilibrium. The flow is driven by a moving surface with velocity $u_w = \lambda U_\infty + u_{slip}$, where the hydrodynamic slip u_{slip} is considered at the fluid–solid interface and λ is a dimensionless quantity with $\lambda > 0$ for a surface moving away from the origin and $\lambda < 0$ for a surface moving towards the origin. The uniform heat flux from the surface is denoted by q_w . The energy equation includes both viscous dissipation and ohmic heating.

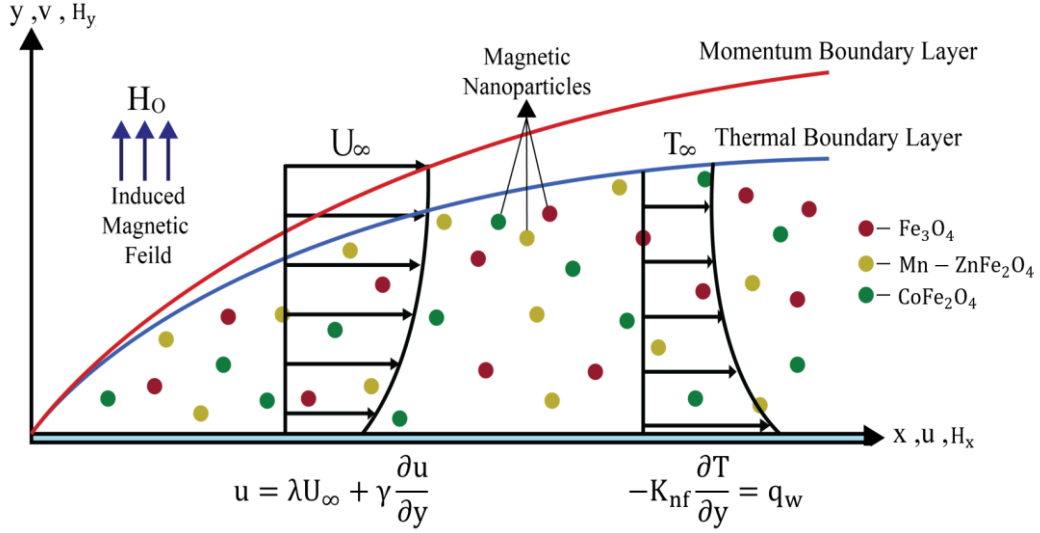


Fig. 7.1 Diagram illustrating the ferrofluid boundary-layer flow over a flat plate

Considering the boundary-layer approximations, following Khan *et al.* (2015), the governing equations for the flow and heat transfer are represented as follows:

Continuity:

$$\frac{\partial u}{\partial x} + \frac{\partial v}{\partial y} = 0 \quad (7.1)$$

$$\frac{\partial H_x}{\partial x} + \frac{\partial H_y}{\partial y} = 0 \quad (7.2)$$

Momentum: (7.3)

$$u \frac{\partial u}{\partial x} + v \frac{\partial u}{\partial y} = \nu_{nf} \frac{\partial^2 u}{\partial y^2} + \frac{\mu_e}{\rho_{nf}} \left(H_x \frac{\partial H_x}{\partial x} + H_y \frac{\partial H_x}{\partial y} \right) - \frac{\sigma_{nf} B^2(x)}{\rho_{nf}} (u - U_\infty)$$

Induced magnetic field: (7.4)

$$u \frac{\partial H_x}{\partial x} + v \frac{\partial H_x}{\partial y} - \left(H_x \frac{\partial u}{\partial x} + H_y \frac{\partial u}{\partial y} \right) = \frac{1}{\mu_e \sigma_{nf}} \frac{\partial^2 H_x}{\partial y^2}$$

Thermal energy:

(7.5)

$$u \frac{\partial T}{\partial x} + v \frac{\partial T}{\partial y} = \alpha_{nf} \frac{\partial^2 T}{\partial y^2} + \frac{\mu_{nf}}{(\rho C_p)_{nf}} \left(\frac{\partial u}{\partial y} \right)^2 + \frac{1}{\sigma_{nf} (\rho C_p)_{nf}} \left(\frac{\partial H_x}{\partial y} \right)^2$$

These are subject to the following boundary conditions:

$$\left. \begin{aligned} u = \lambda U_\infty + \gamma \frac{\partial u}{\partial y}, \quad v = 0, \quad \frac{\partial H_x}{\partial y} = H_y = 0, \quad -K_{nf} \frac{\partial T}{\partial y} = q_w \quad \text{At } y = 0 \\ u \rightarrow U_\infty, \quad H_x \rightarrow H_0, \quad T \rightarrow T_\infty \quad \text{At } y \rightarrow \infty \end{aligned} \right\} \quad (7.6)$$

where $B(x) = B_0 x^{-1/2}$, with $B_0 \neq 0$, is the magnetic field strength and H_0 is the value of the uniform magnetic field at infinity upstream. The thermophysical relations of the base fluid and nanoparticles are given by

$$\nu_{nf} = \frac{\mu_{nf}}{\rho_{nf}}, \quad \mu_{nf} = \frac{\mu_f}{(1-\phi)^{2.5}}, \quad \rho_{nf} = (1-\phi)\rho_f + \phi\rho_s$$

$$\alpha_{nf} = \frac{k_{nf}}{(\rho C_p)_{nf}}, \quad (\rho C_p)_{nf} = (1-\phi)(\rho C_p)_f + \phi(\rho C_p)_s$$

$$\frac{\sigma_{nf}}{\sigma_f} = 1 + \frac{3((\sigma_s/\sigma_f)-1)\phi}{((\sigma_s/\sigma_f)+2)-\phi((\sigma_s/\sigma_f)-1)}, \quad \frac{k_{nf}}{k_f} = \frac{1-\phi+2\phi \frac{k_s}{k_s-k_f} \ln \frac{k_s+k_f}{2k_f}}{1-\phi+2\phi \frac{k_f}{k_s-k_f} \ln \frac{k_s+k_f}{2k_f}}$$

Following Ramli *et al.* (2017), let us introduce the following non-dimensional variables to streamline the mathematical analysis:

$$\psi = \nu_f \sqrt{Re_x} f(\eta), \quad \Phi = \frac{x}{\sqrt{Re_x}} H_0 g(\eta), \quad \eta = \frac{y}{x} \sqrt{Re_x}, \quad \theta(\eta) = \frac{T-T_\infty}{q_w x / K_f} \sqrt{Re_x} \quad (7.7)$$

where the stream functions are defined such that

$$u = \frac{\partial \psi}{\partial y} \quad \text{and} \quad v = -\frac{\partial \psi}{\partial x},$$

$$H_x = \frac{\partial \Phi}{\partial y} \quad \text{and} \quad H_y = -\frac{\partial \Phi}{\partial x}$$

Modifying the governing equations (7.3)–(7.5) by using (7.7), along with the boundary conditions (7.6), reduces them to the following non-dimensional form:

$$\frac{1}{a_1} f'''' + \frac{1}{2} a_2 f f'' - M g g'' + a_3 \beta (1 - f') = 0 \quad (7.8)$$

$$g''' + \frac{1}{2} a_3 Prm (f g'' - f'' g) = 0 \quad (7.9)$$

$$a_4 \theta'' + \frac{1}{2} a_5 Pr (f \theta' - f' \theta) + \frac{Pr Ec}{a_1} (f'')^2 + \frac{M pr Ec}{a_3 Prm} (g'')^2 = 0 \quad (7.10)$$

where

$$a_1 = (1 - \phi)^{2.5}, \quad a_2 = 1 - \phi + \phi \frac{\rho_s}{\rho_f}$$

$$a_3 = \frac{\sigma_{nf}}{\sigma_f} = 1 + \frac{3((\sigma_s/\sigma_f)-1)\phi}{((\sigma_s/\sigma_f)+2)-\phi((\sigma_s/\sigma_f)-1)}$$

$$a_4 = \frac{k_{nf}}{k_f} = \frac{(k_s+2k_f)-2\phi(k_f-k_s)}{(k_s+2k_f)+\phi(k_f-k_s)}, \quad a_5 = 1 - \phi + \phi \frac{(\rho c_p)_s}{(\rho c_p)_f}$$

The corresponding boundary conditions are

$$\left. \begin{aligned} f(0) = 0, f'(0) = \lambda + \alpha f''(0), g(0) = g''(0) = 0, \theta'(0) = -\frac{k_f}{k_{nf}} \quad \text{as } \eta = 0 \\ f' \rightarrow 1, g' \rightarrow 1, \theta \rightarrow 0 \quad \text{as } \eta \rightarrow \infty \end{aligned} \right\} \quad (7.11)$$

The dimensionless parameters are the magnetic parameter $M = \mu_e H_0^2 / U_\infty^2 \rho_f$, the induced magnetic parameter $\beta = \sigma_f B_0^2 / U_\infty \rho_f$, the Eckert number $Ec = U_\infty^2 / \Delta T (C_p)_f$, where $\Delta T = k_f \sqrt{Re_x} / q_w$, the Prandtl number $Pr = \nu_f (\rho c_p)_f / k_f$, the magnetic Prandtl number $Prm = \mu_e \nu_f \sigma_f$, the velocity ratio parameter $\lambda = U_w / U_\infty$, the slip parameter $\alpha = c \sqrt{U_\infty / \nu_f}$, $\gamma = c \sqrt{x}$, and the local Reynolds number $Re_x = U_\infty x / \nu_f$.

The definitions of the skin friction coefficient and the rate of heat transfer are as follows:

$$C_f = \frac{\tau_w}{\rho_f U_\infty^2} \quad \text{and} \quad Nu_x = \frac{x q_w}{K_f (T_w - T_\infty)} \quad (7.12)$$

where τ_w is the surface shear stress along the x -direction and q_w is the heat flux; these are given by

$$\tau_w = \mu_{nf} \left(\frac{\partial u}{\partial y} \right)_{y=0} \quad \text{and} \quad q_w = -k_{nf} \left(\frac{\partial T}{\partial y} \right)_{y=0} \quad (7.13)$$

The non-dimensional forms of the skin friction coefficient C_f and the local Nusselt number Nu_x , in equation (7.12) are

$$\sqrt{Re_x} C_f = \frac{1}{(1-\phi)^{2.5}} f''(0) \quad \text{and} \quad (Re_x)^{-1/2} Nu_x = \frac{1}{\theta(0)} \quad (7.14)$$

7.2 Numerical Solution with the Spectral Relaxation Method

The nonlinear system of coupled equations (7.1)–(7.5), together with the boundary conditions (7.6), are solved numerically using the SRM. We first define $f'(\eta) = F(\eta)$ and $g'(\eta) = G(\eta)$ and then arrange the problem into the following set of equations:

$$f' = F$$

$$\frac{1}{a_1} F'' + \frac{1}{2} a_2 f F' - M g G' + a_3 \beta (1 - F) = 0$$

$$g' = G$$

$$G'' + \frac{1}{2} a_3 Pr m (f G' - g F') = 0$$

$$a_4 \theta'' + \frac{1}{2} a_5 Pr (f \theta' - F \theta) + \frac{Pr Ec}{a_1} (F')^2 + \frac{M Pr Ec}{a_5 Pr m} (G')^2 = 0$$

The associated boundary conditions become

$$f(0) = 0, F(0) = \lambda + \alpha F'(0), g(0) = G'(0) = 0, \theta'(0) = -\frac{k_f}{k_{nf}}$$

$$F(\infty) \rightarrow 1, \quad G(\infty) \rightarrow 1, \quad \theta(\infty) \rightarrow 0$$

The following iteration scheme is obtained using the SRM algorithm

$$\frac{1}{a_1} F''_{r+1} + \frac{1}{2} a_2 f_r F'_{r+1} - M g_r G'_r + a_3 \beta (1 - F_{r+1}) = 0 \quad (7.15)$$

$$f'_{r+1} = F_{r+1} \quad (7.16)$$

$$G''_{r+1} + \frac{1}{2}a_3Prm(f_{r+1}G'_{r+1} - g_rF'_{r+1}) = 0 \quad (7.17)$$

$$g'_{r+1} = G_{r+1} \quad (7.18)$$

$$a_4\theta''_{r+1} + \frac{1}{2}a_5Pr(f_{r+1}\theta'_{r+1} - F_{r+1}\theta_{r+1}) + \frac{PrEc}{a_1}(F'_{r+1})^2 + \frac{MPrEc}{a_5Prm}(G_{r+1}')^2 = 0 \quad (7.19)$$

The boundary conditions for the above iteration scheme are as follows:

$$F_{r+1}(0) = \lambda + \alpha F'_{r+1}(0), F_{r+1}(\infty) = 1 \quad (7.20)$$

$$f_{r+1}(0) = 0 \quad (7.21)$$

$$G'_{r+1}(0) = 0, G'_{r+1}(\infty) = 1 \quad (7.22)$$

$$g_{r+1}(0) = 0 \quad (7.23)$$

$$\theta'_{r+1}(0) = -\frac{k_f}{k_{nf}}, \theta_{r+1}(\infty) = 0 \quad (7.24)$$

After discretizing equations (6.29)–(6.33) using the Chebyshev pseudo-spectral method, the resulting matrix equations are as follows:

$$C_1\mathbf{F}_{r+1} = T_1, \quad F_{r+1}(\xi_N) = 1, F_{r+1}(\xi_0) = \lambda + \alpha F'_{r+1}(\xi_0) \quad (7.25)$$

$$C_2\mathbf{f}_{r+1} = T_2, \quad f_{r+1}(\xi_N) = 0 \quad (7.26)$$

$$C_3\mathbf{G}_{r+1} = T_3, \quad G_{r+1}(\xi_N) = 1, G'_{r+1}(\xi_0) = 0 \quad (7.27)$$

$$C_4\mathbf{g}_{r+1} = T_4, \quad g_{r+1}(\xi_N) = 0 \quad (7.28)$$

$$C_5\boldsymbol{\theta}_{r+1} = T_5, \quad \theta_{r+1}(\xi_N) = 0, \theta'_{r+1}(\xi_0) = -\frac{k_f}{k_{nf}} \quad (7.29)$$

where

$$C_1 = \text{diag}\left(\frac{1}{a_1}\right)\mathbf{D}^2 + \frac{1}{2}a_2\text{diag}(\mathbf{f}_r)\mathbf{D} - a_3\beta\mathbf{I}, \quad T_1 = M\mathbf{g}_r\mathbf{G}'_r - a_3\beta \quad (7.30)$$

$$C_2 = \mathbf{D}, \quad T_2 = \mathbf{F}_{r+1} \quad (7.31)$$

$$C_3 = \mathbf{D}^2 + \frac{1}{2}a_3Prm \text{diag}(\mathbf{f}_{r+1})\mathbf{D}, \quad T_3 = \frac{1}{2}a_3Prm \mathbf{g}_r \mathbf{F}'_{r+1} \quad (7.32)$$

$$C_4 = \mathbf{D}, \quad T_4 = \mathbf{G}_{r+1} \quad (7.33)$$

$$\left. \begin{aligned} C_5 &= \text{diag}(a_4)\mathbf{D}^2 + \frac{1}{2}Pra_5 \text{diag}(\mathbf{f}_{r+1})\mathbf{D} - \frac{1}{2}Pra_5 \text{diag}(\mathbf{F}_{r+1})\mathbf{I}, \\ T_5 &= -\frac{PrEc}{a_1}(\mathbf{F}'_{r+1})^2 - \frac{MPrEc}{a_3Prm}(\mathbf{G}_{r+1}')^2 \end{aligned} \right\} \quad (7.34)$$

The SRM scheme is outlined by equations (7.25) to (7.29), which can be used to accurately determine the estimated values of the controlling functions through the spectral collocation approach. The iteration procedure requires an initial estimate that satisfies the boundary constraints and is determined by the known physical properties of the flow parameters. The pertinent preliminary estimations are as follows:

$$f_0(\eta) = (1 + \lambda + \alpha)\eta + e^{-\eta}, \quad g_0(\eta) = \eta - (1 + \eta)e^{-\eta} + 1, \quad \theta_0(\eta) = -\frac{k_f}{k_{nf}}e^{-\eta} \quad (7.35)$$

The SRM scheme (7.25)–(7.29) is executed iteratively, starting with the initial assumptions (7.35), until the following criterion is fulfilled:

$$\max(\|F_{r+1} - F_r\|; \|G_{r+1} - G_r\|; \|\theta_{r+1} - \theta_r\|) < E_r$$

The convergence tolerance is set at $E_r = 10^{-8}$.

7.3 Observations and Discussion

Following the numerical procedure described above, the impacts of velocity slip, the magnetic parameters, and the volume fraction of solid ferroparticles on the dimensionless velocity, induced magnetic field, and temperature distributions, as well as the skin friction and heat transfer rate, are presented graphically for three ferroparticles in a water-based nanofluid, namely magnetite, cobalt ferrite, and *Mn-Zn* ferrite. The influence of the volume fraction ϕ of solid ferroparticles is varied from 0 to 0.2, where $\phi = 0$ denotes pure water. Taken from the work of Khan *et al.* (2015), the thermophysical properties of the base fluid (water) and the ferroparticles (magnetite, cobalt ferrite, and *Mn-Zn* ferrite) are provided in Table 7.1.

A comparison with the corresponding computation has been done in Table 7.2 to assess the accuracy and reliability of the numerical algorithm used. The $f''(0)$ values are compared with the previous studies by Khan *et al.* (2015), Ramli *et al.* (2017), and Mohamed *et al.* (2021). The numerical results are found to be in good alignment with this earlier research.

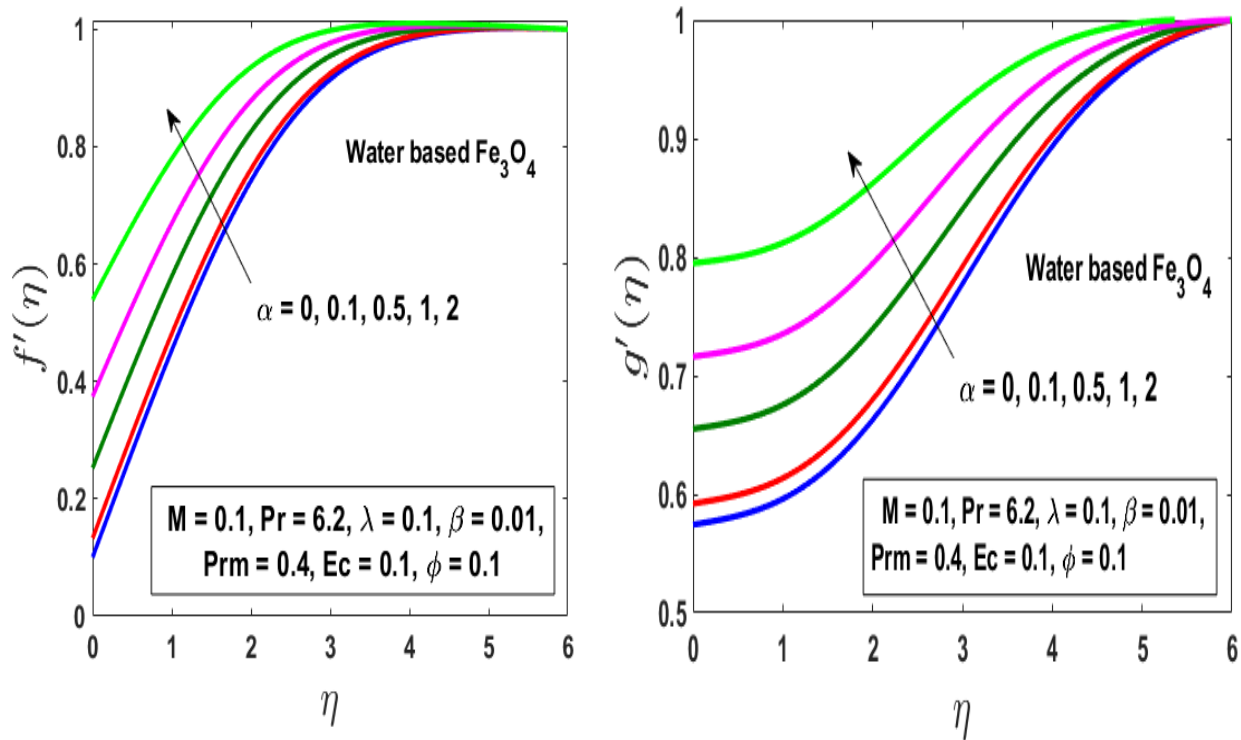
Table 7.1 Thermophysical properties of the base fluid and magnetic nanoparticles

Physical property	Base fluid (water)	Fe_3O_4	$CoFe_2O_4$	$Mn-ZnFe_2O_4$
C_p (J/kg · K)	4,179	670	700	800
ρ (kg/m ³)	997.1	5180	4907	4900
k (W/m · K)	0.613	9.7	3.7	5
σ (S/m)	0.05	0.112×10^6	5.51×10^9	5.32×10^{-9}

Table 7.2 Comparison of $f''(0)$ values for various values of α and β when

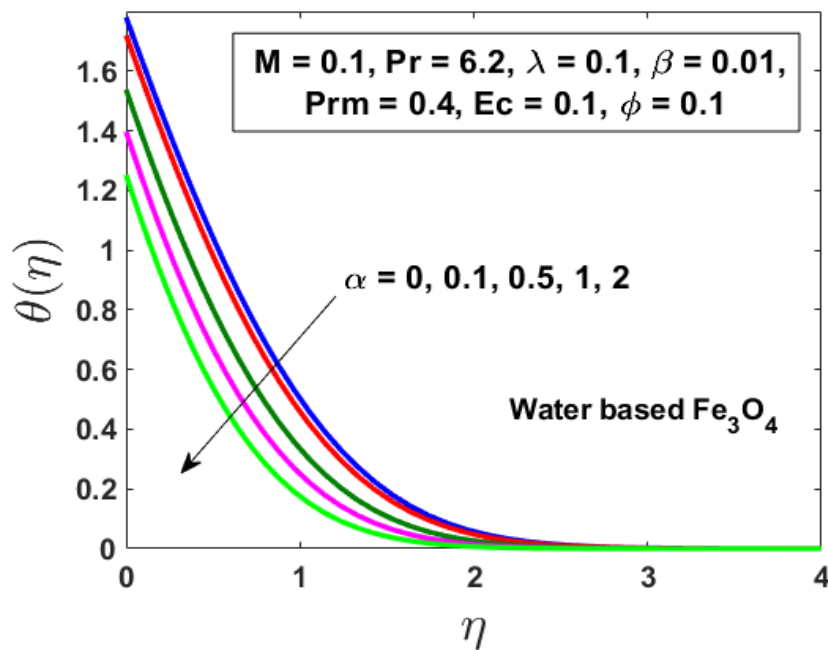
$$Pr = 6.2, Prm = 1, \text{ and } \phi = M = \lambda = Ec = 0$$

α	β	Present study	Mohamed (2021)	Ramli (2017)	Khan (2015)
0	0	0.332057356335180076	0.332057	0.33206	0.33206
0	1	1.04400906092390411	1.044009	1.04400	1.04400
0.5	1	0.698724365148012726	0.698724	0.69872	0.69872



(a)

(b)



(c)

Fig. 7.2 Impact of slip parameter α on (a) velocity, (b) induced magnetic field, and (c) temperature

Fig. 7.2 (a–c) displays the impacts of the slip parameter α on the velocity distribution $f'(\eta)$, magnetic field profile $g'(\eta)$, and temperature distribution $\theta(\eta)$ of water-based Fe_3O_4 ferrofluid. There is significant resistance to fluid flow without slip effects. The flow resistance reduces as the slip parameter rises, and consequently, the velocity increases at the surface, which is visible in Fig. 7.2 (a). It can be observed in Fig. 7.2 (b) that the induced magnetic field $g'(\eta)$ exhibits the same phenomenon. Fig. 7.2 (c) shows that the thickness of the thermal boundary layer decreases as the slip parameter increases.

The variation of the velocity with the magnetic parameter M is depicted in Fig. 7.3 (a–c). The velocity boundary-layer thickness grows with the magnetic parameter M . Unusually, a stronger magnetic field prevents the flow of nanofluid. When magnetic nanoparticles are present, and the magnetic parameter M is increased, the Lorentz force increases and works against the flow of the fluid. Fig. 7.3 (b) shows how the magnetic parameter M affects the induced magnetic field. The values rapidly approach 1 as the value of M is increased, and this causes the thickness of the generated magnetic field boundary layer to expand as well. This occurs because the induced and applied magnetic fields are in the same direction. A graphical representation of the variation of temperature with the value of the magnetic parameter M is shown in Fig. 7.3 (c). Due to the Lorentz force, the magnetic field retards the free convection flow in the boundary layer. Consequently, the surface temperature and the thickness of the thermal boundary layer are observed to grow with the value of M .

The effects of the magnetic Prandtl number Pr_m on the induced magnetic field are illustrated in Fig. 7.4. In convection heat transfer, the magnetic Prandtl number, which signifies the ratio of the viscous to the magnetic diffusivity, is equivalent to the ordinary Prandtl number, which is the ratio of the viscous and thermal diffusivities. The magnetic Prandtl number usually measures the relative magnitude of the magnetic and hydrodynamic boundary-layer thicknesses, often below or equal to unity. Additionally, a significant reduction in flow velocity is seen when the magnetic Prandtl number rises.

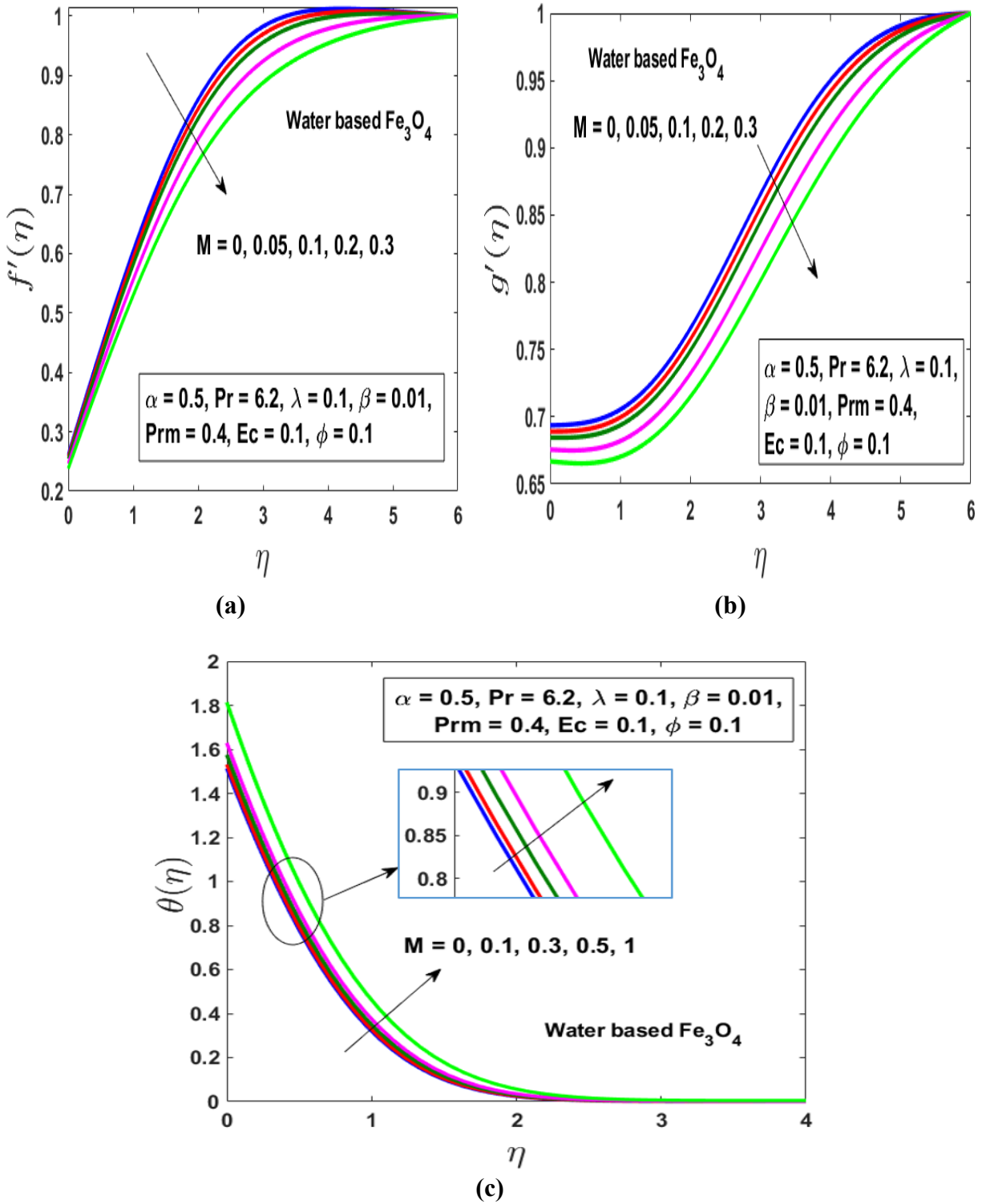


Fig. 7.3 Impact of magnetic parameter M on (a) velocity, (b) induced magnetic field, and (c) temperature

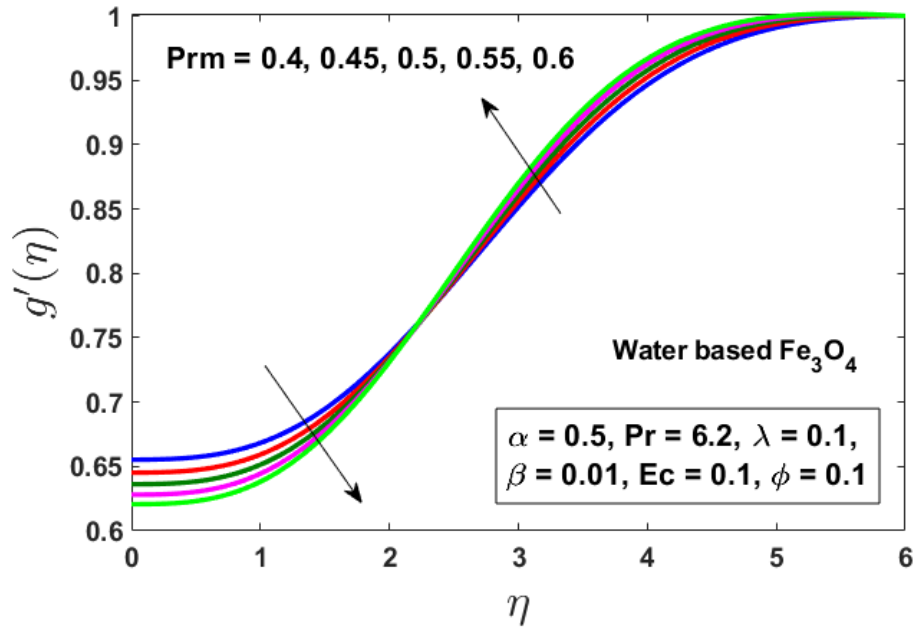


Fig. 7.4 Induced magnetic field profiles for various magnetic Prandtl number Prm

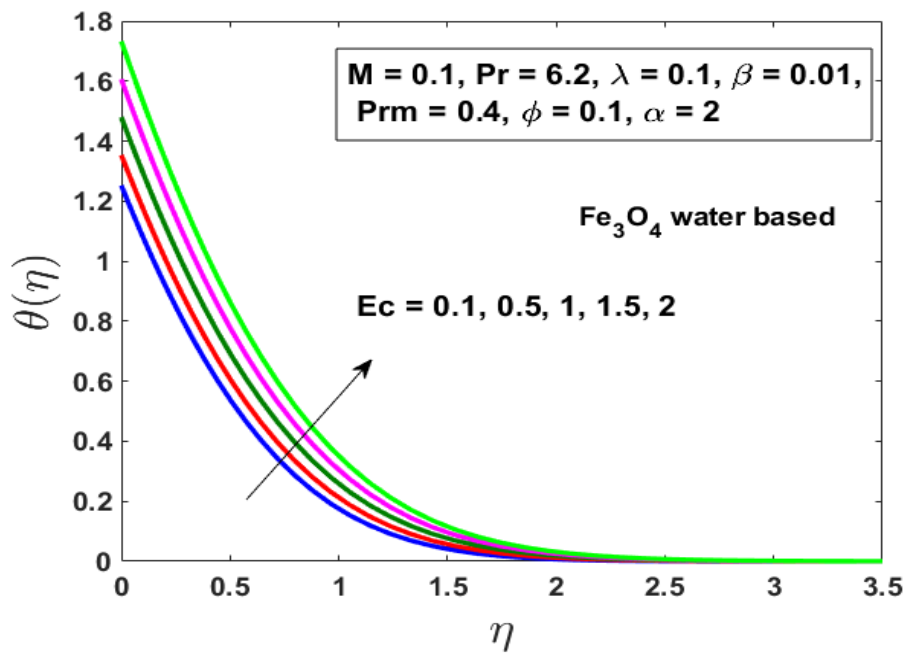


Fig. 7.5 Temperature distributions for different values of Eckert number Ec

Fig. 7.5 shows the positive effect of the heat dissipation term (Ec) on the temperature dispersion of water-based Fe_3O_4 ferrofluid. Increasing the Eckert number results in an elevated energy profile. Because of the disparity between the kinetic energy of the nanofluids and the boundary-layer heat enthalpy, the effect is intense close to the velocity slip plate. The local heat increases with the difference between the local and plate heat. This increases the thickness of the thermal boundary layer, leading to an intense heat distribution in the nanofluid. Consequently, the temperature of the fluid increases.

Fig. 7.6 (a–c) shows the variation of the dimensionless velocity profiles $f'(\eta)$, magnetic field profiles $g'(\eta)$, and temperature profiles $\theta(\eta)$, with the moving parameter α for three water-based ferrofluids: Fe_3O_4 , $CoFe_2O_4$, and $Mn-ZnFe_2O_4$. The velocity profile shows that Fe_3O_4 has a higher impact than the other magnetic particles and attains the highest velocity. For the induced magnetic field distribution, $CoFe_2O_4$ has a lower impact than the other magnetic particles, and $Mn-ZnFe_2O_4$ exhibits the highest induced magnetic field boundary layer. Fig. 7.6 (c) shows that $CoFe_2O_4$ has the highest thermal boundary layer.

The study of the magnetic effects on flow and heat transfer characteristics is displayed in Fig. 7.7 (a–b) for the three selected ferroparticles. Fig. 7.7 (a–b) shows that the $Mn-ZnFe_2O_4$ -water nanofluid has the lowest velocity and the thinnest boundary layer but the highest induced magnetic field. The highest temperature profile of Fe_3O_4 is seen in Fig. 7.7 (c).

Fig. 7.8 (a–b) illustrates the impacts of the concentration of magnetic nanoparticles ϕ on the velocity distributions and induced magnetic field considering three water-based ferrofluids: Fe_3O_4 , $CoFe_2O_4$, and $Mn-ZnFe_2O_4$. It is observed that the ferrofluid flow increases with the solid volume fraction ϕ . Due to an increase in fluid motion resulting from the addition of nanoparticles, the nanofluid velocity and temperature increase as the volume fraction of the fluid increases. The most elevated thermal boundary layer is found in manganese–zinc ferrite, while the highest velocity distribution is identified in magnetite.

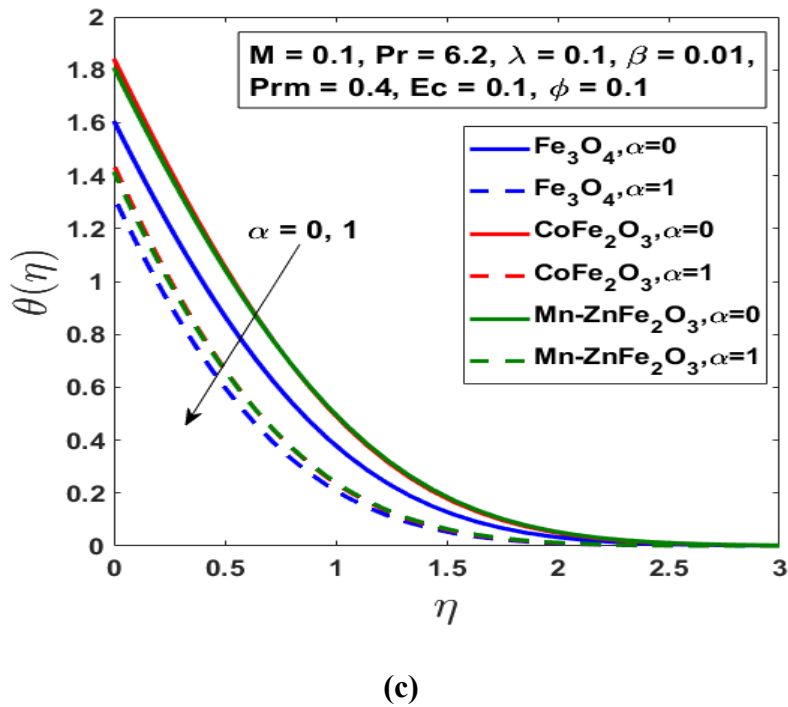
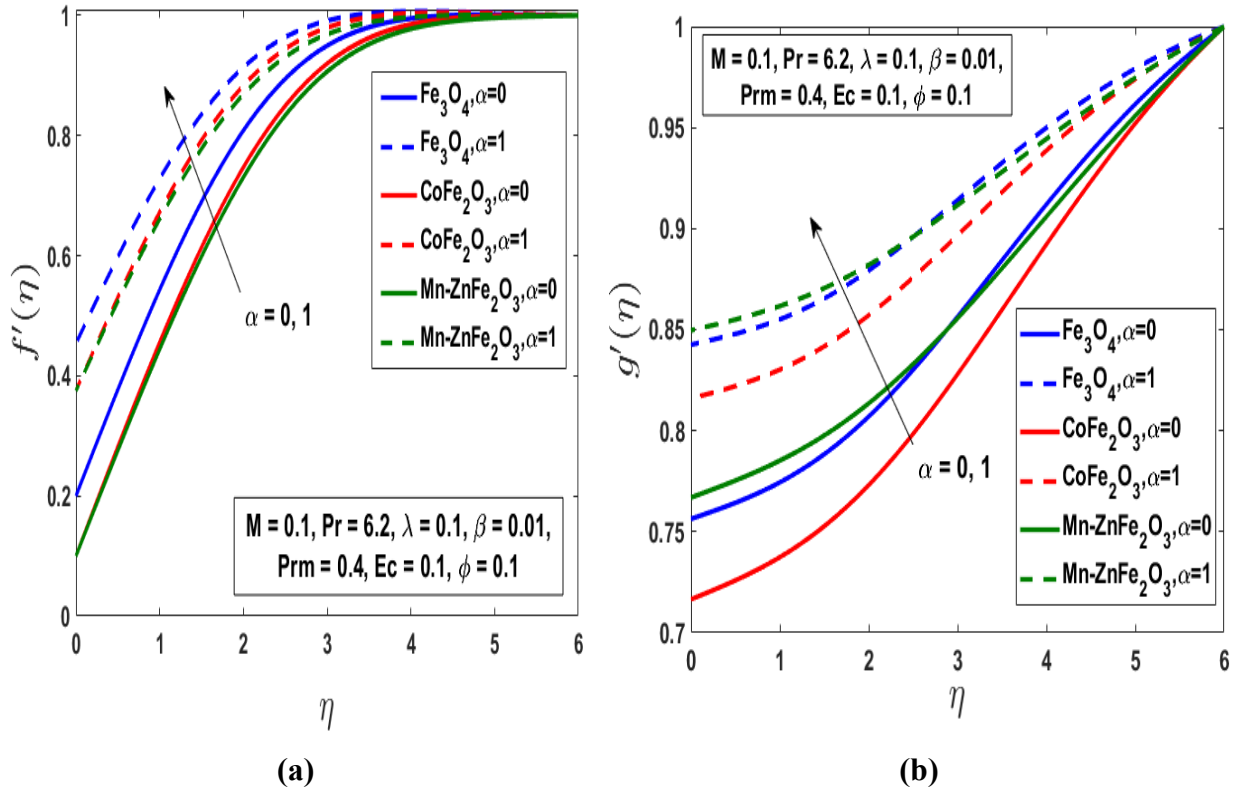


Fig. 7.6 Impact of slip parameter α on (a) velocity, (b) induced magnetic field, and (c) temperature for the ferroparticles

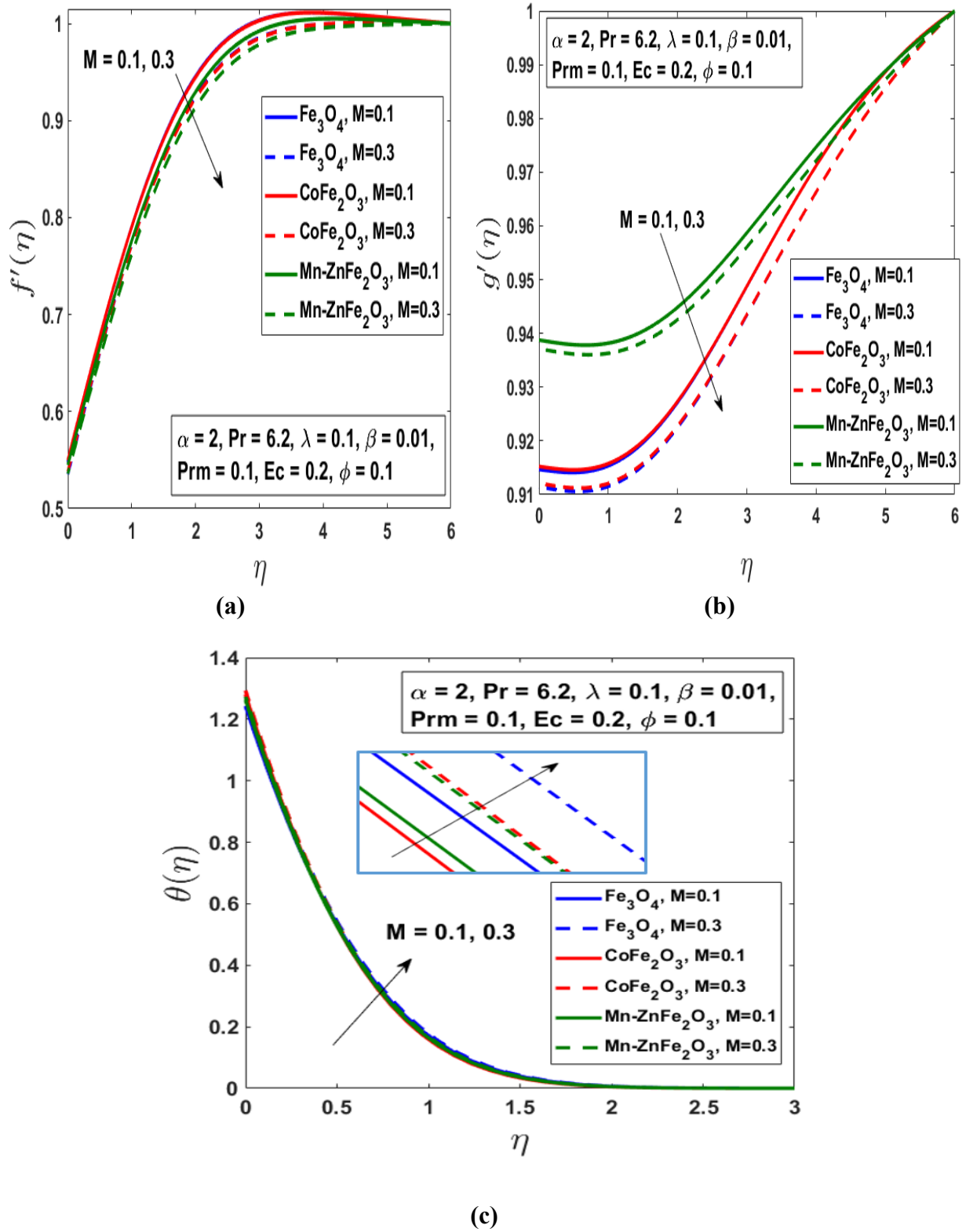


Fig. 7.7 Impact of magnetic parameter M on (a) velocity, (b) induced magnetic field, and (c) temperature for the ferroparticles

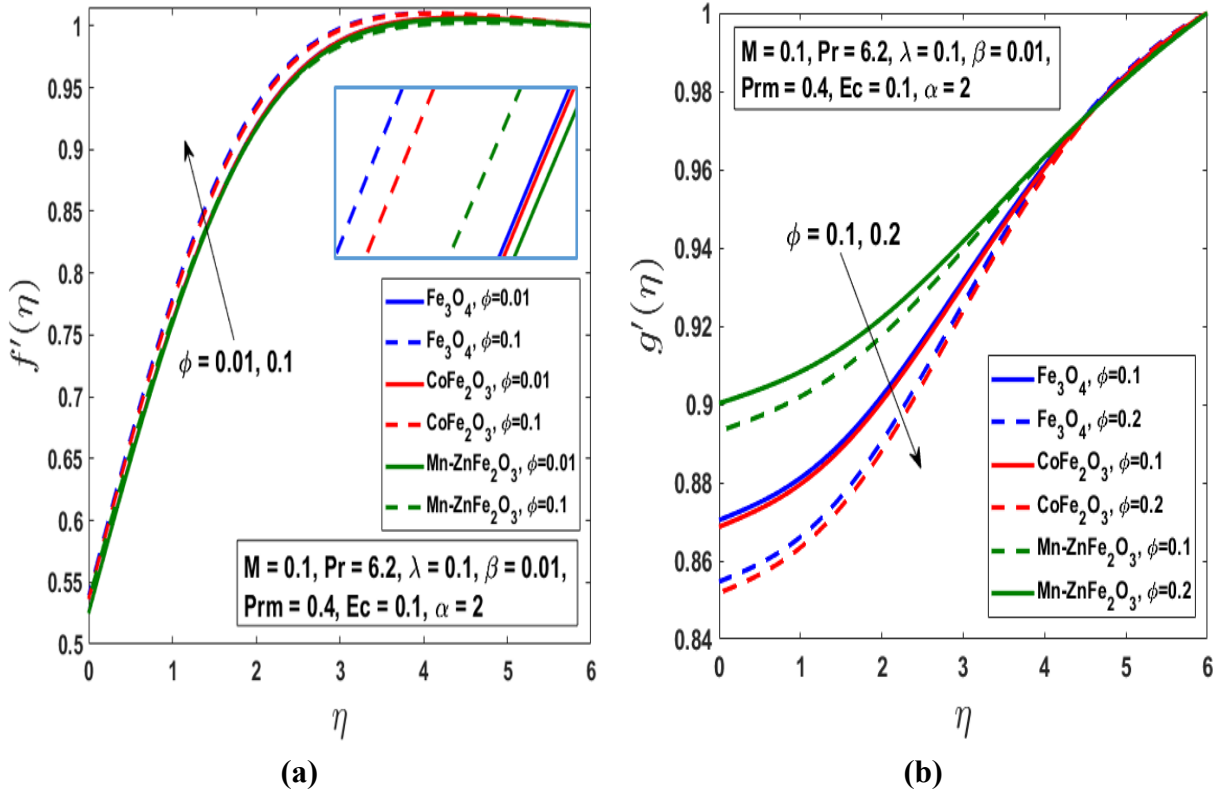


Fig. 7.8 Impact of ϕ on (a) velocity and (b) induced magnetic field for the ferroparticles

The variation of the reduced skin friction coefficient $C_f\sqrt{Re_x}$ and the Nusselt number $Nu_x(Re_x)^{-1/2}$, for different values of velocity slip, are shown in Figs. 7.9 and 7.10, respectively. For each ferrofluid, the skin friction decreases as the slip parameter increases due to a reduction in flow resistance. For the same volume fraction, it is observed that the magnetite nanoparticles exhibit a higher resistance than the other two ferrofluids. Since the magnetite nanofluid is more viscous than the cobalt ferrite and manganese–zinc ferrite nanofluids, there is more surface friction. From Fig. 7.10, with increasing slip parameters, the Nusselt numbers rise, indicating the capacity for fluid convection. The increase in α induces the fluid velocity at the surface to rise, promoting greater fluid particle movement and convective heat transfer in the boundary layer. Again, the Nusselt numbers are higher for magnetite nanoparticles. In comparing the three ferroparticles, magnetite’s high thermal conductivity has the greatest impact on the fluid heat transfer capability and leads to a higher Nusselt number.

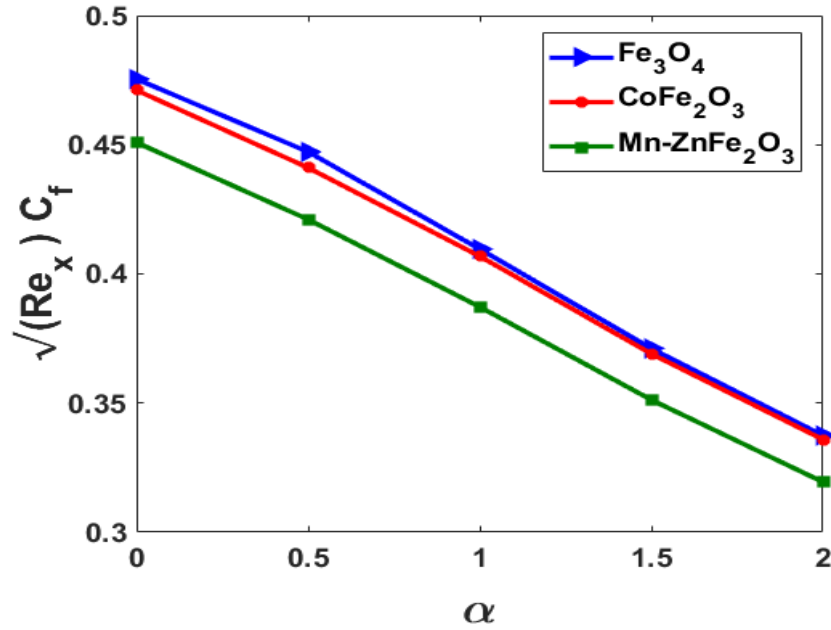


Fig. 7.9 Variation of the skin friction coefficient with α for different ferrofluids

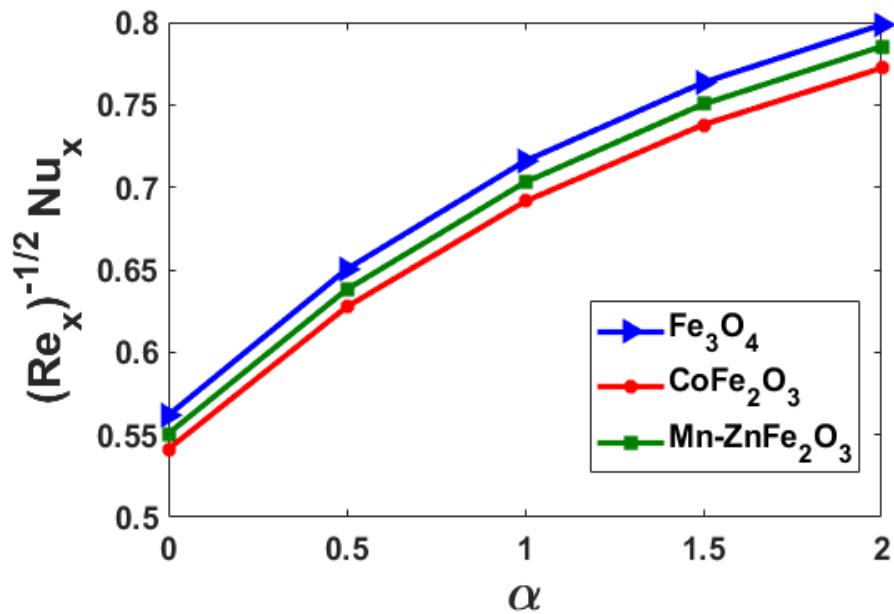


Fig. 7.10 Variation of the Nusselt number with α for different ferrofluids

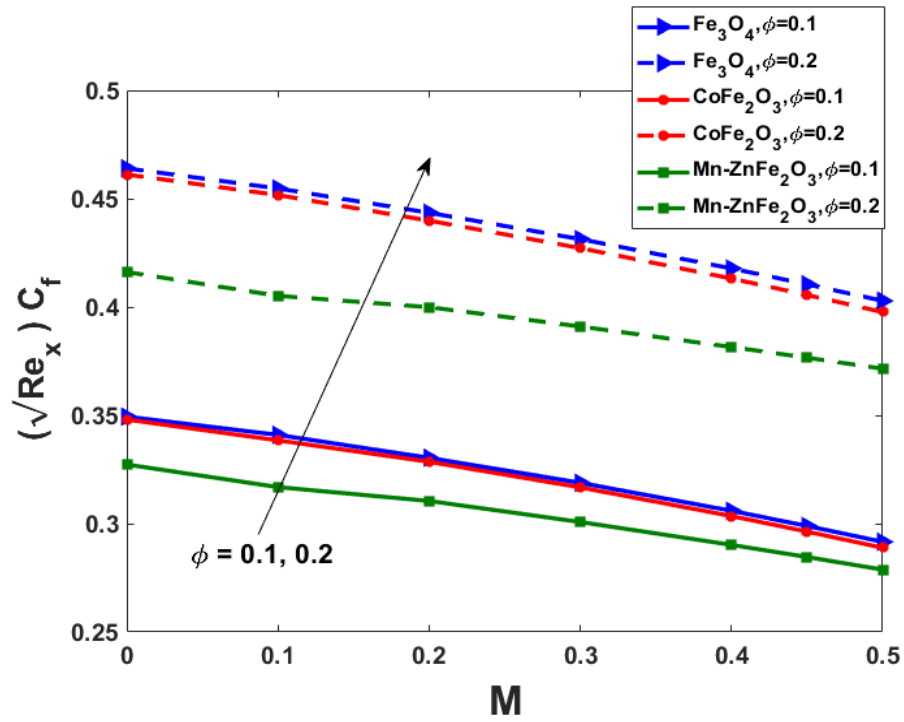


Fig. 7.11 Variation of the skin friction coefficient with ϕ and M for different ferrofluids

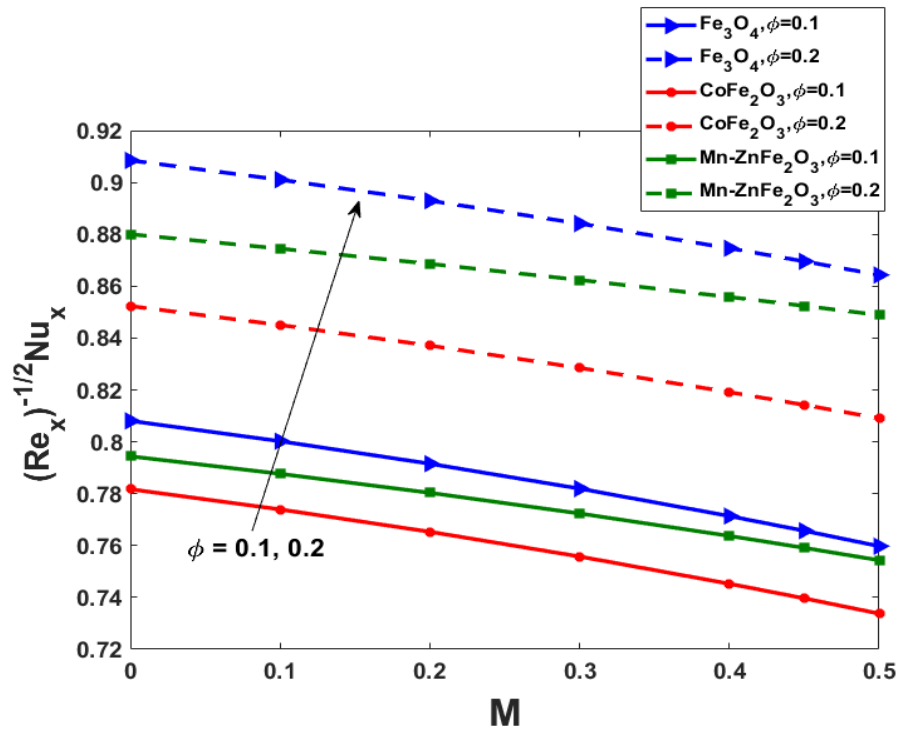


Fig. 7.12 Variation of the Nusselt number with ϕ and M for different ferrofluids

Figs. 7.11 and 7.12 depict the cumulative impact of the magnetic nanoparticle volume fraction ϕ and the magnetic interaction parameter M on the reduced skin friction coefficient $C_f\sqrt{Re_x}$ and Nusselt number $Nu_x(Re_x)^{-1/2}$ in the case of three different ferrofluids. For all types of ferrofluids, the skin friction coefficient and Nusselt number fall as M increases but grow with the concentration of magnetic nanoparticles ϕ .

7.4 Summary

The MHD flow and heat transfer of nanofluids containing three preferred magnetic nanoparticles across a moving flat plate with velocity slip, in the presence of an induced magnetic field and uniform heat flux, have been numerically investigated. The characteristics and impacts of the slip parameter α , the magnetic parameter M , and the ferrofluid volume percentage ϕ of three distinct types of magnetic nanoparticles on the Nusselt number and the skin friction coefficient have been investigated and discussed. Ferrofluid skin friction and the rate of heat transfer are increased when the magnetic field is applied because it lowers the dimensionless velocity and raises the dimensionless surface temperature in comparison with the hydrodynamic scenario.

Chapter 8

Conclusions

8.1 Summary of the Outcomes

The steady MHD viscous flow resulting from the motion of a plate through an electrically conducting nanofluid containing several kinds of nanoparticles has been studied in this thesis. In Chapter 3, an MHD thermal-convection boundary-layer flow of electroconductive nanofluids with radiative heat transfer and magnetic induction has been investigated numerically. The key results of this study can be summarized as follows:

- The velocity and induced magnetic field profiles decrease with increased magnetic body force parameters.
- Increasing magnetic body force, thermophoresis, and radiative parameters enhance the thermal boundary-layer thickness. In contrast, it falls with growing wall velocity, Brownian motion, and Prandtl number.
- The induced magnetic field stream function is affected more strongly by the magnetic Prandtl number Pr_m than the skin friction and heat transfer coefficients.
- The nanoparticle concentration increases with higher thermophoresis and Prandtl number values, whereas it is suppressed with increasing moving wall velocity, Brownian motion, radiative flux, and Lewis number.

In Chapter 4, hydromagnetic metallic nanofluid flows with generated magnetic field effects on an inclined flat plate, either stationary or in motion, have been studied theoretically and computationally with convective boundary conditions. From this study, some key results are as follows:

- The velocity profiles increase with the Grashof number, Biot number, and magnetic field parameter. The opposite trend is observed for the nanoparticle volume fraction and inclination angle in a moving flat plate.

- The induced magnetic field increases with the nanoparticle volume fraction, Grashof number, Biot number, magnetic Prandtl number, and magnetic field parameter. The opposite trend is observed for the angle of inclination in the case of a moving flat plate.
- The temperature profiles increase with nanoparticle volume fraction, angle of inclination, and Biot number. In contrast, they fall with increasing values of the Grashof number and magnetic field parameter.
- The skin friction coefficient increases with the nanoparticle volume fraction and magnetic field parameter in the case of the stationary flat plate, and this trend is reversed in the case of a moving plate, for both the copper–water and silver–water nanofluids.
- In the stationary flat plate and moving plate cases, the reduced Nusselt number decreases as the nanoparticle volumetric fraction and magnetic interaction parameter increase, for both Cu and Ag nanoparticles.

The impacts of temperature- and space-dependent internal heat generation/absorption are examined in Chapter 5. The key observations are summarized as follows:

- Velocity and induced magnetic field increase for $\lambda < 1$ but reduce for $\lambda > 1$ as α increases, and the opposite behavior is observed for the temperature profile.
- Motion and induced magnetic field both increase with M for $\lambda < 1$ and decrease with M for $\lambda > 1$.
- The induced magnetic field strengthens or weakens as χ increases, for $\lambda < 1$ and $\lambda > 1$, respectively.
- The thermal boundary-layer thickness increases with A^* for all values of λ .
- Increasing values of B^* reduce the thermal boundary-layer thickness for $\lambda < 1$ but increase it for $\lambda > 1$.
- Changes in the skin friction coefficient and Nusselt number with M are greater for larger values of ϕ . Ag –water nanofluid exhibits higher drag than the Cu –water and TiO_2 –water nanofluid for $\lambda < 1$, and the opposite trend is observed for $\lambda > 1$.
- Nanofluid with TiO_2 particles has a higher heat transfer rate than the nanofluid with Cu and Ag nanoparticles for all values of λ .

Chapter 6 studies viscous dissipation and aligned induced magnetic field when an electrically conducting nanofluid passes a semi-infinite moving flat plate. The flow velocity and magnetic field vectors away from the surface are parallel. The work's key findings are as follows:

- Higher values of the velocity ratio parameter ϵ increase the rate of change of velocity and induced magnetic field in water-based alumina nanoparticles. However, the reverse pattern is shown by the rate of change of temperature.
- The nanofluids' momentum boundary-layer thickness decreases, while the thermal boundary-layer thickness increases, with increased magnetic field parameter M .
- Rising Ec values accelerate the rate at which the temperature of water-based nanoparticles changes.
- Ag has a thicker momentum boundary layer, while Al_2O_3 has a thinner boundary layer.
- Al_2O_3 has more impact on temperature, whereas Ag has less impact.
- Ag -water nanofluids exhibit higher drag than other nanoparticles.
- The nanofluid with Ag particles has a higher heat transfer rate than the nanofluids with the other three nanoparticles.
- The TiO_2 -water nanofluid has the lowest cooling rate.

The work in Chapter 7 investigates the phenomenon of unstable MHD magnetic nanofluid flow across a moving plate. The fluid is water-based, and the influence of an induced magnetic field, momentum slip, and uniform heat flux are examined. The significant findings from this study are as follows:

- The velocity increases with the velocity slip α and decreases when the magnetic parameter M is increased.
- The induced magnetic field strengthens for higher velocity slip α and weakens under the action of the magnetic parameter M and magnetic Prandtl number Pr_m .
- The energy field lessens with rising velocity slip α and is significantly boosted by the effects of the magnetic parameter M and Eckert number Ec .
- For α , Fe_3O_4 obtains the maximum velocity, $Mn-ZnFe_2O_4$ shows the largest induced magnetic field, and $CoFe_2O_4$ exhibits the thickest thermal boundary layer.

- The highest velocity and temperature profile of magnetite and the greatest induced magnetic field of manganese-zinc ferrite are noticed for growing M .
- $Mn-ZnFe_2O_4$ exhibits the highest induced magnetic field, whereas Fe_3O_4 has the highest velocity dispersion with rising solid volume fraction ϕ .
- The slip parameter has the effect of diminishing friction and accelerating heat transfer.
- With increasing nanoparticle volume fraction, skin friction and heat transmission rates rise.
- Both skin friction and the heat transfer rate grow with the magnetic field strength.
- Magnetite Fe_3O_4 exhibits higher drag and has a higher heat transfer rate than the cobalt ferrite and $Mn-Zn$ ferrite.

8.2 Future Prospects

This study has shown that the SRM is a versatile and powerful numerical technique for nonlinear electromagnetic-induction nanofluid materials processing flows. However, attention has been confined to Newtonian nanofluids. Future studies will explore rheological nanofluid behaviour, including viscoelastic (Rana *et al.*, 2017) and viscoplastic (Thumma *et al.*, 2020) models, and will be communicated imminently. Generalizing this study to consider electric field effects (Beg *et al.*, 2013) is also under consideration. Additionally, several other physicochemical products arise in magnetic nanomaterial synthesis, including shape effects of nanoparticles (Saleem *et al.*, 2020), Hiemenz stagnation and slip flows (Nadeem *et al.*, 2020), Hall current effects (Bhatti *et al.*, 2019), and bioconvection effects in which nanoparticles are combined with micro-organism doping to achieve dual benefits (Bhatti *et al.*, 2020). Furthermore, alternative nanoparticles, such as molybdenum disulfide (Sowmya *et al.*, 2019) and triple diffusion (with two nanoparticle species; Archana *et al.*, 2018), could also be considered, and efforts in this direction are also being explored. In future, a multitude of physical and technical challenges might be resolved by the SRM (Kumar *et al.*, 2022; Golla *et al.*, 2023; Maiti *et al.*, 2023; Rafique *et al.*, 2023). All these areas represent promising directions for building on the studies presented.

References

- Abo-Eldahab, E.M. and El Aziz, M.A. (2005). Viscous dissipation and Joule heating effects on MHD-free convection from a vertical plate with power-law variation in surface temperature in the presence of Hall and ion-slip currents. *Applied Mathematical Modelling*, 29 (6), 579–595.
- Abu-Nada, E. (2008). Application of nanofluids for heat transfer enhancement of separated flows encountered in a backward facing step. *International Journal of Heat and Fluid Flow*, 29(1), 242–249.
- Adem, G. A. and Kishan, N. (2018). Slip effects in a flow and heat transfer of a nanofluid over a nonlinearly stretching sheet using optimal homotopy asymptotic method. *Int. J. Eng. Manuf. Sci*, 8(1), 25–46.
- Afzal, N., Badaruddin, A. and Elgarvi, A. A. (1993). Momentum and heat transport on a continuous flat surface moving in a parallel stream. *International Journal of Heat and Mass Transfer*, 36(13), 3399–3403.
- Ahmad, S., Rohni, A. M. and Pop, I. (2011). Blasius and Sakiadis problems in nanofluids. *Acta Mechanica*, 218, 195–204.
- Ajibade, A. O. and Umar, A. M. (2020). Effects of viscous dissipation and boundary wall thickness on steady natural convection Couette flow with variable viscosity and thermal conductivity. *International Journal of Thermofluids*, 7–8, 100052.
- Akbarzadeh, A., Samiei, M., Davaran, S. (2012). Magnetic nanoparticles: Preparation, physical properties, and applications in biomedicine. *Nanoscale Research Letters*, 7, 144.
- Ali, M. and Al-Yousef, F. (1998). Laminar mixed convection from a continuously moving vertical surface with suction or injection. *Heat and Mass Transfer*, 33 (4), 301–306.
- Al-Sanea, S. A. (2004). Mixed convection heat transfer along a continuously moving heated vertical plate with suction or injection. *International Journal of Heat and Mass Transfer*, 47(6-7), 1445–1465.
- Aminreza, N., Rashid, P., Mohammad, G. (2012). Effect of partial slip boundary condition on the flow and heat transfer of nanofluids past stretching sheet prescribed constant wall temperature. *International Journal of Thermal Sciences*, 54(4), 253–261.

- Anuar Mohamed, M. K., Abas, F. N. and Salleh, M. Z. (2019). MHD boundary layer flow over a permeable flat plate in a ferrofluid with thermal radiation effect. *Journal of Physics: Conference Series*, 1366(1), 012014.
- Arain, M.B., Bhatti, M.M., Zeeshan, A., Alzahrani, F.S. (2021). Bioconvection Reiner-Rivlin Nanofluid Flow between Rotating Circular Plates with Induced Magnetic Effects, Activation Energy and Squeezing Phenomena. *Mathematics*, 9 (17), 2139.
- Archana, M., Reddy, M. G., Giresha, B. J., Prasannakumara, B. C. and Shehzad, S. A. (2018). Triple diffusive flow of nanofluid with buoyancy forces and nonlinear thermal radiation over a horizontal plate. *Heat Transfer*, 47(8), 957–973.
- Awad, F. G., Motsa, S. and Khumalo, M. (2014). Heat and mass transfer in unsteady rotating fluid flow with binary chemical reaction and activation energy. *Plos One*, 9(9), e107622.
- Aydin, O. and Kaya, A O. (2009). MHD mixed convection of a viscous dissipating fluid about a permeable vertical flat plate. *Applied Mathematical Modelling*, 33 (11), 4086–4096.
- Aziz, A. (2009). A similarity solution for laminar thermal boundary layer over a flat plate with a convective surface boundary condition. *Communications in Nonlinear Science and Numerical Simulation*, 14(4), 1064–1068.
- Bachok, N., Ishak, A. and Pop, I. (2010). Boundary layer flow of nanofluids over a moving surface in a flowing fluid. *International Journal of Thermal Sciences*, 49, 1663–1668.
- Bachok, N., Ishak, A. and Pop, I. (2013). Mixed Convection Boundary Layer Flow over a Moving Vertical Flat Plate in an External Fluid Flow with Viscous Dissipation Effect. *PLOS ONE*, 8(4), e60766.
- Bataller, R. C. (2008). Radiation effects in the Blasius flow. *Applied Mathematics and Computation*, 198, 333–338.
- Bataller, R. C. (2008). Radiation effects for the Blasius and Sakiadis flows with a convective surface boundary condition. *Applied Mathematics and Computation*, 206 (2), 832–840.
- Bég, O. A., Hameed, M. and Bég, T. A. (2013). Chebyshev spectral collocation simulation of nonlinear boundary value problems in electrohydrodynamics. *International Journal of Computational Methods in Engineering Science and Mechanics*, 14, 104–115.

- Bég, O. A., Espinoza, D. S., Kadir, A., Shamshuddin, M. D. and Sohail, A. (2018). Experimental study of improved rheology and lubricity of drilling fluids enhanced with nano-particles. *Applied Nanoscience*, 8, 1069–1090.
- Bhatti, M.M., Abbas, T., Rashidi, M.M., Ali, M.E.-S. (2016). Numerical simulation of entropy generation with thermal radiation on MHD carreau nanofluid towards a shrinking sheet. *Entropy*, 18, 200.
- Bhatti, M. M., Ellahi, R., Zeeshan, A., Marin, M. and Ijaz, N. (2019). Numerical study of heat transfer and Hall current impact on peristaltic propulsion of particle-fluid suspension with compliant wall properties. *Modern Physics Letters B*, 33(35), 1950439.
- Bhatti, M. M., Shahid, A., Abbas, T., Alamri, S. Z. and Ellahi, R. (2020). Study of activation energy on the movement of gyrotactic microorganism in a magnetized nanofluids past a porous plate. *Processes*, 8(3), 328.
- Bognár, G. and Hriczó, K. (2020). Numerical Simulation of Water Based Ferrofluid Flows along Moving Surfaces. *Processes*, 8(7), 830.
- Bognár, G. and Hriczó, K. (2020). Ferrofluid flow in magnetic field above stretching sheet with suction and injection. *Mathematical Modelling and Analysis*, 25(3), 461–472.
- Boyd, J. P. (2001). *Chebyshev and Fourier spectral methods*. Courier Corporation.
- Brinkman, H.C. (1951). Heat Effects in Capillary Flow I. *Applied Scientific Research*, 2, 120–124.
- Brinkman, H. C. (1952). The viscosity of concentrated suspensions and solutions. *The Journal of chemical physics*, 20(4), 571–581.
- Cabuil, V. Dekker. (2004). Encyclopedia of Nanoscience and Nanotechnology; Chapter 119 Magnetic Nanoparticles: Preparation and Properties. *Roldan Group Publications; CRC Press: Boca Raton, FL, USA*.
- Canuto, C., Hussaini, M., Quarteroni, A. and Zang, T. (1988). Spectral Methods in Fluid Dynamics. *Springer-Verlag, Berlin*.
- Chamkha, A. J. (1997). Solar radiation assisted convection in uniform porous medium supported by a vertical plate. *ASME Journal of Heat Transfer*, 119, 89–96.

- Chazal, L. (1972). Analysis of heat and mass transfer, E. R. G. Eckert and R. M. Drake, Jr., McGraw-Hill, New York (1972). *Aiche Journal*, 18, 670–670.
- Chen, C. H. (1999). Forced convection over a continuous sheet with suction or injection moving in a flowing fluid, *ActaMechanica*, 138 (1-2), 1–11.
- Chiam, T. C. (1993). Magnetohydrodynamic boundary layer flow due to a continuously moving flat plate. *Computers & Mathematics with Applications*, 26(4), 1–7.
- Daniel, Y. S., Aziz, Z. A., Ismail, Z. and Salah, F. (2018). Thermal stratification effects on MHD radiative flow of nanofluid over nonlinear stretching sheet with variable thickness. *Journal of Computational Design and Engineering*, 5(2), 232–242.
- Darbari, B., Rashidi, S., AbolfazliEsfahani, J. (2016). Sensitivity analysis of entropy generation in nanofluid flow inside a channel by response surface methodology. *Entropy*, 18, 52.
- Das, K., Sharmab, R. P. and Sarkar, A. (2016). Heat and mass transfer of a second grade magnetohydrodynamic fluid over a convectively heated stretching sheet. *Journal of Computational Design and Engineering*, 3(4), 330–336.
- Davidson, P.A. (2006). An Introduction to Magnetohydrodynamics. *Cambridge University Press, Cambridge*.
- Desale, S. and Pradhan, V. H. (2015). Numerical Solution of Boundary Layer Flow Equation with Viscous Dissipation Effect Along a Flat Plate with Variable Temperature. *Procedia Engineering*, 127, 846–853.
- Don, W. S. and Solomonoff, A. (1995). Accuracy and Speed in Computing the Chebyshev Collocation Derivative. *SIAM Journal on Scientific Computing*, 16(6), 1253–1268.
- Elbashbeshy, E. M. A. and Bazid, M. A. A. (2000). The effect of temperature-dependent viscosity on heat transfer over a continuous moving surface. *Journal of Physics D: Applied Physics*, 33 (21), 2716.
- Ellahi, R., Alamri, S. Z., Basit, A. and Majeed, A. (2018). Effects of MHD and slip on heat transfer boundary layer flow over a moving plate based on specific entropy generation. *Journal of Taibah University for Science*, 12(4), 476–482.
- Fakhar, M.H., Fakhar, A., Tabatabaei, H. (2020). Mathematical modeling of pipes reinforced by agglomerated CNTs conveying turbulent nanofluid and application of semi-analytical method for studying the instable Nusselt number and fluid velocity. *Journal of Computational Applied Mathematics*, 378 (1), 112945.

- Farooq, M., Ahmad, S., Javed, M., Anjum, A. (2019). Melting heat transfer in squeezed nanofluid flow through Darcy Forchheimer medium. *Journal of Heat Transfer*, 141 (1), 012402.
- Ferdows, M., Khan, M. S., Alam, M. M. and Sun, S. (2012). MHD mixed convective boundary layer flow of a nanofluid through a porous medium due to an exponentially stretching sheet. *Mathematical Problems in Engineering*, 2012, 408528.
- Ferdows M, Shamshuddin M, Zaimi K. (2021). Computation of steady free convective boundary layer Viscous Fluid flow and heat transfer towards the moving flat subjected to suction/injection effects. *CFD Letters*, 13(3), 16–24.
- Ferdows, M., Alam, J., Murtaza, G., Tzirtzilakis, E.E., Sun, S. (2022). Biomagnetic Flow with CoFe_2O_4 Magnetic Particles through an Unsteady Stretching/Shrinking Cylinder. *Magnetochemistry*, 8, 27.
- Feynman, R. P., Leighton, R. B. and Sands, M. (1963). *The Feynman Lectures on Physics*. Reading, MA: Addison-Wesley.
- Frey, N.A., Peng, S., Cheng, K., Sun, S. (2009). Magnetic nanoparticles: Synthesis, functionalization, and applications in bioimaging and magnetic energy storage. *Chemical Society Review*, 38 (9), 2532–2542.
- Gireesha, B., Mahanthesh, B., Thammanna, G., Sampathkumar, P. (2018). Hall effects on dusty nanofluid two-phase transient flow past a stretching sheet using KVL model. *Journal of Molecular Liquids*, 256, 139–147.
- Golla, R.K. (2023). Nanofluid Boundary Layer Analysis in the Presence of Magnetic Lines of Force Being Fixed Relatively to the Plate and the Water-based Nanofluid Containing Copper, Aluminum Trioxide, and Silicon Dioxide Nanoparticles. *Biointerface Research in Applied Chemistry*, 13 (5), 406.
- Haddad, Z., Nada, A., Oztop, F. and Mataoui, A. (2012). Natural convection in nanofluids: Are the thermophoresis and Brownian motion effects significant in nanofluid heat transfer enhancement? *International Journal of Thermal Sciences*, 57, 152.
- Haile, E. Shankar, B. (2015). Boundary layer flow of nanofluids over a moving surface in the presence of thermal radiation, viscous dissipation and chemical reaction. *Applications and Applied Mathematics: An International Journal (AAM)*, 10 (2), 952–969.

- Hakeem, A. A., Ganesh, N. V. and Ganga, B. (2014). Effect of heat radiation in a Walter's liquid B fluid over a stretching sheet with non-uniform heat source/sink and elastic deformation. *Journal of King Saud University-Engineering Sciences*, 26(2), 168–175.
- Hamad, M. A., Pop, I. and Md. Ismail, A. I. (2011). Magnetic field effects on free convection flow of a nanofluid past a vertical semi-infinite flat plate. *Nonlinear Analysis: Real World Application*, 12, 1338–1346.
- Haroun, N. A., Sibanda, P., Mondal, S. and Motsa, S. S. (2015). On unsteady MHD mixed convection in a nanofluid due to a stretching/shrinking surface with suction/injection using the spectral relaxation method. *Boundary Value Problems*, 2015(1), 24.
- Blasius, H. (1907). *Grenzschichten in Flüssigkeiten mit kleiner Reibung*. Druck von BG Teubner.
- He, W., Tongraie, D., Lotfipour, A., Purfattah, F., Karimipour, A., Afrand, M. (2020). Effect of twisted tape inserts and nanofluid on flow field and heat transfer characteristics in a tube. *International Communications in Heat and Mass Transfer*, 110, 104440.
- Himanshu Upreti, Alok Kumar Pandey and Manoj Kumar (2020). Thermophoresis and suction/injection roles on free convective MHD flow of Ag–kerosene oil nanofluid. *Journal of Computational Design and Engineering*, 7, 3, 386–396.
- Hughes, W. F. and Young, F. J. (1966). *The electromagnetodynamics of fluids*. John Wiley.
- Ishak, A., Yacob, N. and Bachok, N. (2011). Radiation effects on the thermal boundary layer flow over a moving plate with convective boundary condition. *Meccanica*, 46 (4), 795–801.
- Jafar, K., Nazar, R., Ishak, A. and Pop, I. (2011). MHD flow and heat transfer over stretched/shrinking sheets with external magnetic field, viscous dissipation and Joule effects. *Canadian Journal of Chemical Engineering*, 99, 1–11.
- Jafar, A. B., Shafie, S. and Ullah, I. (2019). Magnetohydrodynamic Boundary Layer Flow of a Viscoelastic Fluid Past a Nonlinear Stretching Sheet in the Presence of Viscous Dissipation Effect. *Coatings*, 9(8), 490.
- Buongiorno, J. (2006). Convective transport in nanofluids. *ASME Journal of Heat and Mass Transfer* 128 (3), 240–250.

- Jumah, R. Y., Banat, F. A. and Abu-Al-Rub, F. (2001). Darcy-Forchheimer mixed convection heat and mass transfer in fluid saturated and porous media. *International Journal of Numerical Methods for Heat and Fluid Flow*, 11(6), 600–618.
- Khan, W. A., Khan, Z. H. and Haq, R. U. (2015). Flow and heat transfer of ferrofluids over a flat plate with uniform heat flux. *The European Physical Journal Plus*, 130(4), 86.
- Kumari, M. and Nath, G. (1996). Boundary layer development on a continuous moving surface with a parallel free stream due to impulsive motion. *Heat and Mass Transfer*, 31 (4), 283–289.
- Kumar, P. and Poonia, H. (2022). Slip Effect on Magnetohydrodynamic Boundary Layer Flow of Nanofluid over an Stretching Sheet with Thermal Radiation and Thermal Convective Boundary Condition. *Current Journal of Applied Science and Technology*, 41(46), 33–45.
- Long, N. M. A. N. Suali, M., Ishak, A., Bachok, N., Arifin, N. M. (2011). Unsteady stagnation point flow and heat transfer over stretching/shrinking sheet. *Journal of Applied Sciences*, 11 (20), 3520–3524.
- Mabood, F., Khan, W. A. and Ismail, A. I. M. (2015). MHD boundary layer flow and heat transfer of nanofluids over a nonlinear stretching sheet: A numerical study. *Journal of Magnetism and Magnetic Materials*, 374, 569–576.
- Maiti, H., Mukhopadhyay, S. (2023). Existence of MHD boundary layer hybrid nanofluid flow through a divergent channel with mass suction and injection. *Chemical Engineering Journal Advances*, 14, 100475.
- Mahanthesh, B., Gireesha, B., Shashikumar, N. Shehzad, S. (2017). Marangoni convective MHD flow of SWCNT and MWCNT nanoliquids due to a disk with solar radiation and irregular heat source. *Physica E: Low-dimensional Systems and Nanostructures*. 94, 25–30.
- Maruno, S., Yubakami, K. and Soga, M. (1983). Plain paper recording process using magnetic fluids magneto-fluid-graphy. *Journal of Magnetism and Magnetic Materials*, 39(1-2), 187–189.
- Martin, M.J. and Boyd, I. D. (2006). Momentum and Heat Transfer in a Laminar Boundary Layer with Slip Flow. *Journal of Thermophysics and Heat Transfer*, 20, 710–719.
- Maxwell, J. (1881). *A Treatise on Electricity and Magnetism*. 2nd edition, Clarendon Press, Oxford, UK.

- Maxwell-Garnett, J. C. (1904). XII. Colours in metal glasses and in metallic films. *Philosophical Transactions of the Royal Society of London. Series A, Containing Papers of a Mathematical or Physical Character*, 203(359-371), 385–420.
- Ming-I Char, Cha'O-Kuang Chen, John W. Cleaver. (1990). Conjugate forced convection heat transfer from a continuous, moving flat sheet. *International Journal of Heat and Fluid Flow*, 11 (3), 257–261.
- Mishra, S. R., Baag, S., Bhatti, M. M. (2018). Study of heat and mass transfer on MHD Walters B nanofluid flow induced by stretching plate surface. *Alexandria Engineering Journal*, 57 (4), 2435–2443.
- Mohammadein, A. A. and El-Amin, M. F. (2000). Thermal radiation effect on power law fluid over a Horizontal plate embedded in a porous medium. *International Communications in Heat and Mass Transfer*, 27, 1025–1035.
- Mohamed, M. K. A., Mat Yasin, S. H. and Salleh, M. Z. (2021). Slip Effects on MHD Boundary Layer Flow over a Flat Plate in Casson Ferrofluid. *Journal of Advanced Research in Fluid Mechanics and Thermal Sciences*, 88(1), 49–57.
- Mukhopadhyay, S. (2013). MHD boundary layer slip flow along a stretching cylinder. *Ain Shams Engineering Journal*, 4(2), 317–324.
- Motsa, S. S. (2014). A new spectral relaxation method for similarity variable nonlinear boundary layer flow systems. *Chemical Engineering Communications*, 201, 241–256.
- Motsa, S. S. and Makukula, Z. G. (2013). On spectral relaxation method approach for steady von Karman flow of a ReinerRivlin fluid with Joule heating, viscous dissipation and suction/injection. *Central European Journal of Physics*, 11(3), 363– 374.
- Mosayebidorcheh, S., Hatami, M. (2018). Analytical investigation of peristaltic nanofluid flow and heat transfer in an asymmetric wavy wall channel (Part II: Divergent channel). *International Journal of Heat Mass Transfer*, 126, 800–808.
- Mustafa, M., Khan, J. A., Hayat, T. and Alsaedi, A. (2015). Analytical and numerical solutions for axisymmetric flow of nanofluid due to non-linearly stretching sheet. *International Journal of Non-Linear Mechanics*, 71, 22–29.

- Nadeem, S., Rehman, M. I, Saleem, S. and Bonyah, E. (2020). Dual solutions in MHD stagnation point flow of nanofluid induced by porous stretching/shrinking sheet with anisotropic slip. *AIP Advances*, 10(6).
- Navier, C. L. M. H. (1827). Dissertation on the laws of fluid movements. *Memoirs of the Academy of Sciences*, 6, 389–440.
- Neuringer, J. L. and Rosensweig, R. E. (1964). Ferrohydrodynamics. *The Physics of Fluids*, 7(12), 1927–1937.
- Oosthuizen, P. H. and Naylor, D. (1999). An introduction to convective heat transfer analysis. *New York: WCB/McGraw Hill*.
- Oztop, H. F. and Abu-Nada, E. (2008). Numerical study of natural convection in partially heated rectangular enclosures filled with nanofluids. *International journal of heat and fluid flow*, 29(5), 1326–1336.
- Papell, S. S. (1965). Low viscosity magnetic fluid obtained by the colloidal suspension of magnetic particles. *US Patent 3,215,572*.
- Pankhurst, Q. A., Connolly, J., Jones, S. K. and Dobson, J. (2003). Applications of magnetic nanoparticles in biomedicine. *Journal of physics D: Applied physics*, 36(13), R167.
- Popplewell, J. (1984). Technological applications of ferrofluids. *Physics in technology*, 15(3), 150.
- Prasad, P. D., Kumar, R.V. M. S. S. K., Varma, S.V.K. (2016). Heat and mass transfer analysis for the MHD flow of a nanofluid with radiation absorption. *Ain Shams Engineering Journal*, 9(4), 801–813.
- Rafique, K., Mahmood, Z., Khan, U. (2023). Mathematical analysis of MHD hybrid nanofluid flow with variable viscosity and slip conditions over a stretching surface. *Materials Today Communications*, 36, 106692.
- Raj, K. and Moskowitz, R. (1990). Commercial applications of ferrofluids. *Journal of Magnetism and Magnetic Materials*, 85, 233–245.
- Ramli, N., Ahmad, S. and Pop, I. (2017). Slip effects on MHD flow and heat transfer of ferrofluids over a moving flat plate. *AIP Conference Proceedings*, 1870 (1), 040015.

- Ramesh, G. K., Chamkha, A. J. and Gireesha, B. J. (2016). Boundary layer flow past an inclined stationary/moving flat plate with convective boundary condition. *Afrika Matematika*, 27, 87–95.
- Rana, P., Bhargava, R., Bég, O. A. and Kadir, A. (2017). Finite element analysis of viscoelastic nanofluid flow with energy dissipation and internal heat source/sink effects. *International Journal of Applied and Computational Mathematics*, 3(2), 1421–1447.
- Raptis, A. (1998b). Radiation and free convection flow through a porous medium. *International Communications in Heat and Mass Transfer*, 25, 289–295.
- Rasheed, H., Rehman, A., Sheikh, N. and Iqbal, S. (2017). MHD boundary layer flow of nanofluid over a continuously moving stretching surface. *Applied and Computational Mathematics*, 6(6), 265–270.
- Rashidi, M. M., Kavyani, N., Shirley, A. (2014). Double diffusive magnetohydrodynamic (MHD) mixed convective slip flow along a radiating moving vertical flat plate with convective boundary condition. *PLoS ONE*, 9(10), e109404.
- Rasool, G., Shah, S. Z. H., Sajid, T., Jamshed, W., Cieza Altamirano, G., Keswani, B. and Sánchez-Chero, M. (2022). Spectral Relaxation methodology for chemical and bioconvection processes for cross nanofluid flowing around an oblique cylinder with a slanted magnetic field effect. *Coatings*, 12(10), 1560.
- Reddy, G. J., Raju, R. S. and Rao, J. A. (2017). Influence of viscous dissipation on unsteady MHD natural convective flow of Casson fluid over an oscillating vertical plate via FEM. *Ain Shams Engineering Journal*, 9(4), 1907–1915.
- Lotfi, R., Saboohi, Y. and Rashidi, A. M. (2010). Numerical study of forced convective heat transfer of nanofluids: comparison of different approaches. *International Communications in Heat and Mass Transfer*, 37(1), 74–78.
- Rosensweig, R.E. (1987). Magnetic fluids. *Annual Review of Fluid Mechanics*, 19, 437–463.
- Saleem, S., Qasim, M., Alderremy, A. and Noreen, S. (2020). Heat transfer enhancement using different shapes of Cu nanoparticles in the flow of water based nanofluid, *Physica Scripta*, 95(5), 055209.
- Sakiadis, B. C. (1961). Boundary layer behaviour on continuous solid surface, *AIChE. J.*, 7, 26–28.

- Scherer, C. and Figueiredo Neto, A. M. (2005). Ferrofluids: properties and applications. *Brazilian journal of physics*, 35, 718–727.
- Shateyi, S., Marewo, G. T. (2013). A new numerical approach for the laminar boundary layer flow and heat transfer along a stretching cylinder embedded in a porous medium with variable thermal conductivity. *Journal of Applied Mathematics*, 2013, 1–7.
- Selimefendigil, F., Öztop, H. F., Abu-Hamdeh, N. (2016). Natural convection and entropy generation in nanofluid filled entrapped trapezoidal cavities under the influence of magnetic field. *Entropy*, 18(2), 43.
- Sheikholeslami, M. and Ellahi, R. (2015). Electrohydrodynamic nanofluid hydrothermal treatment in an enclosure with sinusoidal upper wall. *Applied Sciences*, 5(3), 294–306.
- Shliomis, M. I. (2004). Comment on “ferrofluids as thermal ratchets”. *Physical Review Letters*, 92(18), 188901.
- Singamaneni, S., Bliznyuk, V. N., Binek, C., Tsymbal, E.Y. (2011). Magnetic nanoparticles: Recent advances in synthesis, self-assembly and applications. *Journal of Material Chemistry*, 21 (42), 16819–16845.
- S. Kakac, A. Pramuanjaroenkij. (2009). Review of convective heat transfer enhancement with nanofluids. *International journal of heat and mass transfer*, 52(13-14), 3187–3196.
- S. Maiga, C. Nguyen, N. Galanis, G. Roy. (2004). Heat transfer behaviors of nanofluids in a uniformly heated tube. *Superlattices and Microstructures*. 35(3-6), 543–557.
- Sowmya, G., Gireesha, B. J. and Prasannakumara, B. C. (2019). Scrutinization of different shaped nanoparticle of molybdenum disulfide suspended nanofluid flow over a radial porous fin. *International Journal of Numerical Methods for Heat and Fluid Flow*, 30(7), 3685–3699.
- Srinivasacharya, D., Mendu, U. and Venumadhav, K. (2015). MHD boundary layer flow of a nanofluid past a wedge. *Procedia Engineering*, 127, 1064–1070.
- Sus, C. (1995). Enhancing thermal conductivity of fluids with nanoparticles, developments and applications of non-Newtonian flows. *ASME, FED, MD, 1995*, 231, 99–105.
- Tangthieng, C., Finlayson, B. A., Maulbetsch, J. and Cader, T. (1999). Finite element simulations of heat transfer to a ferrofluid in the presence of a magnetic field are

- presented for flow between flat plates and in a box. *Journal of Magnetism and Magnetic Materials*, 201(1–3), 252–255.
- Tiwari, R. K. and Das, M. K. (2007). Heat transfer augmentation in a two-sided lid-driven differentially heated square cavity utilizing nanofluids. *International Journal of heat and Mass transfer*, 50(9-10), 2002–2018.
- Thumma, T., Mishra, S. R. and Bég, O. A. (2020). ADM solution for Cu/CuO–water viscoplastic nanofluid transient slip flow from a porous stretching sheet with entropy generation, convective wall temperature and radiative effects. *Journal of Applied and Computational Mechanics*, 1–15.
- Trefethen, L. N. (2000). *Spectral methods in MATLAB*. Society for industrial and applied mathematics.
- Tripathi, D., Bég, O. A. (2014). A study on peristaltic flow of nanofluids: Application in drug delivery systems. *International Journal of Heat and Mass Transfer*. 70, 61–70.
- Trisaksri, V. and Wongwises, S. (2007). Critical review of heat transfer characteristics of nanofluids. *Renewable and sustainable energy reviews*, 11(3), 512-523.
- Tsou, F. K., Sparrow, E. M. and Goldstein, R. J. (1967). Flow and heat transfer in the boundary layer on a continuous moving surface. *International Journal of Heat and Mass Transfer*, 10 (2), 219–235.
- Tzirtzilakis, E. E., Kafoussias, N. G. and Raptis, A. (2010). Numerical study of forced and free convective boundary layer flow of a magnetic fluid over a flat plate under the action of a localized magnetic field. *Zeitschrift für angewandte Mathematik und Physik*, 61, 929–947.
- Tzou, D.Y. Thermal instability of nanofluids in natural convection. *Int. J. Heat Mass Transf.* 51, 2967–2979, (2008).
- Upreti, H., Pandey, A. K. and Kumar, M. (2020). Thermophoresis and suction/injection roles on free convective MHD flow of Ag–kerosene oil nanofluid. *Journal of Computational Design and Engineering*, 7(3), 386–396.
- Wang, R., DU, J. and Zhu, Z. (2016). Effects of wall slip and nanoparticles' thermophoresis on the convective heat transfer enhancement of nanofluid in a microchannel. *Journal of Thermal Science and Technology*, 11(1), JTST00017–JTST00017.

- Wang, X. Q. and Mujumdar, A. S. (2007). Heat transfer characteristics of nanofluids: a review. *International journal of thermal sciences*, 46(1), 1–19.
- Weideman, J. A. and Reddy, S. C. (2000). A MATLAB differentiation matrix suite. *ACM transactions on mathematical software (TOMS)*, 26(4), 465–519.
- Weidman, Patrick and Kubitschek, Daniel & Davis, A.M.J. (2006). The Effect of Transpiration on Self-Similar Boundary Layer Flow Over Moving Surface. *International Journal of Engineering Science*, 44, 730–737.
- Yohannes, Y. and Shankar, B. (2014). Melting heat transfer in MHD flow of nanofluids over a permeable exponentially stretching sheet. *Journal of Nanofluids*, 3, 90–100.
- Zhu, J., Chu, P., Sui, J. (2018). Exact analytical nanofluid flow and heat transfer involving asymmetric wall heat fluxes with nonlinear velocity slip. *Mathematical Problems in Engineering*, 2018, 3094980.